

**FABRICATION OF SOLID, POROUS, AND MAGNETIC CERAMIC
MICROPARTICLES VIA STOP-FLOW LITHOGRAPHY**

by

Alejandro M. Alcaraz Ramirez

A Dissertation

Submitted to the Faculty of Purdue University

In Partial Fulfillment of the Requirements for the degree of

Doctor of Philosophy



School of Materials Engineering

West Lafayette, Indiana

May 2020

THE PURDUE UNIVERSITY GRADUATE SCHOOL
STATEMENT OF COMMITTEE APPROVAL

Dr. Carlos J. Martinez

School of Materials Engineering

Dr. Rodney W. Trice

School of Materials Engineering

Dr. Ernesto E. Marinero

School of Materials Engineering

Dr. Kevin P. Trumble

School of Materials Engineering

Approved by:

Dr. David F. Bahr

Dedicated to my family and friends

ACKNOWLEDGMENTS

I want to express my initial gratitude to all Purdue community. I also want to thank Conacyt, for funding part of this research work. Starting with my advisor, Prof. Carlos Martinez, I want to thank his continuous guidance through all this process, as well as his patience to share all his experience and knowledge. I want to thank all my committee members for their support. Prof. Marinero, for creating the collaborative program with I2T2 from Monterrey, that let us start this journey. Prof. Trumble, for sharing his knowledge and dedicating time to explain scientific concepts. Prof. Trice, for encouraging me to become a part of the global scientific community. Additionally, I want to give special thanks to Prof. Erk and Prof. Howarter, for their support, and for letting me collaborate with their research groups. To Prof. Davis, for sharing her instruments and dedicating time to share her knowledge. I also want to thank Prof. Bahr, Prof. Handwerker, Prof. Kvam, Rosemary, Stacey, Aury, Lisa and Donna, for all their support. I want to thank the Hispanic association, SHPE, and the ceramic association, ACERS, for providing traveling funds to share my research work with the scientific community.

I want to express my infinite love and gratitude to my family, Lucia and Isabel, who have been unconditionally in this trip with me. I want to thank specially my mom Graciela, for her immeasurable love. My father Raul, my brother Raul Jr., and my sister Nayeli, for their unceasing support. I also want to thank all my friends, from Mexico and from West Lafayette, that I also consider part of my family. For my friends that have departed early from this world, I want to let them know that they will always be a part of me.

TABLE OF CONTENTS

LIST OF TABLES	8
LIST OF FIGURES	9
ABSTRACT	14
1. INTRODUCTION	16
1.1 Microparticles	16
1.1.1 The Importance of Microparticles	16
1.1.2 Fields of Application	16
1.1.3 Properties of Interest	18
1.2 Techniques for Fabricating Microparticles	19
1.2.1 General Techniques	19
1.2.2 Relevant Techniques	20
1.3 Selected Technique for the Fabrication of Microparticles	21
1.3.1 Flow Lithography	21
1.3.2 Material Requirements	21
1.3.3 Stop-Flow Lithography	22
1.4 Preceramic Polymer Precursors	24
2. STOP-FLOW LITHOGRAPHY AND PARTICLE DIMENSIONS VARIABILITY	27
2.1 Introduction	27
2.2 Stop-Flow Lithography	27
2.2.1 Set-up and Description	27
2.2.2 Material Selection	33
2.3 Particle Dimensions Variability	33
2.3.1 Introduction	33
2.3.2 Microchannel Mold	34
2.3.3 UV Source Variability	36
2.3.4 Oxygen Depletion Model	39
2.3.5 Conclusions	42
3. FABRICATION OF CERAMIC MICROPARTICLES FROM PRECERAMIC POLYMERS VIA STOP-FLOW LITHOGRAPHY	43

3.1	Introduction	43
3.2	Experimental Section	44
3.2.1	Materials, Characterization, and Methods	44
3.2.2	SFL Setup and Operation.....	44
3.2.3	Preceramic Particle Pyrolysis and Characterization	45
3.3	Results and Discussions	46
3.3.1	Cycle Times	46
3.4	Conclusions	51
4.	FABRICATION OF POROUS HEXAGONAL SIOC MICROPARTICLES VIA STOP- FLOW LITHOGRAPHY	53
4.1	Introduction	53
4.2	Experimental Section	54
4.2.1	Materials, Characterization, and Methods	54
4.2.2	Emulsion Generation	56
4.2.3	Hexagon Microparticle Fabrication	61
4.3	Conclusions	67
5.	FABRICATION OF SIOC MICROPARTICLES WITH EMBEDDED COBALT ZINC FERRITE NANOPARTICLES VIA STOP-FLOW LITHOGRAPHY	69
5.1	Introduction	69
5.2	Experimental Section	70
5.2.1	Materials, Characterization, and Methods	70
5.3	Results and Discussion.....	72
5.3.1	Preparation	74
5.3.2	Oval Shape Microparticle Fabrication	75
5.3.3	Drug Targeting.....	81
5.4	Conclusions	85
6.	FABRICATION OF BIFUNCTIONAL POLYMER PRECERAMIC MICROPARTICLES VIA CONTINUOUS-FLOW LITHOGRAPHY	86
6.1	Introduction	86
6.2	Experimental Setup	87
6.2.1	Materials, Characterization, and Methods	87

6.2.2	Method	88
6.3	Results and Discussion.....	89
6.3.1	Liquid-Liquid Interface.....	89
6.3.2	CFL Parameters	89
6.3.3	Functional Particles.....	90
6.4	Conclusions	92
7.	FUTURE WORK.....	93
7.1	Fabrication of Microbatteries	93
7.2	Self-Assembly Particles	95
7.3	Conclusions	97
8.	CONCLUSIONS	99
	APPENDIX A. ARDUINO PROGRAM.....	101
	REFERENCES	106
	VITA.....	120

LIST OF TABLES

Table 2.1: Polymerization rate parameters for PEGDA. ⁷⁵	41
Table 3.1: Relevant length and thickness for SFL fabricated particles before and after pyrolysis. Particles were fabricated in a channel 1 mm wide, 3 mm long and $75 \pm 4 \mu\text{m}$ height channel using a 20x and 10x objectives.	49
Table 4.1: Stop-Flow lithography fabrication parameters as objective used, number of exposed shapes, exposed particle size, flush out and cycle times.....	62
Table 4.2: Hexagon microparticles, droplets and pores relevant dimensions after fabrication, immersed in cleaning solution, and after pyrolysis.	63
Table 4.3: Glycerol and DI-H ₂ O contents of emulsion discontinuous phase to index match with preceramic continuous phase TEGO RC ® 711 refractive index.	66
Table 5.1: Sedimentation and centrifugation time to separate particle agglomerates of 0.4 – 10 μm in TEGO RC® 711 preceramic polymer matrix.	74
Table 5.2: Stop-flow lithography parameters used for the fabrication of oval microparticles containing Co _{0.5} Zn _{0.5} Fe ₂ O ₄ nanoparticles.	76
Table 5.3: Content of magnetic nanoparticles in the oval microparticles before and after pyrolysis.	77
Table 5.4: Particle dimensions of oval microparticles after fabrication, in cleaning solution and after pyrolysis.....	77
Table 5.5: Shows the elemental wt% calculated by EDX analysis for Oval SiOC particles containing CoZnFe ₄ O ₈	79
Table 5.6 (a) Available ferrites from the selected supplier (Nanostructured and Amorphous Materials Inc., Katy, TX) with information about the saturation magnetization, the remanent magnetization, and the susceptibility. (b) Used parameters to calculate magnetic field strength needed to move a microparticle with magnetic loading.	84
Table 6.1: Parameters used for the fabrication of dumbbell, ovals, and funnel-like preceramic polymer particles via CFL.	90
Table 6.2: Additional parameters used for the fabrication of predefined shape bimodal preceramic polymer microparticles.	90
Table 6.3: Parameters and major dimensions for the 3 different microparticles fabricated via CFL, for 2 inlet fluids, an emulsion and a suspension.	92

LIST OF FIGURES

Figure 1.1: Image showing swimming microrobot between magnetic fields, fabricated with MEMS technologies: a) oval microrobot, b) flagella microrobot. Reproduced from ref 10 with permission from SAGE Publications, copyright 2009.	17
Figure 1.2: SEM images of mask defined shapes fabricated via flow lithography techniques; (a) and (b) were fabricated with continuous-flow lithography and (c) with maskless-flow lithography. Scale bar in image (a) and (b) is 10 μm , and in (c) is 50 μm . Reproduced from refs 44, 50 with the corresponding permissions. Copyright 2006 Nature Publishing Group, 2009 The Royal Society of Chemistry.	21
Figure 1.3: Microscope images showing the steps of the SFL fabrication cycle inside the PDMS microchannel device. (a) The first step is the time it takes for the fluid to stop after the input pressure has been released, (b) the second step shows the selective polymerization of the polymer by UV projection through a photomask, and (c) the third step shows the particles being flushed out of the generation area after polymerization. Scale bar is 50 μm in all cases. Reproduced from ref 45 with permission from The Royal Society of Chemistry, copyright 2007.	23
Figure 1.4: (a) SEM micrograph of SiO_2 microgear sintered at 1150 $^{\circ}\text{C}$ fabricated via SFL by Shepherd et al., (b) SEM micrograph of sintered Al_2O_3 cube microparticles sintered at 1450 $^{\circ}\text{C}$ fabricated via SFL by Baah et al. Scale bar in (a) is 50 μm , while in (b) is 100 μm . Reproduced from refs 60, 61 with the corresponding permissions. Copyright 2008 WILEY-VCH Verlag GmbH & Co KGaA Weinheim, 2013 Elsevier B.V.	24
Figure 1.5: Schematic showing the most common preceramic polymer precursors with silicon as the main element in the polymer chain backbone. Reproduced from ref 71 with permission from The American Ceramic Society, copyright 2010.	25
Figure 1.6 Common monomer structure of preceramic polymers with silicon in their backbone, with side groups R^1 and R^2 that enhance crosslinking but may be lost during pyrolysis. R is oxygen, carbon or nitrogen. X and n are repeating units of the monomer and oligomer respectively.	25
Figure 2.1: Schematic showing the main stop-flow lithography components. A microcontroller coordinates the shutter and the air pump pulses. A UV light source is connected to a shutter that determines UV pulses. The fluid reservoir chamber moves the selected photosensitive fluid into the PDMS microchannel with air pulses controlled with a relay and a solenoid.	27
Figure 2.2: Drawings of designed patterns to be printed on a photomask with different shapes and arrays for the fabrication of microparticles via SFL.	29
Figure 2.3: Schematic of electrical connections to the solenoid, fluid reservoir, as well as fluid connections to the PDMS microchannel for SFL setup.	30
Figure 2.4: Flow diagram of Arduino SFL program instructions to define cycle times with the software or potentiometer and run SFL cycles in continuous loops.	30
Figure 2.5: Schematic of Arduino microcontroller connections to the relay, potentiometers, switch button, and 16x2 8-digit display with I2C interpreter.	31

Figure 2.6: Photograph of stop-flow lithography box with microcontroller, potentiometers, switch button, display, and banana jacks.	31
Figure 2.7: Photograph of the microchannel mold made with a self-adhesive vinyl film, an oval acrylic chamber and a 30-gauge needle tip. The scale bar (1mm) is valid along the horizontal centerline of the microchannel mold.....	32
Figure 2.8: Vinyl film thickness (a) with and (b) without adhesive, tested for different pressure passes with a granite base gauge meter.....	34
Figure 2.9: (a) Vinyl films thickness profile of two films, one with and one without adhesive, and (b) shows pictures of vinyl films with arrow profile needle tip scanning line.	35
Figure 2.10: (a) Top view image of vinyl film cut with a razor blade adhered to a silicon wafer; (b) and (c) show vinyl height comparison by colors; (d), (e), and (f) plots correspond to the arrows in (a), delineating the scanning direction. Measurement lines were performed with a confocal microscope for a section of a vinyl film with adhesive. The height of the vinyl film is 70 μm except the right size where the film was cut with a razor blade, showing adhesive agglomeration.	36
Figure 2.11: Showing degradation time vs. bulb elapsed time (hours), for UV light source X-Cite 120, reconstructed plot from supplier's technical sheet. ⁸¹	37
Figure 2.12: (a) Optical image showing microscope observation area, and the reduced projected area in the blue circle. (b) Normalized intensity variation through the diagonal length (orange arrow).	38
Figure 2.13: Optical images showing fabrication of hexagonal shape particles after UV patterned exposure through 3 different masks with increasing number of shapes. Values within the image represent the mean diagonal dimensions of the hexagons for a given mask.	38
Figure 2.14: Relative average UV intensity vs. time, plotted for 200 ms, showing peak variation for a square wave with a frequency of 150 Hz.	39
Figure 2.15: Thickness variation of (a) PEGDA and (b) TEGO RC ® 711 as number of fabrication cycles increased.	40
Figure 2.16: Oxygen concentration as a function of time for PEGDA with addition of three different photoinitiator concentrations, 2.5 wt%, 5 wt% and 10 wt%.	42
Figure 3.1: Schematic of SFL system showing the PDMS channel device with the photosensitive solution being flowed after UV light has been exposed through the microscope objective. Crosslinked particles and excess uncrosslinked solution are recovered in a filtering mesh after generation.	46
Figure 3.2: (a) Theoretical response subtime (t_{res} in red) and total experimental stop time (t_{stop} in blue) for microchannel length of 3, 4, 5, and 6 mm. The 3 arrows show the subtimes ($t_{\text{res}} + t_{\text{dec}} + t_{\text{rtf}}$) of stop time. (b) Decompression time vs. initial chamber pressure for the fluid reservoir. The black arrow shows the decompression time (t_{dec}) for an input chamber pressure of 1.2 E5 Pa....	47
Figure 3.3: Optical (a) and SEM (b) images of hexagons, triangles, and gears particles synthesized via SFL. The upper row shows crosslinked polysiloxane particles in solution after cleaning while the lower row shows the particles after pyrolysis converted to SiOC.	49

Figure 3.4: (a) Transmittance as a function of wavelength for the preceramic capsules cross-linked in solution and the oxycarbide glass (SiOC) samples after pyrolysis at 1000 °C in nitrogen. (b) X-ray diffraction profile as a function of scanning angle for the oxycarbide glass particles (SiOC) after pyrolysis at 1000 °C in nitrogen. 51

Figure 4.1: Image of photomask used to expose patterned UV light for the photopolymerization of the preceramic polymer emulsion. 55

Figure 4.2: Droplet content vs. droplet size for laminar emulsification, considering constant volume and rotational speed for a 5-minute and 20-minute run. The error bar represents the standard deviation measured with a confidence interval of 95%. 58

Figure 4.3: Droplet size for laminar and turbulent homogenization, showing the two-step emulsification process. 70–100 droplet sizes were measured, with a bin size of 0.5 μm 60

Figure 4.4: Droplet size vs. (a) dispersed phase, and (b) power for laminar and turbulent emulsification processes. Total volume was maintained constant with a droplet content of 10 wt%. For the case of laminar homogenization, x-axis is rotational speed. For turbulent homogenization, x-axis is power amplitude. The error bar represents the standard deviation measured with a confidence interval of 95%. 60

Figure 4.5: Rheology behavior of DI-H₂O/TEGO RC® 711 emulsion with DI-H₂O content of 5, 10 and 15 wt%. 61

Figure 4.6: Schematic showing (a) PDMS microchannel device with emulsion entrance, fabrication area and collection chamber region; patterned UV light is projected to the fabrication area where the emulsion polymerizes in SFL cycles. (b) Schematic showing side view of microchannel particle fabrication area, showing the emulsion and partial height polymerization of the microparticles. The schematics are used for description, they are not actual scales. 62

Figure 4.7: (a) Optical images of polymerized acrylated polysiloxane/DI-H₂O emulsion hexagon microparticles in cleaning solution. (b) SEM images of the ceramic hexagon microparticles after completion of polymer to ceramic transformation. 63

Figure 4.8: (a) Image showing one side of a ceramic microparticle with a higher content of porosity, after converting the image to black and white with the threshold method, the area with pores was measured at 11%. (b) Side two showed a low content of porosity, after doing the conversion of the image to black and white with the threshold method, the porous are was measured at 1%. 64

Figure 4.9: Schematic showing a PDMS microchannel where an emulsion is flow. Droplets experience migration due to a lift force (F_L) towards the centerline of the microchannel. t_1 , t_2 and t_3 , represent increasing times when the particle will change position. 65

Figure 4.10: Microparticles thickness as a function of droplet concentration for the case of DI-H₂O and 71 wt% glycerol/29 wt% DI-H₂O as the dispersed phase in the preceramic polymer TEGO RC® 711. The error bar represents the standard deviation measured with a confidence interval of 95%. 67

Figure 5.1: TEM image of magnetic nanoparticles Co_{0.5}Zn_{0.5}Fe₂O₄ provided by Nanostructured and Amorphous materials, Inc. 71

Figure 5.2: Illustration of ultrasonic tip immersed in vial (a) close to the bottom and (b) close to the top of the solution, containing preceramic polymer and magnetic nanoparticles.....	72
Figure 5.3: Size distribution plot for agglomerated $\text{Co}_{0.5}\text{Zn}_{0.5}\text{Fe}_2\text{O}_4$ nanoparticles immersed in $\text{DI-H}_2\text{O}$ after ultrasonic mixing in a 1-dram vial with 20% of power amplitude.....	73
Figure 5.4: (a) Suspension transmittance vs. UV-light wavelength for TEGO RC® 711 containing $\text{CoZnFe}_4\text{O}_8$. b) Picture of suspensions after ultrasonic mixing for vials containing TEGO RC® 711 and magnetic particles with concentrations of 0.005 wt%, 0.015 wt%, 0.05 wt%, and 0.1 wt%. 75	75
Figure 5.5: Photograph of a photomask used for the fabrication of oval microparticles with a 3x3 array via SFL.....	76
Figure 5.6: Photographs of oval shape polymer microparticles with embedded $\text{CoZnFe}_4\text{O}_8$ magnetic nanoparticles in cleaning solution, from (a) vial 1 and (b) vial 2; (b) SEM images of ceramic SiOC microparticles with embedded $\text{CoZnFe}_4\text{O}_8$ magnetic nanoparticles after pyrolysis transformation.	78
Figure 5.7: EDX analysis of oval ceramic microparticles with embedded $\text{CoZnFe}_4\text{O}_8$ magnetic nanoparticles. Particles from vial 2, side 1.	80
Figure 5.8: XRD data comparing scans for $\text{CoZnFe}_4\text{O}_8$ crystal structure before and after pyrolysis. The peaks are the spinel ferrite lattice planes.	80
Figure 5.9: Magnetic force field with colors, showing the effect of 4 solenoids, with 10 cm of vertical distance and 5 cm of horizontal distance. The colors are shown in exponential form corresponding to 10^n , from 0 to -25.	82
Figure 5.10: Schematic of arm with sleeve that contains 4 solenoids with an hypothetical strength of 1 Tesla to control magnetic particles directionality with magnetic field. Red arrows show initial and final desired points for a magnetic microparticle that acts as a drug carrier. Image of arms with arteries modified from original source from basicmedicalkey site.....	83
Figure 5.11: The magnetic field strength of two solenoids separated at a distance of 10 cm as shown in figure 5.10, for magnetic oval particles with the dimensions used in this chapter with loading (wt%) increasing from 1 to 10wt%.....	84
Figure 6.1: Drawings of potential particles having two sections, usually known as Janus particles. These types of particles can be fabricated with a 2-entrance microchannel PDMS device to be used in SFL.....	86
Figure 6.2: Photograph of microchannel mold showing the 3 different regions to imprint a PDMS microchannel device for the fabrication of bifunctional preceramic particles via CFL. It also shows the elements used for its construction. The scale bar is valid along the centerline of the image. 87	87
Figure 6.3: Schematic showing the microcontroller, the fluid reservoirs, the UV source, the shutter, and the PDMS microchannel device. The solutions were flown inside the PDMS microchannel with independent input pressures from the fluid reservoirs. UV pulses were controlled with the microcontroller and shutter and were exposed to the PDMS microchannel to polymerized bifunctional microparticles.	88

Figure 6.4: Image of the solutions entrance of a two-inlet PDMS microchannel device with two solutions, a suspension and an emulsion, prepared as described in chapter 4 and 5.	91
Figure 6.5: Optical images of microparticles with two sides, one porous and one magnetic, fabricated via CFL. The mask used to fabricate the shapes is shown in the inset of the upper row images.	91
Figure 7.1: Schematic of microbatteries with three components: anode, separator and cathode. (a) Design considering porous spheres in the cathode and anode sections; (b) drawing of square shape with the three sections resembling a battery architecture.	93
Figure 7.2: Photograph of microchannel mold with three entrances, indicating the microchannel regions for a three-entrance microchannel for the fabrication of microparticles with three different sections.	94
Figure 7.3: Photographs showing suspensions containing functional powders for anode, separator, and cathode for the fabrication of microbatteries via SFL.	94
Figure 7.4: PDMS microchannel device with 3 entrances having components of a microbattery, the anode, the separator, and the cathode. The 3 suspensions have different loadings. The middle fluid contained PEGDA 400 as the photopolymer matrix, while the outer regions contained TEGO RC® 711 as the photopolymer matrix.	95
Figure 7.5: (a) Micron size polyhedral folded from planar substrates, (b) 3D aggregate of micron size plates assembled by capillary forces, and (c) millimeter polymeric plates assembled at water/perfluorodecalin interface by capillary interactions. Reproduced from ref 154 with permission from The American Association for the Advancement of Science, copyright 2002.	96
Figure 7.6: Hexagon polysiloxane polymer TEGO RC ® 711 microparticles fabricated via SFL and collected in DI-H ₂ O. The hexagons agglomerated due to their hydrophobic characteristic.	96
Figure 7.7: Drawings showing potential shapes that can be fabricated assuming two different properties: potentially one that is hydrophilic and one that is hydrophobic for self-assembly structures.	97

ABSTRACT

Microparticles have been investigated not only as feedstock spherical or amorphous bulk materials used for shape molding, but also as agents that can perform work in the micron scale. The fabrication of microparticles with active properties of self-propulsion, self-assembly, and mobility with enhanced mechanical, thermal, and chemical properties is of particular interest for emerging technologies such as drug delivery, micro-robotics, micro energy generation/harvesting, and MEMS. Conventional fabrication methods can produce several complex particle shapes in one fabrication session or hundreds of spheroid shaped particles per second. Innovative techniques, as flow lithography, have demonstrated control over particle form and composition for continuous fabrication cycles. In recent years predefined shape polymer microparticles have been fabricated as well as ceramic microparticles through suspension processing with these set of techniques. Even though ceramic materials have been fabricated, there is still a strong need to increment the palette of available materials to be processed via flow lithography. We have pioneered the production of shaped ceramic microparticles by Stop-Flow Lithography (SFL) using preceramic polymers, providing control of particle size and shape in the range of 1 – 1000 μm . The principal arranged technique (SFL) combines aspects of PDMS-based microfluidics and photolithography for the continuous cyclable fabrication of microparticles with predefined shapes. The PDMS microchannel devices used were fabricated with vinyl film molds in a laminar hood avoiding the need for a cleanroom, procedure that reduced fabrication costs. After a fabrication session, the preceramic polymer microparticles were collected, washed, and dried before entering an inert atmosphere furnace for pyrolysis. Additionally, by treating the material initially as liquid polymer, special properties can be added by converting it into an emulsion or a suspension. Microparticles were functionalized by introducing porosity and magnetic nanoparticles in the preceramic polymer matrix. The porous characteristic of a particle leads to an increase in surface area, allowing the particle to be infiltrated with a catalyzer or act as a chemical/physical carrier, and the magnetic behavior of the particles allows a controllable trajectory with defined external magnetic fields. These two properties can be used to fabricate bifunctional microparticles to serve as drug carriers through human arteries and veins for drug delivery purposes. We successfully fabricated solid and functional ceramic microparticles in the 10 – 50 μm range with predefined shapes as hexagons,

gears, triangles, and ovals. This system is an economical route to fabricate functional defined shape particles that can serve as microrobots to perform tasks in liquid media.

1. INTRODUCTION

1.1 Microparticles

1.1.1 The Importance of Microparticles

Microparticles are now also viewed as agents that can perform work on the micron scale. As their functionalities increase, so do their applications. For this reason, the fabrication of monodisperse, well-defined, non-spherical microparticles with enhanced mechanical properties, and dynamic characteristics is of interest for areas such as of microrobotics, micro-energy generation/harvesting, drug delivery, and micro electro-mechanical systems. Microparticles with functional properties may perform work, for instance, in the field of drug delivery.¹ Two dynamic characteristics of microparticles that are a focus of current research are self-propulsion and controlled mobility. These characteristics have the potential to enhance microparticles for use as active agents that can perform work on the micron scale. Both functionalities are achieved mainly through chemical reactions and magnetic or electric forces, but may also be achieved through alternative mechanisms such as UV exposure, ultrasound vibration, and capillary action.²

Historically, devices in the micron range have been created with conventional fabrication methods used for semiconductors: photolithography, thin film deposition, etching, and lift-off. Micro electro-mechanical systems (MEMS) are the best examples of dynamic micro elements able to perform work in the micron range. MEMS have applications in many fields,³ including electronics, optics, medicine, biotechnology, sensors, communication, and avionics. These abilities suggest complex tasks for a microrobot to perform. However, these fabrication techniques are constrained by material availability, confined geometries, the need for a cleanroom environment, and high investment costs. By simplifying shapes and functions, a microrobot in liquid media can be treated as a functional or active microparticle.

1.1.2 Fields of Application

Microrobotics and Drug Delivery

Microrobots are robots on a millimeter, or micron-size scale. Efforts to build and automate microrobots have been constant in recent decades. Microcomponents such as micro/nanomotors⁴ and micron-size electromagnetic actuators to give power to microants⁵ or miniature robots⁶ that

can move,⁷ jump,⁸ or fly,⁹ have progressed tremendously in recent decades. However, in liquid media motors and actuators movements are not efficient at the micron scale due to scalability, power, and inertia effects. At the micron scale in liquid media, viscosity effects reign over inertia and weight. Reciprocal body motion, as in macroscale swimmers, has a negligible movement effect.¹⁰ At Reynolds number < 1 , the main property affecting a micron-size particle is viscosity. In this condition, called creeping flow or Stokes flow¹¹, there is no turbulent transition and flow patterns do not change considerably.

Microrobot geometries, thus, need to be founded on different movements than traditional robots. Microrobots in liquid media should mimic microorganisms and soft-body fish shapes. One way for microrobots to swim in viscous media is to imitate the movements of microorganisms. For example, microorganisms such as cilia or eukaryotic flagella change their configuration to reduce friction during active movement strokes. Prokaryotic flagella use a molecular motor to rotate their tails and move with a corkscrew-like movement. Propulsion schemes with magnetic field gradients¹² and helical propellers that mimic bacterial flagella¹³ have been shown to be the most efficient options (figure 1.1). In the future, microrobots should be able to sense, actuate, and locomote by themselves. However, locomotion is the first step towards robotic miniaturization in liquid media.

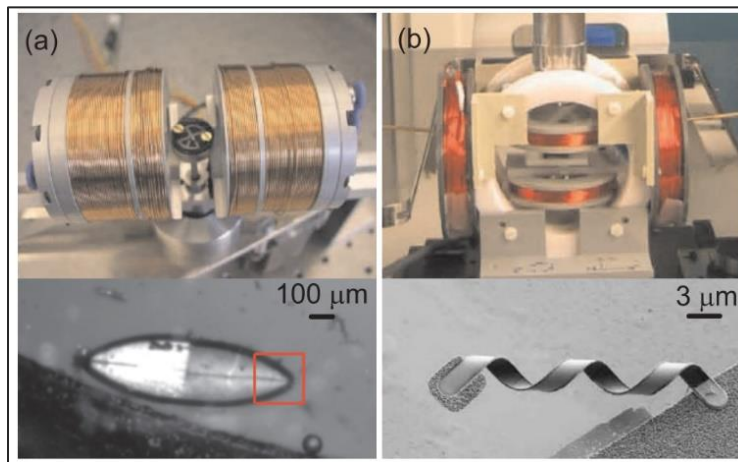


Figure 1.1: Image showing swimming microrobot between magnetic fields, fabricated with MEMS technologies: a) oval microrobot, b) flagella microrobot. Reproduced from ref 10 with permission from SAGE Publications, copyright 2009.

Drug delivery systems are a field of constant growth, expanding at a rate¹ of 15% in 2017. Controlled drug delivery aims to reduce side effects by delivering drugs on-site without affecting tissues or organs. Current technologies such as capsule endoscopy and lab-on-a-chip are medical solutions that reduce the need for invasive medical treatments¹⁴. Microrobotics are a promising path for medical interventions since they can navigate in liquid media to perform diagnosis and therapy. Microfabrication techniques for MEMS and NEMS are being utilized to fabricate miniature robots that can be deployed in human bodies to accomplish specific complex tasks. With robots or particle sizes in the micron range, wireless intervention is possible in the circulatory, urinary, and nervous systems. Devices capable of developing in the range between 3 μm to 800 μm can be safely injected into the human body.¹⁵

In recent years, research for chemotherapies using magnetic particles as drug carriers has been pursued; for example, a cytotoxic drug was attached to a magnetic particle that was injected through a patient's circulatory system and targeted on tumor cells using magnetic fields.¹⁶ Magnetic particles acting as drug carriers may be directed along specific artery and vein paths by controlling nearby magnetic field strength and direction, offering a non-intrusive alternative to medical surgery interventions. By developing an economical fabrication method that can functionalize particles with precise and defined shapes, simple microrobots can be fabricated.

1.1.3 Properties of Interest

In this work we are interested in two properties, for a particle to locomote and perform work as a drug carrier: porosity and magnetism. We also recognize that this requires particles to develop a self-propulsion capability that can be acquired by adding energy harvesting and/or energy storage functionalities.

Porosity

Porous structures may serve as cell-culture environments¹⁷ or drug delivery carriers.¹⁸ Particles resembling microorganisms or flagella can use the tail as a reservoir or drug carrier.¹ Porous particles with a head and a tail are viable for drug targeting.¹⁴ More specifically, an important feature of porosity is its capacity to increase the surface area of a material, which promotes its ability for infiltration and surface modification for self-propelled particles.¹⁹ Porosity

may also impact density and permeability; and may also have a negative effect on the mechanical properties of a material.

Magnetism

Magnetism has a wide range of applications. One use of magnetism in microparticles is to control their mobility, a property of interest for the fields of structured assembly,²⁰ microrobotics²¹ and drug targeting.¹⁶ Magnetic microparticles can serve as non-intrusive medical devices, providing an alternative to surgeries.²² Research on chemotherapies has deployed magnetic drug carriers,²³ in which a cytotoxic drug attached to a magnetic particle travels through the patient's circulatory system towards areas of concentrated tumor cells.

Energy Harvesting and Energy Storage

Energy harvesting and energy storage are characteristics of interest as they could provide independent locomotion to microparticles. In the case of energy harvesting, piezoelectric materials are a common method for harvesting energy from the environment, as they can convert external pressure to electricity. Many commonly used piezoceramics are derived from lead-zirconate-titanate (PZT), such as PZT-5H and PZT-8.²⁴ In the case of piezopolymers, the most frequently used material is polyvinylidene fluoride (PVDF).²⁵

Fabrication of micro electrochemical energy storage devices and micro electrochemical capacitors will promote independence and the ability to reduce the size of microactuators, MEMS, and sensors. Fabrication of these devices via additive manufacturing technologies has been proved to be feasible. For example, Tian et al. fabricated a 3D printed microbattery with inks containing suspended nanoparticles deposited layer-by-layer to construct the anode and cathode.²⁶ Additionally, Sun et al.²⁷ fabricated a 30 μm layer width microbattery with inks containing Li_4TiO and LiFePO_4 nanoparticles.

1.2 Techniques for Fabricating Microparticles

1.2.1 General Techniques

In recent decades, diverse techniques have been developed to fabricate droplets, particles, devices, and systems with several properties in the micro- and nano-size range. In this section, we

will give a general overview of relevant techniques and focus on those that match the focus of this work. Polymer microparticles are typically fabricated through droplet generation, emulsion processing, and pattern molding. Methods such as spray drying,²⁸ flow-focusing capillaries,²⁹ hydrogel templating,³⁰ and soft lithography³¹ are conventional techniques for fabricating polymer microparticles with a small dispersion range. These particles are commonly used in the areas of drug delivery, oil recovery, food processing, and cosmetology. For the case of metals and ceramic materials, the shaping and fabrication of micro- and nano-size particles and devices are performed with micromanufacturing technologies such as mechanical shaping, electron and ion-beams, electrophysical and chemical deposition, lithography, and additive processing techniques.³²

1.2.2 Relevant Techniques

Photolithography

Photolithography is a technique for polymerizing or unpolymerizing patterns based on the selective exposure of optical radiation to a photosensitive or photoinitiated solution to modify its chemical bonds.³³ Photolithography was developed in the mid-1900s³⁴ to achieve submicron-sized features in the semiconductor industry. Wide spectrum UV light can define patterns of ~500 nm, limited by optical resolution. Nonetheless, features < 50 nm can be achieved by using UV laser photolithography³⁵ with techniques such as in-line lithography,³⁶ two photon lithography,³⁷ and multiphoton lithography.³⁸ For features below 30 nm, e-beam lithography has become the preferred technique, capable of reaching sizes of ~10 nm.³⁹

PDMS-based Microfluidics

Microfluidic silicon chips emerged in the 70's with the development of the gas chromatograph and ink jet printers.⁴⁰ Over the past 30 years, lab-on-a-chip technology has incorporated the advances of microfluidic chips, using a transparent and chemically inert cross-linked polydimethylsiloxane elastomer (PDMS, Sylgard 184, DOW Corning, Midland, MI). This integration has helped increment chemical experimentation and analysis in miniature systems.⁴¹

PDMS has become one of the most attractive materials for microfluidic devices due to favorable characteristics such as economic viability, optical transparency, excellent glass adhesion, tunable stiffness, and chemical stability.⁴² Fields including microfluidics, cell biology, lab-on-a-chip and flexible electronics have benefitted from its versatility in fabrication and processability.⁴³

A set of techniques encompassed by soft lithography has been used to fabricate microparticles from a PDMS elastomeric mold, which embosses a pattern from a photopolymerized master mold.

1.3 Selected Technique for the Fabrication of Microparticles

1.3.1 Flow Lithography

Flow lithography techniques began to be developed in 2006, incorporating fundamentals of photolithography and PDMS-based microfluidic methods, for the continuous fabrication of predefined two-dimensional (2D) extruded shapes. Essentially, a photosensitive solution flown through a PDMS microchannel, is exposed in patterned UV pulses that onset polymerization. Flow lithography techniques have evolved to include a variety of set-ups: continuous,⁴⁴ stop-flow,⁴⁵ lock-release,⁴⁶ vertical,⁴⁷ interference,⁴⁸ inclined,⁴⁹ maskless,⁵⁰ curvature,⁵¹ and contact-flow⁵² lithography techniques. The fabrication of predefined shapes from 5–500 μm in relevant length has been demonstrated using flow lithography. Simple shapes such as circles, triangles, hexagons, as well as more complex shapes (figure 1.2) like keys, horns, long-tail particles have been synthesized with flow lithography techniques.⁵³

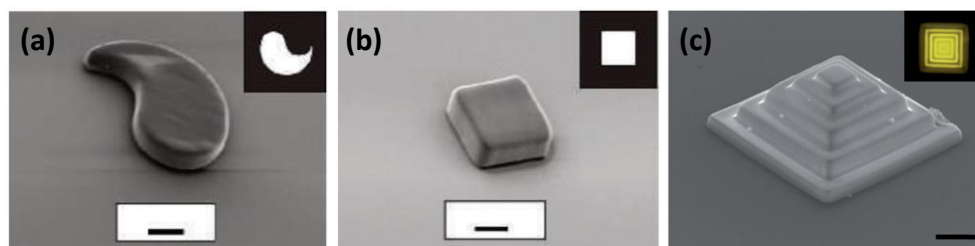


Figure 1.2: SEM images of mask defined shapes fabricated via flow lithography techniques; (a) and (b) were fabricated with continuous-flow lithography and (c) with maskless-flow lithography. Scale bar in image (a) and (b) is 10 μm , and in (c) is 50 μm . Reproduced from refs 44, 50 with the corresponding permissions. Copyright 2006 Nature Publishing Group, 2009 The Royal Society of Chemistry.

1.3.2 Material Requirements

SFL requires a transparent or translucent Newtonian monomer/oligomer solution with a fast UV-crosslinking chemistry capable of polymerizing in less than one second. The viscosity of the solution used should be below 1 Pa·s, to limit the pressure needed to drive in the fluid in the PDMS microchannel device and avoid device debonding.⁵⁴ Satisfying these requirements means there are a limited number of polymer chemistries suitable for SFL processing. Polyethylene glycol

diacrylate (PEGDA) has become the most widely used UV-crosslinkable material for SFL particle fabrication due to its fast UV-crosslinking chemistry, bio-compatibility and ease of chemical alteration making it suitable for a wide range of applications.⁵⁵ Other methacrylated and acrylated materials have also been used, such as hydroxyethylmethacrylate (HEMA)⁵⁶ and tetraethylenglycoldiacrylate (TEGDA),⁵⁷ as ultrafast photopolymerization materials. Nonetheless, there are still several opportunities to augment the palette of materials to be used in flow lithography techniques. One of them is by using preceramic polymeric materials.

1.3.3 Stop-Flow Lithography

Stop-flow lithography (SFL)⁵⁸ is a method that was developed in 2007 by Patrick Doyle research group from Massachusetts Institute of Technology. SFL has been demonstrated to be a fast, versatile, and robust lithography technique for the fabrication of predefined 2D extruded particles. Particles fabricated via SFL acquire a previously designed two-dimensional shape from a planar UV light projection through a photomask and volume thickness along the PDMS microchannel height. A SFL basic setup is composed of an inverted microscope, a UV source, a fluid reservoir, and a microcontroller that coordinates the cycle times. In a typical fabrication session, a photosensitive solution moves through a microfluidic channel until it is stopped, and exposure of a patterned UV light pulse in the milliseconds range starts free-radical chain polymerization of the photosensitive fluid. The fluid flows again to move the polymerized particles out of the generation area to refill it with new unpolymerized solution and prepare the device for a new cycle. The flowability characteristic of the polymerized particles is possible due to the oxygen permeability property of the PDMS microchannel, which terminates polymerization through the formation of peroxide groups at the end of the polymer chain. The 3 main cycles of SFL can be observed in figure 1.3, showing in image (a) the fluid stopping after entering the PDMS microchannel, (b) selective UV polymerization of the photopolymer after UV exposure, (c) the polymerized particles being flushed out of the generation area to prepare the microchannel for a new cycle.

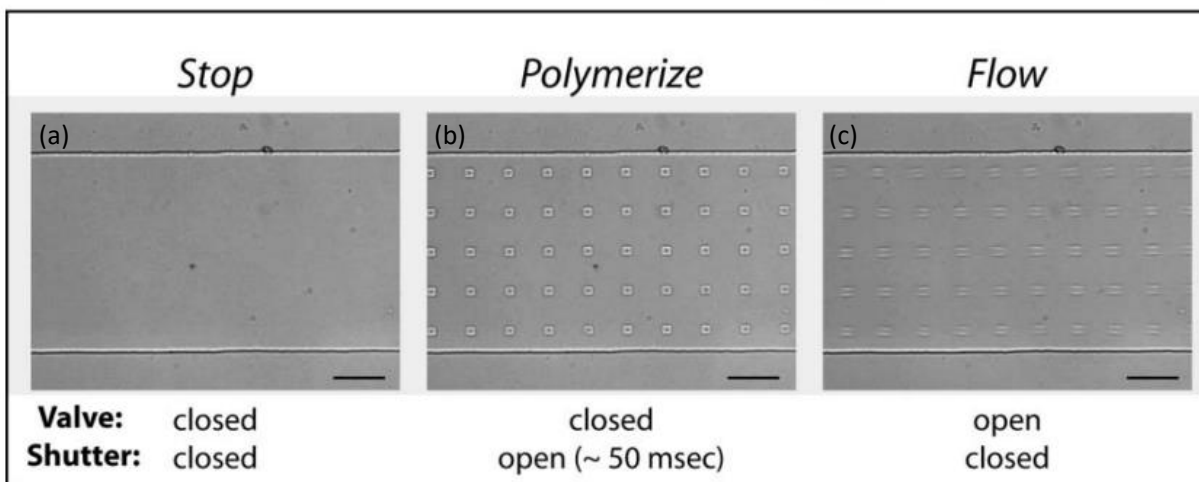


Figure 1.3: Microscope images showing the steps of the SFL fabrication cycle inside the PDMS microchannel device. (a) The first step is the time it takes for the fluid to stop after the input pressure has been released, (b) the second step shows the selective polymerization of the polymer by UV projection through a photomask, and (c) the third step shows the particles being flushed out of the generation area after polymerization. Scale bar is 50 μm in all cases. Reproduced from ref 45 with permission from The Royal Society of Chemistry, copyright 2007.

Hydrogels have been the main materials used to fabricate particles with flow lithography techniques. PEGDA hydrogel is the material of choice due to its excellent rheological properties, biocompatibility,⁵⁹ and ultra-fast UV light polymerization. In recent years, not only polymer particles but also ceramic particles have been fabricated through suspension processing. By loading functional powders into the green polymer matrix, ceramic materials can be obtained after sintering where the polymer matrix is lost and the ceramic powders group together. The first approach to fabricate ceramic microparticles via SFL was made by Shepherd et al.,⁶⁰ by index matching a colloidal silica suspension with dimethyl sulfoxide (DMSO, Fisher Scientific, Hillsboro, OR). The index-matched suspension was then mixed with acrylamide monomer (Acros Organics, Fischer Scientific, Hillsboro, OR), N,N-methylene bisacrylamide (Sigma Aldrich, St. Louis, Missouri), and photoinitiator (Darocur 1173, CIBA, Basel, Switzerland) to add the crosslinking and photosensitive characteristic to the solution. By index match, it acquired a translucent appearance, reducing light scattering and allowing full polymerization throughout the PDMS microchannel device height. Porous and dense oxide structures containing SiO_2 were obtained after partial and full sintering of the microparticles. The particles presented shrinkage due to polymer burn-out. Another research work presented by Baah et al.,⁶¹ showed the fabrication of predefined shape ceramic microparticles of SiO_2 and Al_2O_3 by mixing colloidal suspensions with

PEGDA. The content of the SiO_2 and Al_2O_3 in PEGDA matrix was 20% and 12% correspondingly. Since the loading of the suspensions was lower than the previous approach, it resulted in higher volume shrinkages up to 60%. The polymer was burned out at 600 °C, and the ceramic particles were fully sintered for 8 hours at 1150 °C. Even with higher mass losses, the ceramic microparticles maintained their shape after heat treatment.

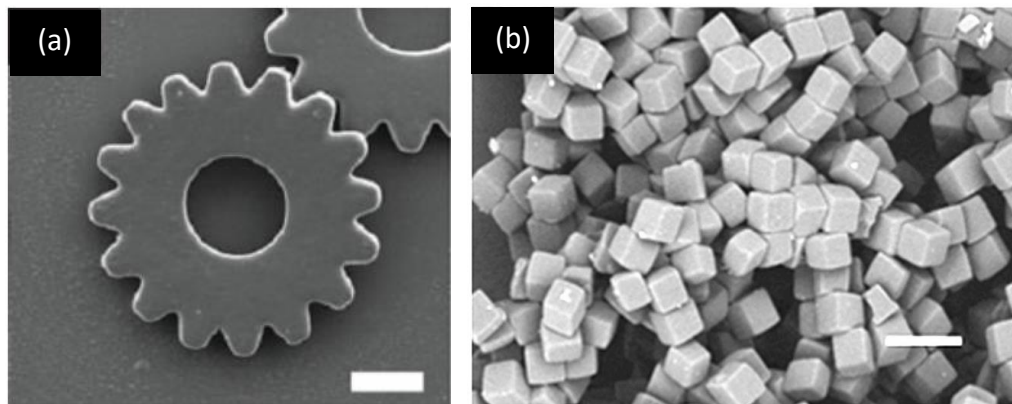


Figure 1.4: (a) SEM micrograph of SiO_2 microgear sintered at 1150 °C fabricated via SFL by Shepherd et al., (b) SEM micrograph of sintered Al_2O_3 cube microparticles sintered at 1450 °C fabricated via SFL by Baah et al. Scale bar in (a) is 50 μm , while in (b) is 100 μm . Reproduced from refs 60, 61 with the corresponding permissions. Copyright 2008 WILEY-VCH Verlag GmbH & Co KGaA Weinheim, 2013 Elsevier B.V.

1.4 Preceramic Polymer Precursors

Preceramic polymers are polymeric materials that upon heat treatment in an inert atmosphere, transform through decomposition or reconfiguration of their chemical bonds into ceramic materials. By treating them initially as polymers, a wider variety of processing techniques can be used to shape them in their green state. Preceramic polymers were first reported in the 60's by Yajima⁶² for the fabrication of ceramic silicon carbide fibers. The most common ceramic materials (figure 1.4) obtained from polymer precursors through pyrolysis heat treatment are SiOC , SiO_2 , SiC , and Si_3N_4 , which have silicon in their chain backbone as the primary element bonded to carbon, oxygen and/or nitrogen.⁶³ Nonetheless, other ceramic materials converted from polymers precursors, such as BN , AlN , B_4C , and SiTiC have also been fabricated.⁶⁴

Preceramic polymers have commonly silicon attached to oxygen, carbon or nitrogen in their backbone with attached side groups that enhance polymerization. When the polymerization reaction starts when the crosslinker or photoinitiator onset reaction triggers, the oligomer side and end groups cross link to create a polymer network. When the polymer is pyrolyzed, the side groups

are evaporated, and the main back bone bond remains. This effect leads to an important reduction in mass, volume and linear dimensions. Final masses commonly yield between 10 and 70 wt% of the initial mass.⁶⁵ Some porosity is expected from the treatment and further heat treatment as sintering may remove porosity as well as increase shrinkage.

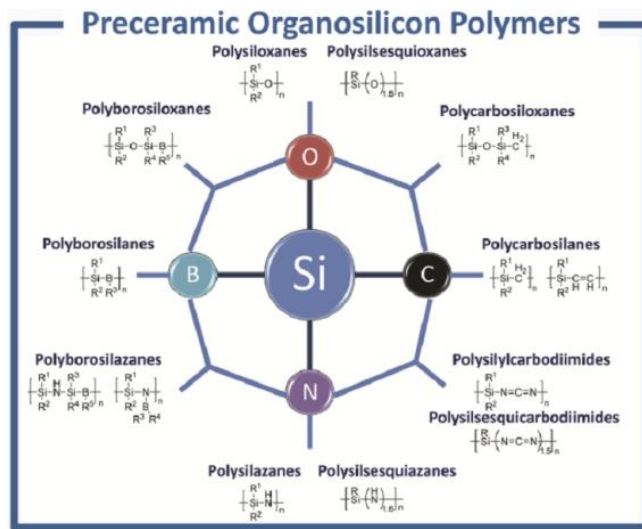


Figure 1.5: Schematic showing the most common preceramic polymer precursors with silicon as the main element in the polymer chain backbone. Reproduced from ref 71 with permission from The American Ceramic Society, copyright 2010.

SiC and Si₃N₄ have been used not only as wear-resistant and abrasive materials but also as semiconductors and light-emitting materials. SiOC has revealed white luminescence⁶⁶ and is also a good candidate as anode material.⁶⁷ Furthermore, it has been shown that silicon-based metamaterials could be used for photonic circuits.⁶⁸ SiOC has presence of carbon in its insulating glass structure, has shown thermal stability and chemical inertness,⁶⁹ gaining significant attention in several research groups in recent years.⁷⁰

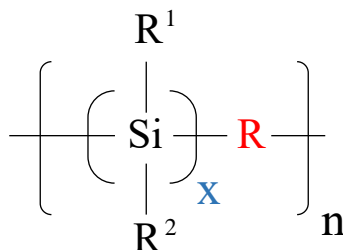


Figure 1.6 Common monomer structure of preceramic polymers with silicon in their backbone, with side groups R¹ and R² that enhance crosslinking but may be lost during pyrolysis. R is oxygen, carbon or nitrogen. X and n are repeating units of the monomer and oligomer respectively.

The shape of preceramic polymers has been defined using 3D printing techniques such as stereolithography⁷¹ and photocurable inkjet printing⁷² to fabricate three dimensional objects. Ceramic pieces in the mm/cm range have been fabricated by converting polysiloxane, polycarbosilane and polysilazane into SiOC, SiC, and Si₃N₄ respectively. Recently, the fabrication of SiOC nanometer-sized pieces with a two-photon laser writing technique has been demonstrated as well.⁷³ These materials have also been used to fabricate solid and hollow ceramic microspheres from a polysilsesquioxane polymer precursor, using flow focusing capillaries.⁷⁴

In this thesis, we introduce preceramic polymer materials to SFL system to fabricate solid and functional ceramic microparticles. Previous efforts to fabricate ceramic microparticles via SFL have used PEGDA as the suspension matrix. We focused on the fabrication of ceramic polysiloxane microparticles via SFL of preceramic materials for further heat treatment transformation into ceramic SiOC particles. The two properties of interest that we focus on in this research work are porosity and magnetism. Porosity can reduce material density and increase surface area for surface modification or chemical attachment.¹⁹ The magnetic functionality allows us to achieve directional control of the particles through external magnetic fields. We envision the continuous fabrication of particles with two properties where one can control directionality and the other can generate the propulsion needed for a particle to flow in a liquid media or serve as drug carrier. By introducing preceramic polymers to SFL, this research expands the range of materials that can be processed with this technique.

2. STOP-FLOW LITHOGRAPHY AND PARTICLE DIMENSIONS VARIABILITY

2.1 Introduction

Stop-flow lithography (SFL) combines aspects of PDMS-based microfluidics and photolithography. It has been used to fabricate polymer and ceramic microparticles, mainly by using polyethylene glycol diacrylate (PEGDA) as solid material or as a matrix to embed nanoparticles. The microparticles fabricated with this method are monodisperse or have a narrow dimension range. However, there are several factors affecting repeatability of particle size and shape. In this chapter, the stop-flow lithography system will be described in detail. Additionally, sources of particle size and thickness variability will also be addressed.

2.2 Stop-Flow Lithography

2.2.1 Set-up and Description

A SFL system (figure 2.1) is mainly composed of the following parts:

- Air pump and chamber
- Microcontroller
- UV filter
- PDMS microchannel
- Shutter
- Inverted microscope
- Photomask transparency
- UV source

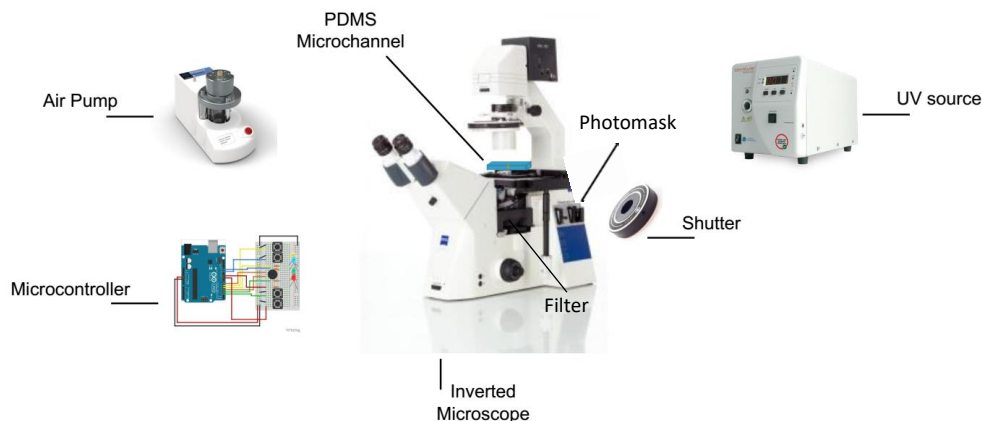


Figure 2.1: Schematic showing the main stop-flow lithography components. A microcontroller coordinates the shutter and the air pump pulses. A UV light source is connected to a shutter that determines UV pulses. The fluid reservoir chamber moves the selected photosensitive fluid into the PDMS microchannel with air pulses controlled with a relay and a solenoid.

SFL is a fabrication technique that functions in repeatable and continuous cycles. SFL is composed of two main processes: UV exposure occurrence, and fluid flow occurrence. Initially, a vial containing the photosensitive material is placed inside a 40 mL fluid reservoir chamber (Mitos, Dolomite©, UK), and connected to an elastomeric polydimethylsiloxane microchannel (PDMS, Sylgard 184, Dow©, Midland, MI) using 20-gauge tubing. The photosensitive material moves with air pressure to the PDMS microchannel device to fill the projection area and prepare the beginning of SFL cycles. The PDMS microchannel is located on an inverted microscope (Axio Observer A1, Zeiss©, Göttingen, Germany) that incorporates a 360–390 nm filter (AT- UV/DAPI Longpass, Chroma, Bellows Falls, VT) and a photomask transparency (CAD/Art Services, Inc., Bandon, OR) with the desired shapes to enact patterned polymerization. UV light (X-Cite 120, Excelitas©, Mississauga, ON) is guided to the inverted microscope's objective rear end (5x, 10x or 20x) where it is transmitted to the shutter (Uniblitz VS25S2ZM1R3-21, Vincent Associates, Rochester NY) and collimating lens. It passes through a patterned photomask transparency located in the microscope, and with controlled triggered UV light pulses polymerization is initiated. Figure 2.2 shows examples of photomasks designed for the photopolymerization of microparticles. An Arduino (ArduinoMega, Arduino©, Ivrea, Italy) microcontroller coordinates on/off pulses in the air chamber using a solenoid valve (McMaster, Elmhurst, IL) and on/off pulses of the UV light (X-Cite 120, Excelitas©, Mississauga, ON) using the shutter drive (VCM-D1 Shutter, VincentAssociates©, Rochester, NY).

In a typical cycle session, when the solenoid valve opens to ambient pressure, the fluid flow stops to start a new cycle. When the fluid is at rest after a brief time, the shutter opens for several milliseconds allowing UV light to pass through the patterned mask to start the selective crosslinking of the photosensitive solution. After polymerization, the solenoid closes, restarting the fluid flow to transport the crosslinked particles downstream. This process is repeated every 1–2 seconds to continuously fabricate crosslinked preceramic polymer microparticles. One cycle time, t_{cycle} , is composed of four sub times: fluid stop time (t_{stop}), exposure time (t_{exp}), dark polymerization time (t_{dark}), and flush out time (t_{flush}).

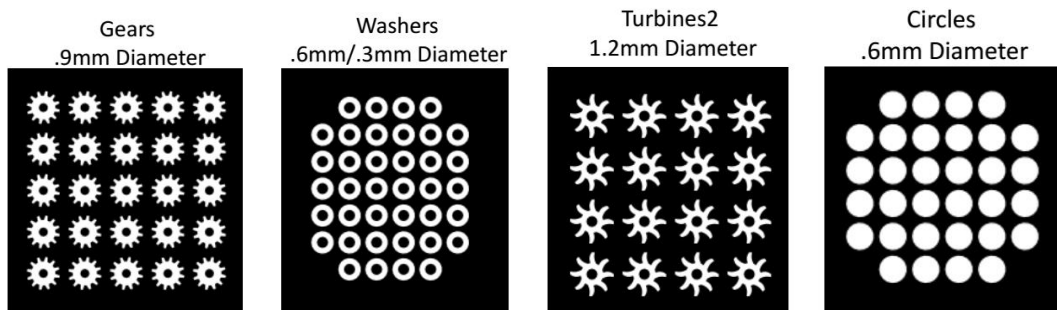


Figure 2.2: Drawings of designed patterns to be printed on a photomask with different shapes and arrays for the fabrication of microparticles via SFL.

Air Source, UV Source, and Microcontroller

In this section, we will describe the characteristics of the air source, the UV source and the microcontroller. For the air source, the source supply came from the main building pipeline with an input pressure of 8 bars. Pressure was reduced to 0.2–1 bar with a compressed air regulator (McMaster, Elmhurst, IL). The solenoid on/off valve connected the air supply to the fluid reservoir and opened or closed upon energization of 120 AC volts, which was controlled with a NO/NC relay that changed its polarity when it was energized with 5 DC volts. For the UV Source, its shutter drive controlled the UV light pulses with an input signal of 5 DC volts. Both DC voltages were fed by the microcontroller. The Arduino model is Mega 2560, with 54 digital input/output pins (of which 15 can be used as PWM outputs) and 16 analog inputs pins. The system is capable of running two solenoids in parallel with equal or different pressures, for a 1–5 inlets microchannel. Figure 2.3 shows a flow diagram of the SFL components and the PDMS microchannel. The DC per pin is 40 mA and the DC for 3.3 V pins is 50 mA. The flash memory is 256 KB of which 8 KB is used for boot loading the system, with a clock speed of 16 Mhz.

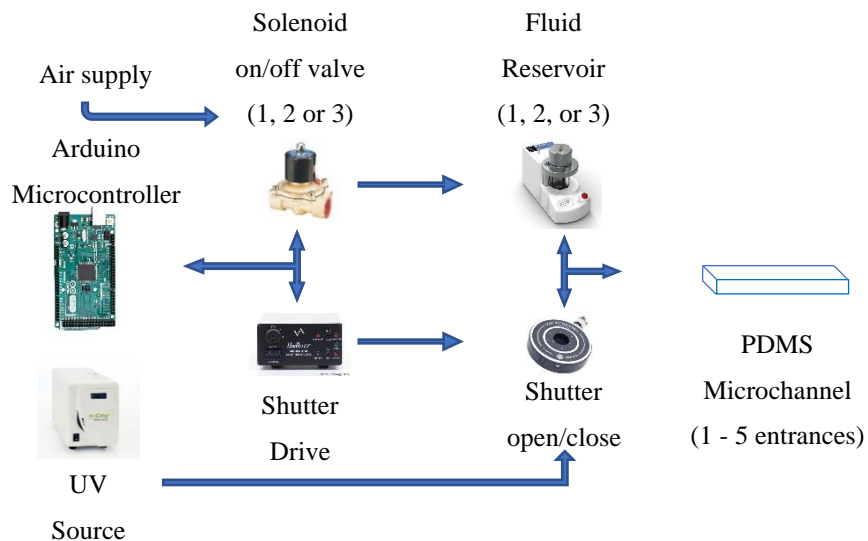


Figure 2.3: Schematic of electrical connections to the solenoid, fluid reservoir, as well as fluid connections to the PDMS microchannel for SFL setup.

The Arduino SFL program is composed of two parts: the first defines the time ranges for the SFL cycles, either with the software or with four integrated potentiometers; the second runs SFL cycles with the defined times. To change from mode one to mode two, a switch setup button has to be activated. Figure 2.4 shows a flow diagram of the Arduino SFL program.

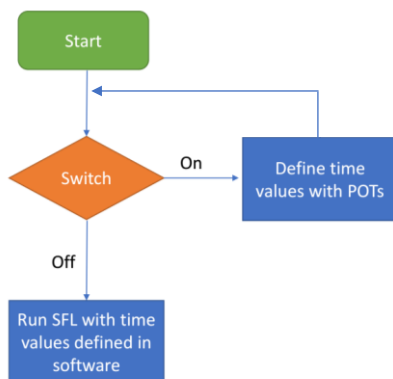


Figure 2.4: Flow diagram of Arduino SFL program instructions to define cycle times with the software or potentiometer and run SFL cycles in continuous loops.

In figure 2.5 a schematic of the Arduino connections with a PC board can be observed, both with the connections to the potentiometer and the connections to the 16x2 8 digit display and I2C circuit interpreter.

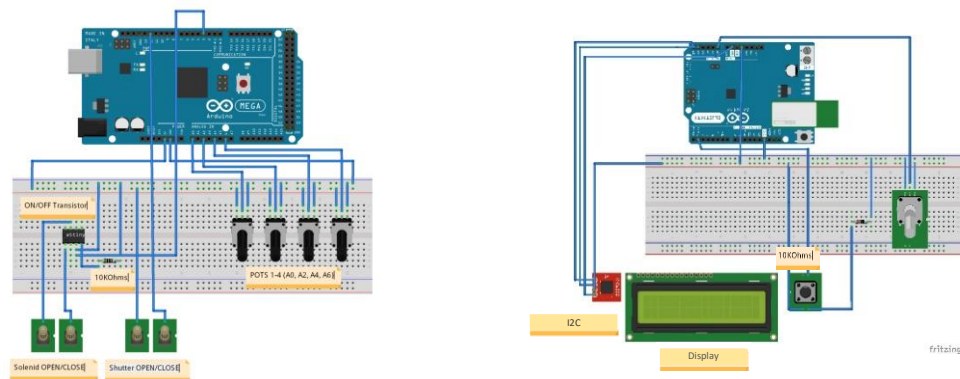


Figure 2.5: Schematic of Arduino microcontroller connections to the relay, potentiometers, switch button, and 16x2 8-digit display with I2C interpreter.

A picture of the SFL box with the microcontroller inside, the potentiometers, the switch button, the banana jacks, and the display can be observed in figure 2.6. Three pairs of banana jacks serve as solenoid one, solenoid two and NO/NC relay connections. The SFL Arduino code can be found in appendix A of this thesis work.



Figure 2.6: Photograph of stop-flow lithography box with microcontroller, potentiometers, switch button, display, and banana jacks.

PDMS Microchannel

Oxygen permeability²³ through the PDMS microchannel is the essential characteristic that allows the continuous fabrication of photopolymerized particles. As the polymerization crosslinking starts and grows through the microchannel, chain growth polymerization terminates

through the reaction of the polymer end chains with free oxygen available in the microchannel walls due to the PDMS gas permeability characteristic. For a PDMS device mixed at 1:10 ratio, an oxygen diffusion coefficient of $6 \times 10^{-10} \text{ m}^2/\text{s}$ and initial inhibition layers of $2.5 \text{ }\mu\text{m}$ were experimentally measured by Dendukuri et al.,⁷⁵ which were independent of the channel height but dependent on photopolymer permeability. Additionally, it has been demonstrated that PDMS permeability ($1\text{E-}12 \text{ mol}\cdot\text{m}^{-1}\text{s}^{-1}\text{Pa}^{-1}$ for CO_2) value depends on whether the layer's thickness is below $50 \text{ }\mu\text{m}$.⁷⁶ However, if permeability of the microchannel needs to be augmented, it is possible by increasing the PDMS mixing ratio.⁷⁷

PDMS microchannel devices were assembled from two partially cured PDMS sections. The top section contained the microchannel silhouette while the bottom section served to close the device. The top section was built by casting PDMS on a mold built on a glass slide (figure 2.7). The bottom section was a PDMS-coated coverslip.

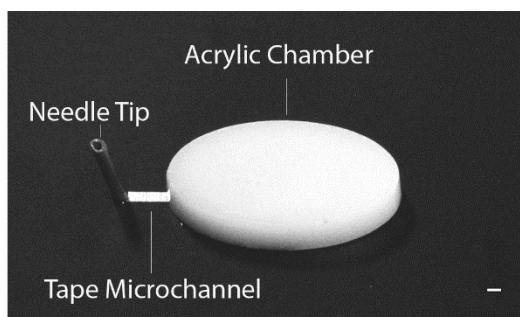


Figure 2.7: Photograph of the microchannel mold made with a self-adhesive vinyl film, an oval acrylic chamber and a 30-gauge needle tip. The scale bar (1mm) is valid along the horizontal centerline of the microchannel mold.

The microchannel negative mold (figure 2.7) was fabricated with a trimmed self-adhesive vinyl film (Vinyl Sheets 12 in., Swisselite, Amazon, ASIN: B06Y5V5VJS) of $1 \text{ mm} \times 3 \text{ mm}$, an elliptical acrylic chamber piece of $17 \text{ mm} \times 10 \text{ mm} \times 3 \text{ mm}$ cut with a laser cutter (Speedy 400 Flexx, Trotec, Plymouth, MI) and a 20-gauge needle tip. Nath et al.⁷⁸ showed a rapid method to prototype microfluidic components by using adhesive transfer tapes. We adapted self-adhesive vinyl films to construct the negative microchannel pattern as a reproducible, versatile, and economical approach. Both the oval acrylic chamber and the needle tip were epoxied to the glass slide at the beginning and end of the vinyl film. The end tip of the microfluidic device (the PDMS microchannel) had a small aperture open to atmospheric conditions. Since the elliptical dome's

volume capacity was much larger than the microchannel volume, it resembled an infinite reservoir with a minimum pressure on the fluid speed in the microchannel.

A two-part PDMS was hand-mixed at a 10:1 monomer to hardener ratio, and after de-airing it in a vacuum chamber, the mixture was poured over the template followed by heating it in an oven at 60 °C for 50 minutes. The PDMS base was cast on a large coverslip using the same PDMS ratio and cured for just 35 min at 60 °C. The partial curing of PDMS⁷⁹ allows for strong bonding between the top section and the base without the need for a plasma cleaning treatment. Once removed from the template, the top part was carefully pressed against the PDMS coated coverslip and left undisturbed for 24 hours, followed by 1 hour at 60 °C to fully cure the device. A 20-gauge stainless steel tapered syringe tip (Luer Lock Dispensing Needle, McMaster-Carr, Elmhurst, IL) was inserted on one end of the PDMS channel to serve as input for the preceramic monomer solution.

2.2.2 Material Selection

A SFL system requires a liquid, photosensitive, and translucent material able to undergo ultra-fast polymerization. We selected a preceramic polymer material to be used in SFL system, for the fabrication of ceramic microparticles. The photosensitive material in the present research was the UV-curable silicone TEGO RC® 711. The photoinitiator DMPA (2,2-Dimethoxy-2-phenylacetophenone 99%, Sigma-Aldrich®, St. Louis, MO) was added to the preceramic solution to accelerate its UV photosensitive capability.

2.3 Particle Dimensions Variability

2.3.1 Introduction

The fabrication of microparticles using SFL is an attractive technique for continuously generating predefined shape particles in an oxygen-permeable elastomeric microchannel device. PDMS microchannel molds are usually fabricated following SU-8 photoresist spin coating and contact photolithography. A clean environment is commonly aimed to avoid mold contamination and variability. We adapted an alternative method to fabricate our PDMS molds by using tape molding. The molds were fabricated in a laminar hood from vinyl films which reduced fabrication costs but affected particle dimensions repeatability. The variability of particle size and height is

due to several factors. The three primary sources that we identified were mold variability, UV light projection, and PDMS oxygen diffusion/consumption. Microchannel molds made from tape or polymer films may impact particle thickness. Additionally, light projected with a gaussian intensity distribution⁸⁰ may also affect particle dimensions.

2.3.2 Microchannel Mold

Vinyl Tapes

Diverse tapes and vinyl films were tested as candidates for the fabrication of PDMS molds. By transferring a tape from the reel to the glass slide, some of its adhesive may remain in the reel. Also, by applying pressure when adhering the tape to the glass slide, the adhesive might get compressed unevenly. For these reasons, reel tapes were avoided. Instead, self-adhesive and non-adhesive vinyl films were used. Nine vinyl films with and without adhesive were adhered to a clean glass slide before testing their surface profile. The films were pressed with a force of 7–12 Newtons on a glass slide, zero times, three times and ten times. The nine additional vinyl films were first tested with a granite gage stand to obtain an estimate of their thickness and variability. From these nine vinyl films, two were selected for further testing with a profilometer.

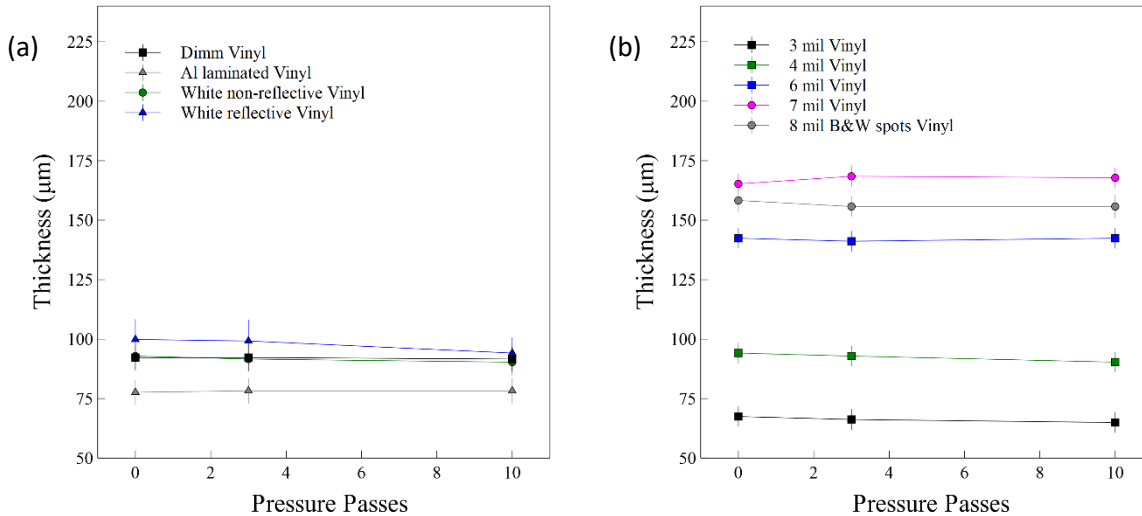


Figure 2.8: Vinyl film thickness (a) with and (b) without adhesive, tested for different pressure passes with a granite base gauge meter.

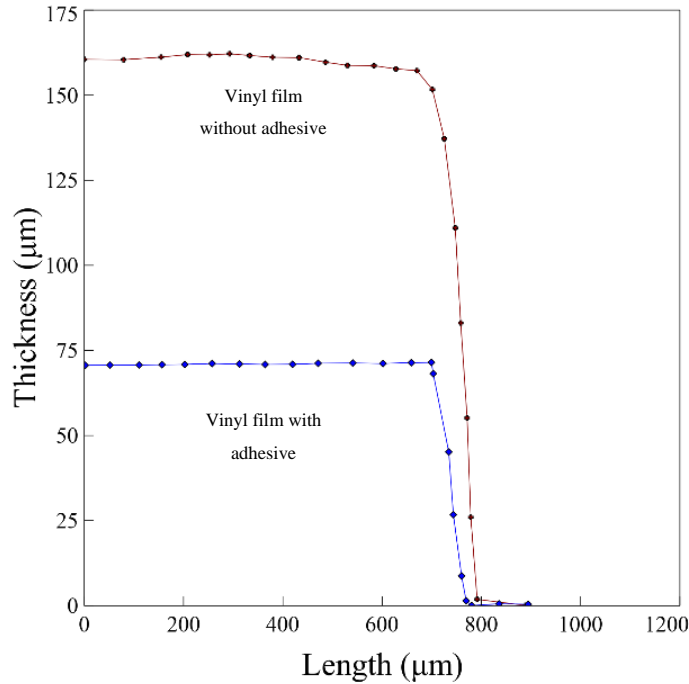


Figure 2.9: (a) Vinyl films thickness profile of two films, one with and one without adhesive, and (b) shows pictures of vinyl films with arrow profile needle tip scanning line.

Figure 2.8 (a) shows the variability of four different vinyl films with adhesive when pressed repeatedly. Some of the films varied when pressure was applied. Some vinyl films without adhesive were subject to bubble trapping when adhering them to a glass slide, affecting the microchannel mold height. Two vinyl films, one with adhesive and one without, were selected for further testing using a P-7 Stylus Profiler (Tencor, College Station, TX). Both showed a low degree of variability, as shown in figure 2.9. Both vinyl films are good candidates for use as tape microchannel molds with $153 \pm 5 \mu\text{m}$ and $75 \pm 5 \mu\text{m}$ thickness respectively. A final test, figure 2.10, was performed with a confocal microscope (FV1000, Olympus, Tokyo, Japan) to analyze the self-adhesive vinyl film thickness. A uniform height was observed on the left of the sample where no compression was exerted. However, on the side where compression was effected by cutting the film with a razor blade, accumulated adhesive increased the height of the tape up to $25 \mu\text{m}$. When these vinyl tapes are used, the edges of the tapes should be avoided, and the central region of the tape should be used for the projection area.

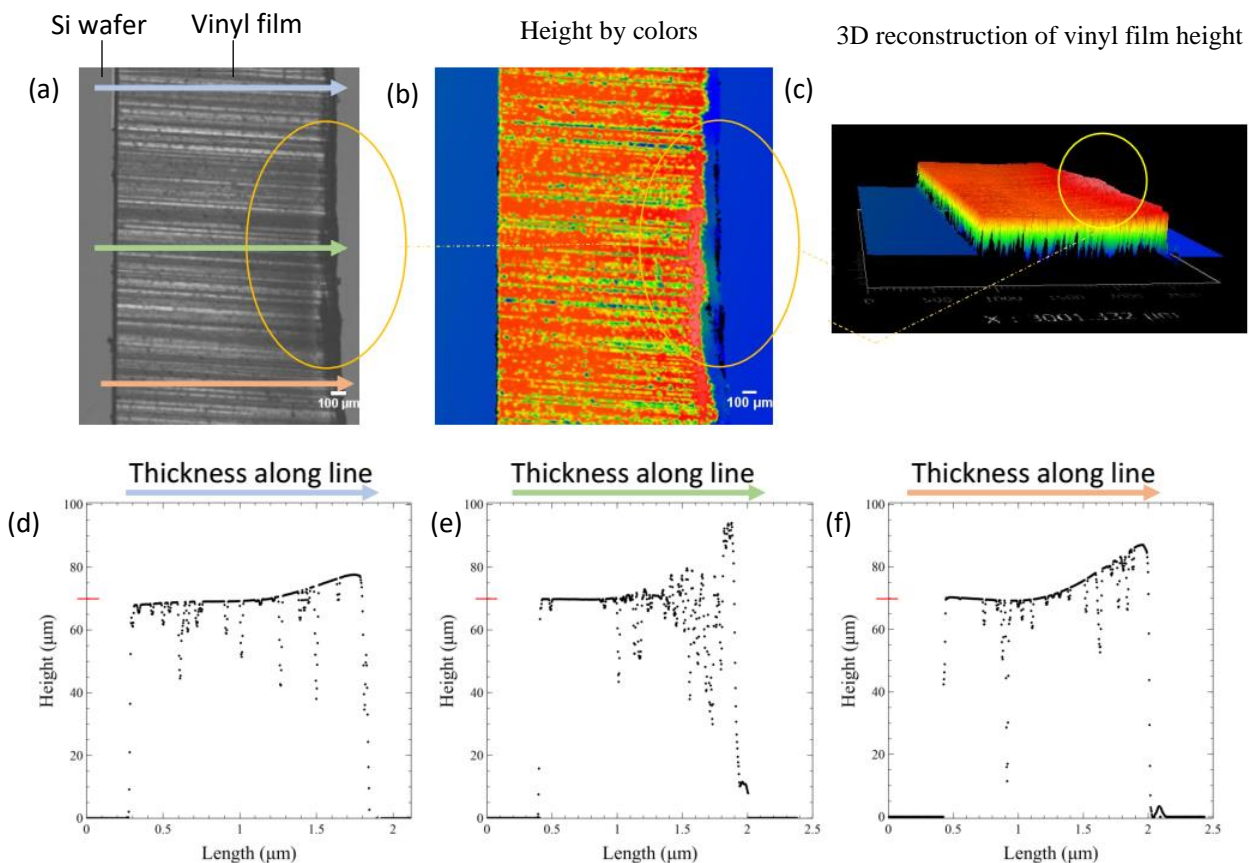


Figure 2.10: (a) Top view image of vinyl film cut with a razor blade adhered to a silicon wafer; (b) and (c) show vinyl height comparison by colors; (d), (e), and (f) plots correspond to the arrows in (a), delineating the scanning direction. Measurement lines were performed with a confocal microscope for a section of a vinyl film with adhesive. The height of the vinyl film is 70 μm except the right size where the film was cut with a razor blade, showing adhesive agglomeration.

2.3.3 UV Source Variability

Light Source Lifetime

The second factor affecting particle dimensions is UV variability, projection variation and time variation, which will be analyzed in this section. The UV source used was a wide-spectrum X-Cite 120 lamp (Excelitas®, Mississauga, ON). It functions with a metal halide lamp with four intensity levels that are selected manually by changing the aperture of the source. The recommended lifetime of a metal halide bulb is 2000 hours, although it can last for up to 4000 hours. The behavior of the lamp during its lifetime may affect UV light intensity. Figure 2.11 shows the degradation of the metal halide bulb as working time increases. Additionally, a warmup time is necessary for the lamp to reach an equilibrium state.

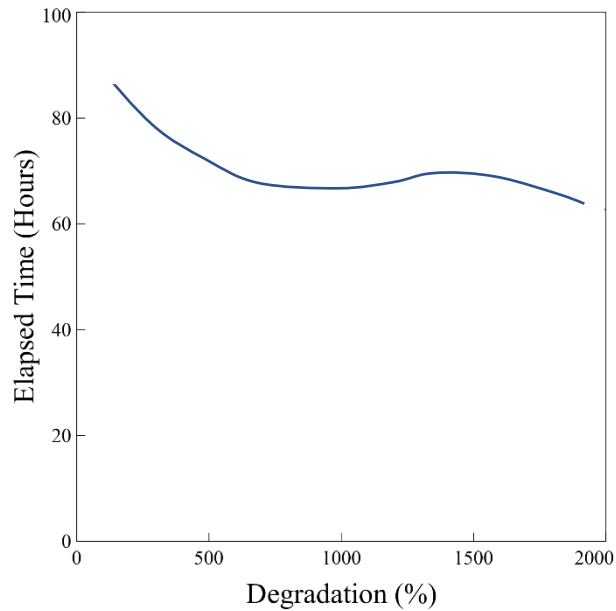


Figure 2.11: Showing degradation time vs. bulb elapsed time (hours), for UV light source X-Cite 120, reconstructed plot from supplier's technical sheet.⁸¹

The lamp works with DC duty cycles after AC conversion. The lamp RMS voltage is 85V with 1.4 amps of current with a square wave signal and a duty cycle of $d = 0.5$. The maximum lamp voltage is 115 V RMS, and the lamp drive frequency is 150 Hz, with a square wave ramping up every 6.6 ms. The UV light is transmitted through a light guide to the shutter; any bending or kinking of the collimating adapter will affect the light distribution.

UV Planar Gaussian Distribution Projection

The UV projected from a single source (X-Cite 120) on an illuminated area is not uniform; rather, it follows an intensity gaussian distribution projection. The total projected area after the collimating lens at the rear end of the used microscope has 13 mm in diameter, and the selected reduced projected area has 5 mm in diameter. The reduced projected area after 20x magnification has a diameter of 625 μm . By reducing the projected area, relative variability is reduced by $< 20\%$. Figure 2.12 shows the reduced area (the blue circle) and the relative intensity variability through the diagonal length (the orange arrow).

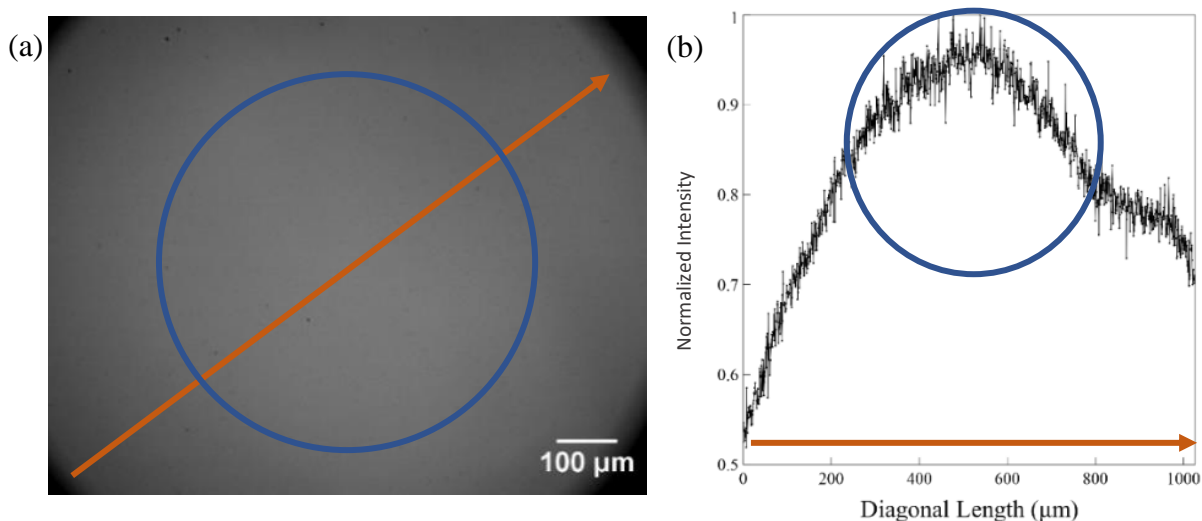


Figure 2.12: (a) Optical image showing microscope observation area, and the reduced projected area in the blue circle. (b) Normalized intensity variation through the diagonal length (orange arrow).

Within the reduced projection area, three different masks with a different number of hexagon particles were projected, measured, and compared. The projected hexagons with their corresponding sizes can be observed in figure 2.13. It is suggested by Decker et al.⁸² to use the highest UV light intensity level to achieve a higher rate of bond conversion.

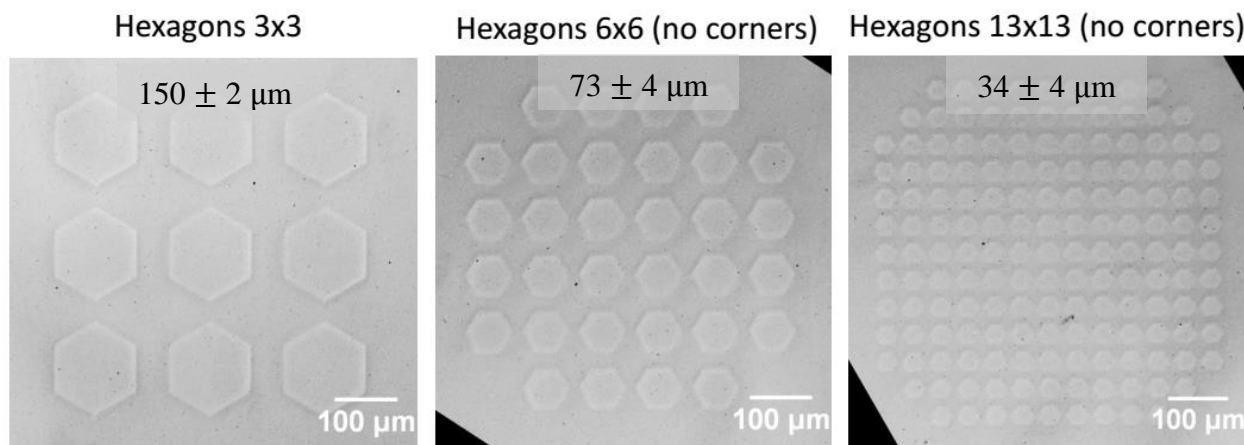


Figure 2.13: Optical images showing fabrication of hexagonal shape particles after UV patterned exposure through 3 different masks with increasing number of shapes. Values within the image represent the mean diagonal dimensions of the hexagons for a given mask.

Time-Dependent Intensity Variations

The next intensity variability observed was related to time, referred as duty cycle. Even though the duty cycle of the lamp is 6.66 ms with a square wave at 150 Hz, the obtained intensity average plot suggests different intensity peaks at the stated duty cycle. The average intensity of the UV light was recorded with a fast camera every 2 ms. It can be observed in figure 2.14 that the average relative intensity fluctuates every duty cycle, where the recorded time was 200 ms. Intensity variations will affect the formation of photoinitiator radicals and hence particle dimensions through cycle times.

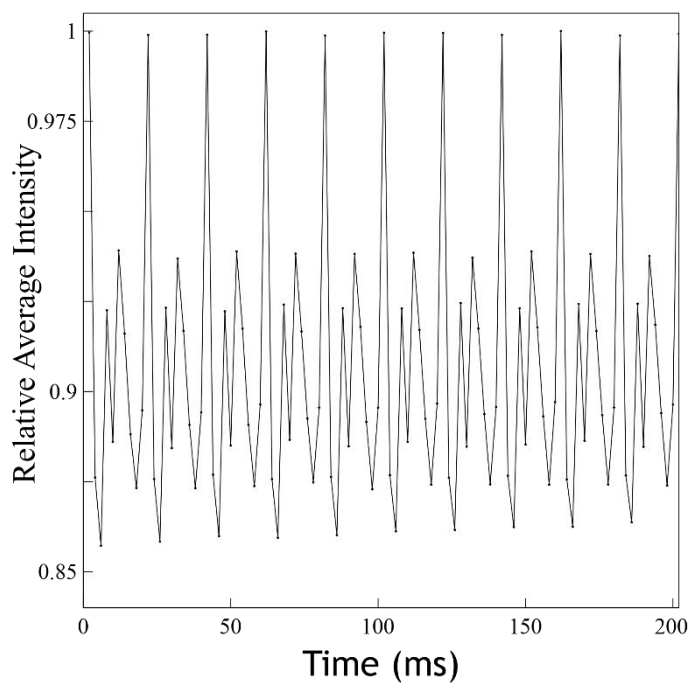


Figure 2.14: Relative average UV intensity vs. time, plotted for 200 ms, showing peak variation for a square wave with a frequency of 150 Hz.

2.3.4 Oxygen Depletion Model

The last source of particle dimension variation was thickness reduction with incremental cycle times. This variability is related to the state of the oxygen inhibition layer thickness, which is a dynamic process. The layer's thickness may increase or decrease, depending on the diffusion and radical consumption rates. Additionally, the transmittance of UV light through the PDMS microchannel may be affected after several cycles from unreacted radicals getting attached to the PDMS structure.

The amount of oxygen in the PDMS walls will change depending on the oxygen diffusion characteristic of the oligomer/PDMS and oxygen consumption of the radical species. If oxygen is diffused at a similar rate at which it is consumed by the radical species, the oxygen inhibition layer may become constant. The Damköhler number, Da , is a guide to find an equilibrium state between the reaction rate and mass transport rate, shown in equation 2.1, where k_o is the radical-oxygen reaction rate, H is the height of the microchannel, $O_{2,eqb}$ is the equilibrium concentration of oxygen in the monomer, k_t is the radical-radical chain termination rate, and D_0 is the diffusivity of oxygen in the monomer.

$$Da = \frac{\text{Reaction rate}}{\text{Mass Transport rate}} = \frac{k_o^2 H^2 [O_{2,eqb}]}{2k_t D_0} \quad \text{Eq. 2.1}$$

Depending on the characteristics of the polymer, polymerization rates, diffusivity constant and equilibrium oxygen content, the oxygen inhibition layer can reduce if it is consumed faster than it is diffused, or it may grow if the oxygen concentration is higher than the equilibrium value. Figure 2.15 shows that by tuning the amount of photoinitiator radical species in the photosensitive solution, particle thickness throughout fabrication cycles may vary. We tested PEGDA 400 with 2 wt% and 5 wt% of Darocur 1173 photoinitiator and TEGO RC® 711 with 2.5% and 5% of Irgacure 651 photoinitiator.

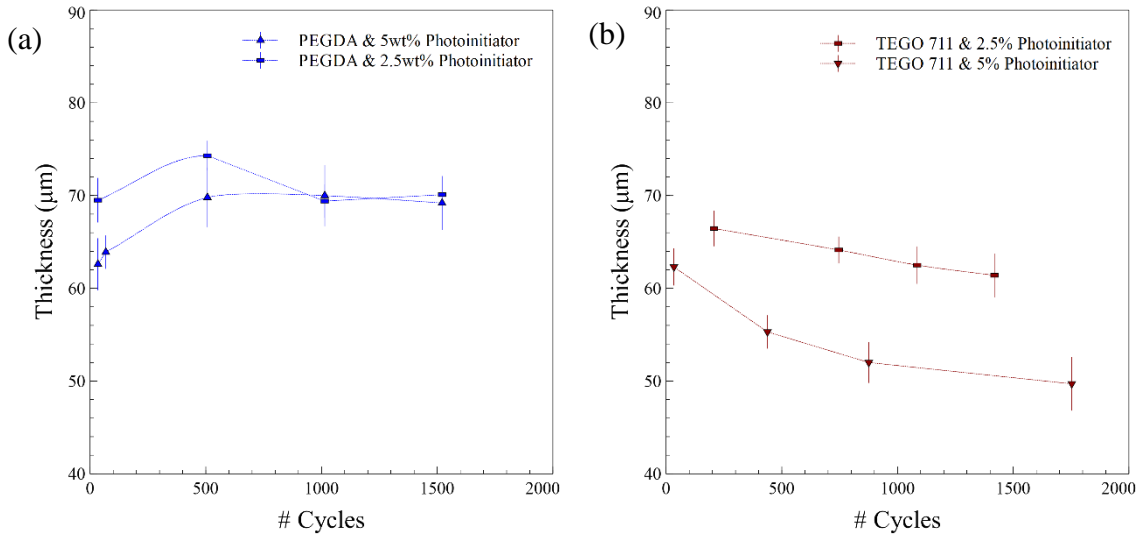


Figure 2.15: Thickness variation of (a) PEGDA and (b) TEGO RC ® 711 as number of fabrication cycles increased.

The oxygen consumption at the PDMS walls, where $z = 0$, for a continuous pulse of UV exposure can be modeled with equation 2.2, derived from the rate of radical production, the rate of radical consumption, and the oxygen consumption equations.⁷⁵ The equation was modeled for PEGDA, since their parameters are known, for the case of three different photoinitiator concentrations. It can be noted in figure 2.16 that oxygen concentration over time at the interface gets consumed faster when the amount of photoinitiator increases. When there is more photoinitiator, more radicals are generated, meaning more oxygen will be consumed. The parameters used to model equation 2.2. can be found in table 2.1.

$$\frac{\partial [O_2]}{\partial t} = \frac{k_o}{2k_t} [k_o [O_2]^2 - [O_2] \sqrt{(k_o [O_2])^2 + 4k_t \phi \epsilon [PI] I_0}] \quad \text{Eq. 2.2}$$

Table 2.1: Polymerization rate parameters for PEGDA.⁷⁵

Parameter	Symbol	Value	Units
Propagation rate	k_p	25	mol ³ /(mol s)
Termination rate	k_t	2520	mol ³ /(mol s)
Inhibition rate	k_o	5.00E+05	mol ³ /(mol s)
UV intensity	I_0	1.50E-02	E/(m ² s)
Photoinitiator []	$[PI]$	168	mol/m ³
Extinction coefficient	ϵ	1.6	m ³ /(mol m)
Oxygen concentration	O_2	1-1.5	mol/m ³
Quantum yield	ϕ	0.6	-

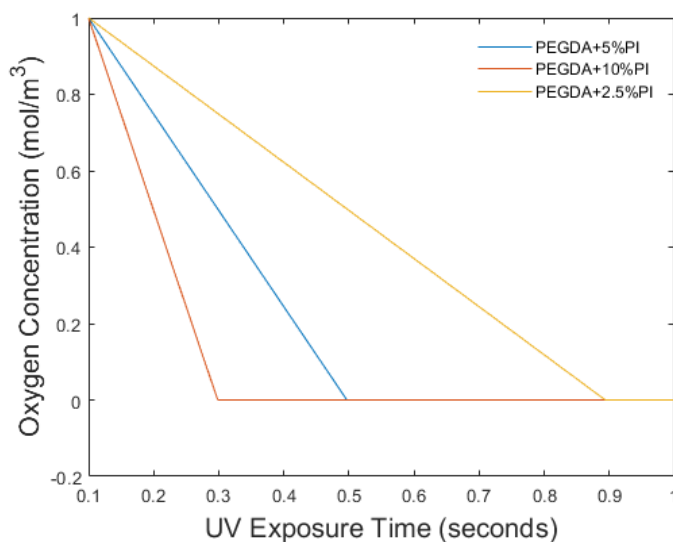


Figure 2.16: Oxygen concentration as a function of time for PEGDA with addition of three different photoinitiator concentrations, 2.5 wt%, 5 wt% and 10 wt%.

2.3.5 Conclusions

Stop-flow lithography (SFL) is a fast, and versatile technique to fabricate microparticles with defined shapes. By introducing preceramic polymers to SFL, polymer shapes can be easily molded and after collection, washing and drying they can be converted to ceramic particles via pyrolysis. PDMS oxygen diffusion characteristic allows cycle repetition by avoiding particle sticking on the PDMS microchannel walls. An Arduino microcontroller was connected to a UV shutter drive and a solenoid relay to control UV pulses and air pulses to coordinate cycle times for SFL fabrication. Vinyl films are a good, replicable, inexpensive and versatile way of fabricating microchannel molds to be used for SFL fabrication method. By selecting a type of vinyl film, its thickness will determine particle height. 2D shapes can be predefined by designing a mask array that will pattern UV light. Three main sources of thickness variation were identified: vinyl mold variability, UV light variability, and oxygen diffusion/depletion competition in PDMS microchannel. Additionally, as time progresses, absorption of UV light through the PDMS device increases due to photoinitiator byproducts, leading to a reduction in photons transmitted to the solution. Particle size variability cannot be avoided but it can be minimized. By mitigating variability, particle can have a narrow size distribution.

3. FABRICATION OF CERAMIC MICROPARTICLES FROM PRECERAMIC POLYMERS VIA STOP-FLOW LITHOGRAPHY

3.1 Introduction

Fabrication of solid and ceramic microparticles via Stop Flow Lithography (SFL) has been mainly achieved by using acrylated or methacrylated polymers. Polyethylene glycol diacrylate (PEGDA) has been the hydrogel of choice due to its fast UV-crosslinking property, biocompatibility, hydrophilicity, and viscosity of 57 cSt.⁵⁵ It has been mixed with other polymers and/or nanoparticles to fabricate composite particles with enhanced functionalities such as magnetic,⁸³ pH,⁸⁴ light,⁸⁵ and temperature⁸⁶ sensitivity. Besides polymers, several approaches have been developed to fabricate ceramic particles using SFL. In most cases an index-matched suspension or low volume fraction ceramic suspension with a UV-crosslinkable polymer acting as the binder are used to make ceramics particles via SFL. The polymer/ceramic crosslinked particles are then dried and sintered to thermally remove the binder and densify the ceramic particles. There is a need for new SFL compatible chemistries in particular those that permit the fabrication of ceramic particles with well-defined shapes and functionalities.

In this work we aim to expand the palette of SFL compatible chemistries using preceramic polymers to fabricate ceramic particles. Ceramics are traditionally made via powder processing. However, in polymer-derived ceramics, preceramic polymers with a Si-backbone containing atoms such as carbon, boron, and nitrite are shaped using standard polymer processing techniques followed by pyrolysis to form ceramics such as SiC, SiO₂ and Si₃N₄.⁶³ The advantage of polymer-derived ceramics is that they are processed as polymers, enabling the fabrication of complex shapes and coatings that are hard to make via traditional methods. In this research study we used a commercially available UV-crosslinkable acrylated-polysiloxane as the preceramic polymer to fabricate silicon oxycarbide (SiOC) glass ceramic particles via SFL. This clear monomer, trade name TEGO® RC 711, is used as a fast UV-crosslinking adhesive with a viscosity of 0.59 Pa·s making it suitable for SFL processing. A simple SFL system was assembled to fabricate continuously the UV-crosslinked preceramic polymer particles with shapes including triangles, hexagons and gears with sizes ranging from 106 to 209 µm and 60 to 77 µm thicknesses. The preceramic particles were harvested from solution followed by pyrolysis at 1000 °C in an argon atmosphere to obtain SiOC glass particles. Particles were fully characterized before and after

pyrolysis via Optical Microscopy, SEM, X-Ray and FTIR. As is common in non-optimized preceramic polymers the particles shrank over 80% linearly during pyrolysis. Usually this excessive shrinkage is detrimental in ceramic processing but in SFL, it permits the fabrication of smaller particles without affective particle shape or inducing cracking. Overall, this work demonstrates a robust path for the fabrication of ceramic particles with specific shapes from preceramic polymers via SFL.

3.2 Experimental Section

3.2.1 Materials, Characterization, and Methods

An acrylate-modified methylsiloxane (TEGO® RC 711, Evonik®, Richmond, VA) with a viscosity of 0.59 Pa·s served as the UV-crosslinkable preceramic monomer. The photoinitiator (2,2-Dimethoxy-2-phenylacetophenone 99%, Sigma-Aldrich®, St. Louis, MO) (DMPA) with an initiation peak at 341 nm was added to the preceramic monomer solution at a 2.5 wt% concentration. Reagent grade isopropanol (Sigma-Aldrich, St. Louis, MO) was used to remove excess unreacted monomer from the crosslinked preceramic polymer particles. Polydimethylsiloxane (PDMS, Sylgard 184 Silicone, Dow Corning, Midland MI) was used to fabricate the SFL microfluidic device. SFL particle fabrication was carried out in an all-PDMS microfluidic device fabricated with a 2-side mold (A+B), where side A included the microchannel feature, and B served as the bottom cover base.

3.2.2 SFL Setup and Operation

A simple SFL system was assembled on an inverted microscope (Axio Observer, Zeiss America, Peabody, MA, USA) fitted with a broad spectrum UV light source (X-Cite 120, Excelitas®, Mississauga, ON), a 360–390 nm filter (AT- UV/DAPI Longpass, Chroma, Bellows Falls, VT), and a shutter (Uniblitz VS25S2ZM1R3-21, Vincent Associates, Rochester NY) following the setup developed by Dendukuri et al.⁴⁵ A photomask was designed (Autocad, Autodesk Inc., Sausalito, CA) and printed (CAD/Art Services, Inc., Bandon, OR) with 3x3 and 5x3 arrays of transparent geometric shapes including hexagons, triangles, and gears with 1.20, 1.04, and 0.88 mm relevant lengths respectively. The relevant length is being defined as the longest

end to end distance for a given shape. For the hexagons, the relevant length is the largest width; for the equilateral triangles, the relevant length is the altitude or height; and for the gears, the relevant length is the outer diameter.

The length of the crosslinked particles is a result of the mask shape size and the objective used. A 20x objective was used for the triangles and hexagons mask, and a 10x objective for the gears mask. The polymerization/crosslinking process was captured using a fast camera (Fastcam Mini UX100, Photron, Tokyo, Japan). Polymerized preceramic particles and uncrosslinked solution were recovered on the filtering mesh that drained most of the uncrosslinked solution for 12-20 hours. Subsequently, particles were transferred into a hydrophilized vial for solvent-exchange with IPA (Isopropanol alcohol). The vial containing the particles and IPA was hand stirred for few seconds before leaving them unperturbed to allow particles to sediment. IPA was replaced few times within the same vial and particles were collected with DI-H₂O and transferred to a different hydrophilized clean vial for further cleaning. The previous process was repeated 3 times. This cleaning process step was performed within 1 hour and was crucial to avoid particle deformation and to maintain particle shape definition. Particles in the washing solution (IPA) were imaged with optical microscopy. It is recommended to complete the bond conversion of the formed polymer microparticles. It can be with a post UV-treatment while they are immersed in a milder cleaning solution, as diphenyl ether, or by washing them with peroxide solution. After completion of the cleaning step particles were placed on a glass slide on a laminar hood where they dried for few weeks before pyrolysis.

3.2.3 Preceramic Particle Pyrolysis and Characterization

Dry preceramic particles were pyrolyzed in an alumina crucible coated with Au-Pd placed in a controlled argon atmosphere furnace (Lindberg54352, Lindberg, Riverside, MI) for 1 hour at 1000 °C with a ramping rate of 10 °C/min and cooled down to room temperature at 2 °C/min. Temperature was held at 440 °C and at 510 °C for 5 minutes. During pyrolysis, the preceramic particles are converted to oxycarbide glass (SiOC). The shape and size of the particles before and after pyrolysis were imaged via optical microscopy (Axio A1, Zeiss®, Gottingen, Germany) and scanning electron microscopy (Quanta FEG, Thermofisher, Hillsboro, OR). Their width and thickness were obtained by measuring over 50 particles via digital analysis of optical and SEM images. Values reported are within 95% of confidence interval. Particle composition was studied

before and after pyrolysis with FTIR while their glassy phase was confirmed using X-Ray diffraction (D8 Focus, Bruker, Karlsruhe, Germany). Dry SiOC particles were re-dispersed in DI-H₂O with the aid of an ultrasonic bath.

3.3 Results and Discussions

3.3.1 Cycle Times

Preceramic particles were successfully fabricated using SFL as shown in figure 3.1. A typical particle generation session started by imposing 0.5 bar of pressure to the preceramic solution inducing fluid flow and filling the microfluidic device. SFL times are exposure time (t_{exp}), dark polymerization time (t_{dark}), flush out time (t_{flush}), and stop time (t_{stop}). They were experimentally optimized to obtain fully crosslinked particles.

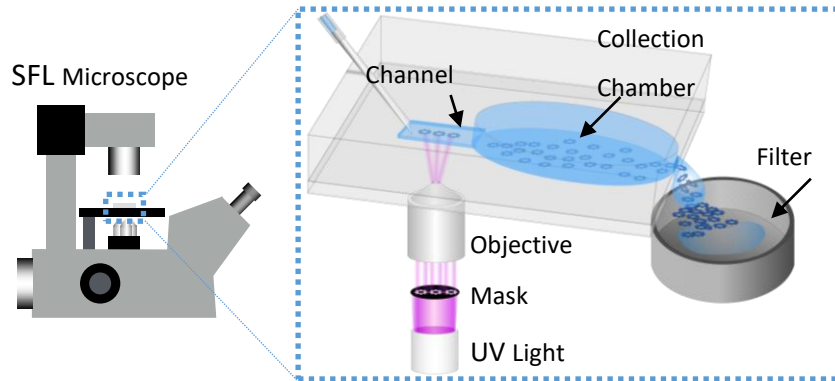


Figure 3.1: Schematic of SFL system showing the PDMS channel device with the photosensitive solution being flowed after UV light has been exposed through the microscope objective. Crosslinked particles and excess uncrosslinked solution are recovered in a filtering mesh after generation.

The t_{exp} and t_{dark} were 0.05s and 0.09s respectively, and both times were estimated from direct observation of particle formation using the fast camera. A $t_{\text{flush}} = 0.35$ s was necessary to move the crosslinked particles downstream with a flush out pressure of 0.5 bar. t_{stop} was ~ 0.9 seconds for a PDMS microchannel device with a length of 4 mm, with a width of 1 mm and a height of 75 μm . It can be observed in figure 3.2 (a) the theoretical t_{res} and experimental t_{stop} for PDMS microchannel devices where length increases from 3 to 6 mm, while the width and the height are kept constant. Figure 3.2 (b) shows t_{dec} for different input pressures in the fluid reservoir. It is shown in figure 3.2 (a), that for a microchannel length of 4 mm, the 3 arrows (red, black and

blue) correspond to the three different times ($t_{\text{res}} + t_{\text{dec}} + t_{\text{rtf}}$) to account for the total time for t_{stop} . The equations used to calculate $t_{\text{dec}} + t_{\text{res}}$ are discussed below.

t_{stop} is the time that takes for the fluid to stop moving after the microfluidic device equilibrates to atmospheric pressure when the solenoid closes. t_{stop} is composed of 3 main times: $t_{\text{dec}} + t_{\text{res}} + t_{\text{rtf}}$, where the time taken for the air dead volume to decompress is known as t_{dec} ; the time that it takes for the PDMS device to recuperate after expansion is known as t_{res} ; and the time that it takes for the tubing and fittings to recuperate after expansion is known as t_{rtf} . For t_{dec} ,⁸⁷ equation 3.1 demonstrates the time taken for the compressed air mass to achieve equilibrium conditions for chamber with an exit nozzle for an ideal gas with non-choked conditions, where ρ is the density of the air, V is the dead air volume, R is the ideal gas constant, T_0 is equilibrium temperature, A is the cross sectional area of the exit nozzle, P_0 is the initial pressure, P_f is the final pressure and k is a constant with value of 1.4.

$$t_{\text{dec}} \sim \frac{\rho V \sqrt{RT_0}}{AP_0} \left(\frac{2k}{k-1} \left(\frac{P_f}{P_0} \right)^{2/k} \left(1 - \left(\frac{P_f}{P_0} \right)^{(k-1)/k} \right) \right)^{-1/2} \quad \text{Eq. 3.1}$$

For t_{res} , Dendukuri et. al.⁴⁵ showed that this time is proportional to the microfluidic microchannel device dimensions (L,W,H) as $\frac{\eta L^2 W}{E H^3}$, where the fluid viscosity is η and the elastic modulus of the PDMS device is E .

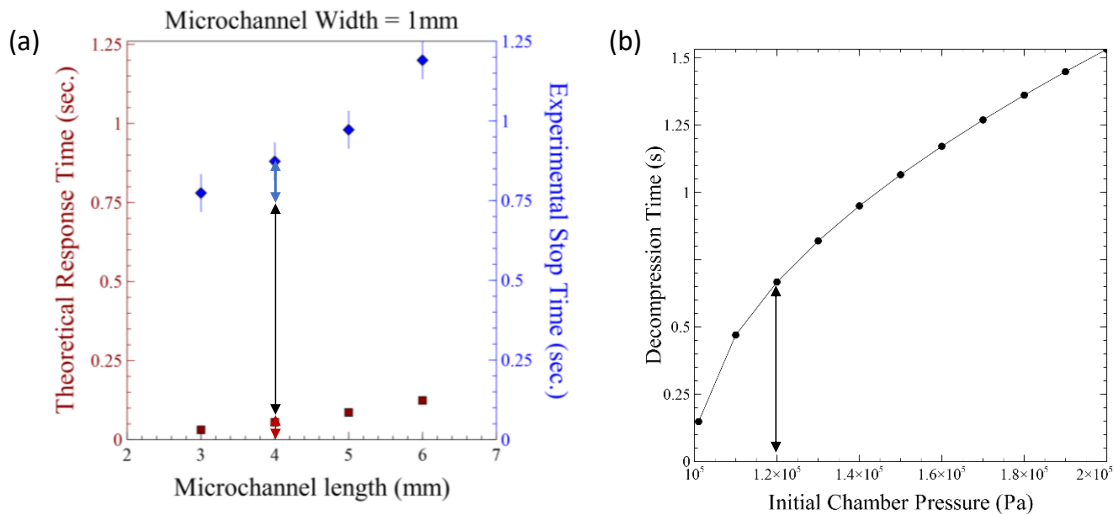


Figure 3.2: (a) Theoretical response subtype (t_{res} in red) and total experimental stop time (t_{stop} in blue) for microchannel length of 3, 4, 5, and 6 mm. The 3 arrows show the subtimes ($t_{\text{res}} + t_{\text{dec}} + t_{\text{rtf}}$) of stop time. (b) Decompression time vs. initial chamber pressure for the fluid reservoir. The black arrow shows the decompression time (t_{dec}) for an input chamber pressure of 1.2 E5 Pa.

The flow speed profile, equation 3.2, of the solution through the PDMS microchannel can be modeled with the Navier-Stokes equation for steady state fluids with no-slip condition at the wall boundaries for ratios $h/w < 0.35$,⁸⁸ where u_x is the speed of the fluid at any point in the microchannel, h is the height of the microchannel, L is the length of the microchannel, w the width of the microchannel, Δp is the pressure difference and μ the viscosity of the fluid. When $w \gg h$, the flow profile equation can be simplified to the solution for a fluid flowing between 2 infinite parallel plates.

$$u_x(y, z) = \frac{4h^2\Delta p}{\pi^3\mu L} \sum_{n=1,3,5}^{\infty} \frac{1}{n^3} \left[1 - \frac{\cosh\left(n\pi\frac{y}{h}\right)}{\cosh\left(n\pi\frac{w}{2h}\right)} \right] \sin\left(n\pi\frac{z}{h}\right) \quad \text{Eq. 3.2}$$

To calculate the mean velocity, an approximation of the Poiseuille equation⁸⁹ gives an accurate result shown in equation 3.3 where Q is the flow rate.

$$Q \approx \frac{h^3w\Delta p}{12\mu L} \left[1 - 0.63 \frac{h}{w} \right] \quad \text{Eq. 3.3}$$

Within the same PDMS channel device further thickness variation of the particles as generation time progressed was noticed. Particle generation with a thickness variation $\sim 10\%$ was achieved by exposing the mask shapes in a single location along the microfluidic channel for 0.3 hours. After that, residual crosslinked monomer on the channel bottom wall was observed in the shape of the crosslinked particles which contributed to the reduction of the particles thickness. The second contribution of particle thickness reduction was due to the dynamic interaction between the oxygen inhibition layer and the initiated radical species. The rate of formation of initiating radicals is a function of the incident light intensity and the quantum yield of formation. If radical fragments would remain in the solution or if the monomer or tertiary amine would abstract to the substrate surface, absorbed UV light would diminish, leading to a reduction in photons transmitted to the solution.⁹⁰

To reduce particle variation due to residual monomer buildup on the PDMS microchannel device, the generation location was shifted ~ 0.4 mm towards the collection chamber and this translation was repeated to increase generation session times. Up to 8 hours of particle generation were possible using a single device with a yield $> 150,000$ particles. Higher yields are possible by increasing the array of shapes per mask as well as optimizing the setup and device to minimize t_{stop} . Specialized SFL systems have been developed to increase the rate of particle fabrication by two orders of magnitude.⁵²

Table 3.1: Relevant length and thickness for SFL fabricated particles before and after pyrolysis. Particles were fabricated in a channel 1 mm wide, 3 mm long and $75 \pm 4 \mu\text{m}$ height channel using a 20x and 10x objectives.

		Mask Shape Size	After Generation	In Cleaning Solution	Dried Polymer	Pyrolyzed Ceramic	Linear Shrinkage
Hexagons	Relevant Length (μm)	1205	142 \pm 4	159 \pm 1	121 \pm 1	25 \pm 1	80% \pm 1%
	Thickness (μm)		71 \pm 2	64 \pm 1	52 \pm 2	10 \pm 1	81% \pm 5%
Triangles	Relevant Length (μm)	1040	109 \pm 3	120 \pm 1	93 \pm 1	22 \pm 2	76% \pm 2%
	Thickness (μm)		70 \pm 2	67 \pm 1	52 \pm 1	12 \pm 1	77% \pm 3%
Gears	Relevant Length (μm)	880	205 \pm 4	231 \pm 2	182 \pm 2	35 \pm 1	81% \pm 1%
	Thickness (μm)		72 \pm 2	71 \pm 2	59 \pm 1	12 \pm 1	80% \pm 3%
Note: Microchannel thickness = $75 \pm 4 \mu\text{m}$. 20X objective was used to fabricate the hexagons and triangles and a 10X for the gears.							

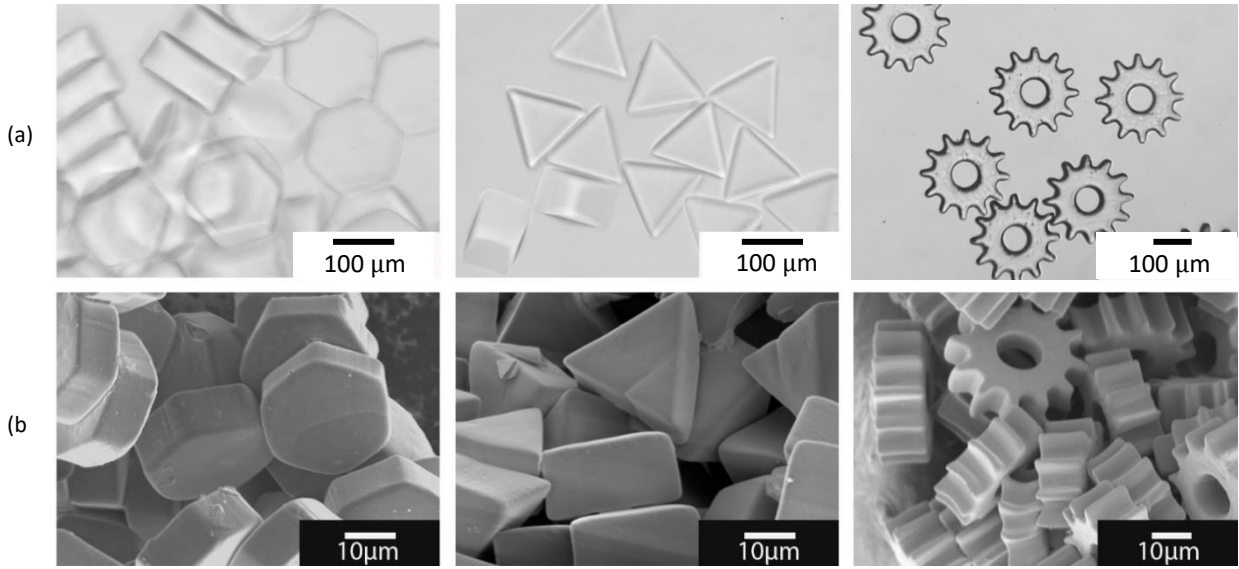


Figure 3.3: Optical (a) and SEM (b) images of hexagons, triangles, and gears particles synthesized via SFL. The upper row shows crosslinked polysiloxane particles in solution after cleaning while the lower row shows the particles after pyrolysis converted to SiOC.

Figure 3.3 shows optical and SEM images of preceramic particles fabricated using SFL with different shapes before and after pyrolysis. The particles relevant length and thickness as well as the linear shrinkage after pyrolysis are summarized in table 3.1. Hexagons, triangles and gears are representative of the preceramic particles that can be fabricated using SFL. Relevant lengths range from 106 to 209 μm while thicknesses ranged from 68 to 74 μm after generation. Particles

show flat side walls with a slight curvature along the edges. Initial particle thickness is given by the channel height minus the oxygen-rich inhibition layer at the top and bottom inner channel surfaces. Previous work have estimated the inhibition layer to be $\sim 2.5 \mu\text{m}$ ⁷⁵ and with a channel thickness of $75 \pm 4 \mu\text{m}$, the particle thickness is expected to be between 66 and 74 μm which matches well with the thicknesses measured after generation. Less variation in the channel thickness can be obtained by using molds from spin coated photoresist and patterns from contact photolithography. Particles swelled when cleaned with IPA and shrank during drying. For example, the hexagons relevant length increased from 142 μm after generation to 159 μm after cleaning and finally shrank to 121 μm after drying. Minimal deformation was observed before pyrolysis suggesting that the particles are strong enough to survive the cleaning and drying processes.

Particle shrank $\sim 80\%$ linearly during pyrolysis as shown in figure 3.3(b) and the values are reported in table 1. The pyrolyzed relevant length ranged from 22 to 38 μm while the thickness ranged from 10 to 12 μm . The alumina crucible was coated about a hundred nanometers with Au-Pd to reduce particle adhesion the crucible surface. Shrinkage is due to the removal of acryl and methyl side groups during pyrolysis as shown in the transmittance vs wavelength curves in figure 3.4(a). C-H(2898 cm^{-1}), O-C=O (1750 cm^{-1}) and CH₃ (1250 cm^{-1} and 600 cm^{-1}) group peaks disappeared after pyrolysis leaving behind wide peaks for the Si-O and Si-C groups as the polymer converted to silicon oxide carbide (SiOC) glass. The non-crystalline structure of the SiOC is confirmed by the broad X-Ray peak shown in figure 3.4(b). Shrinkage is common during pyrolysis of preceramic polymers⁹¹ and different strategies have been developed to minimize it, including changing the polymer structure to increase the number of Si groups and the addition of ceramic particles to the preceramic monomer solution.⁹² In our case, an adhesive polymer optimized for fast crosslinking rather than to maximize ceramic yield was selected to satisfy the SFL requirements, therefore significant shrinkage was obtained. In terms of particle fabrication, shrinkage can be beneficial since it is possible to obtain pyrolyzed particles that are smaller than their crosslinked size. The crosslink particle size is given by the mask shape size and the objective used. The size of the projected mask shape scales linearly with the objective used, a 10x objective gives approximately a $1/4$ reduction in size. In our case the relevant size of the hexagon mask exposed with the 20x objective was 1.2 mm while the projected size was 0.142 mm or approx. $1/8$ size reduction. It is possible to make $< 10 \mu\text{m}$ particles using smaller mask patterns and higher

objective magnifications. For example, a 6 μm relevant length hexagon can be made using a 250 μm hexagon mask shape and a 20x objective.

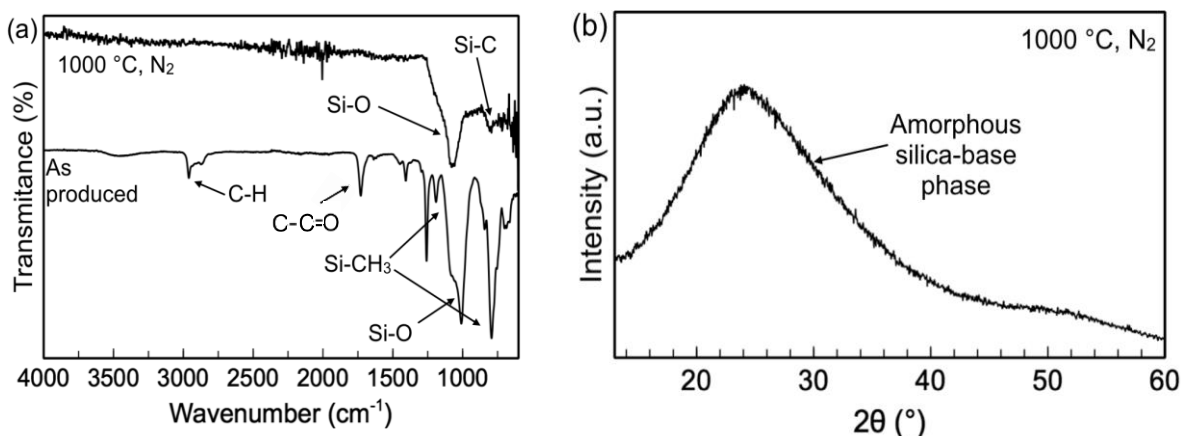


Figure 3.4: (a) Transmittance as a function of wavelength for the preceramic capsules cross-linked in solution and the oxycarbide glass (SiOC) samples after pyrolysis at 1000 °C in nitrogen. (b) X-ray diffraction profile as a function of scanning angle for the oxycarbide glass particles (SiOC) after pyrolysis at 1000 °C in nitrogen.

UV photopolymerization offers several advantages as fast-speed, spatial resolution and ambient temperature fabrication, among others.⁸² As polymer solidifies and transforms from a viscous fluid into a viscoelastic solid, mobility of reactive species decreases.⁹³ For this reason, high intensity and short times exposures are suggested, to achieve higher particle bond conversion rates.⁹⁴ Due to its high degree of acrylic side group modification, linear shrinkage in the dried crosslinkable preceramic polymer to the SiOC ceramic was ~78%, while mass loss ~97%. SiOC true density has been identified as ~2.35 g/cm^3 .⁹⁵

3.4 Conclusions

Ceramic SiOC microparticles in the type of hexagon, triangle and gears, were successfully fabricated via SFL and heat treatment pyrolysis conversion at 1000 °C. SFL offers a route to fabricate hundreds of microparticles per minute in repeatable cycles by using a translucent photosensitive acrylated polysiloxane preceramic polymer. The geometry and definition of the particles were preserved during heat conversion. The pyrolysis of the preceramic polymer led to linear shrinkage ~80%. During heat conversion, methoxide and acrylate side groups of the preceramic precursor were evaporated or chemically transformed. By polymerizing the particles

in a PDMS microchannel, flowability of particles was secured, allowing repeatability of photopolymerization cycles. Microchannel molds constructed with self-adhesive vinyl films demonstrated to be a fair, versatile and economic method to fabricate PDMS microchannel molds besides photolithography technique. The cleaning solution (IPA) proved to be a good solvent to remove the uncrosslinked residual monomer from the photopolymerized particles as long as the particles are not immersed in it more than 1 hour. Alternatives to IPA as the cleaning solution are diphenyl ether and peroxide solutions. SiOC is a hard, biocompatible and chemically inert material that can resist temperatures up to 1200°C. By using an acrylated polysiloxane preceramic precursor to fabricate ceramic SiOC particles, the fabrication of other ceramic microparticles as SiC, Si₃N₄ and SiO₂ through preceramic polymers has been shown to be feasible.

4. FABRICATION OF POROUS HEXAGONAL SIOC MICROPARTICLES VIA STOP-FLOW LITHOGRAPHY

4.1 Introduction

Porous ceramic materials are ubiquitous, ancient, and have plenty of applications. Their properties have been exploited in several fields. For example, in the field of engineering, porous structures have served as physical environments for cell growth¹⁷; micro and mesopores have been suggested as drug delivery carriers;¹⁸ and silicoboron carbonitride foams have been used for CO₂ capturing.⁹⁶ In addition, Fischer et al.⁹⁷ demonstrated the capacity of carbide-derived porous materials to be used as hydrogen storage materials. A further important feature of porosity is its capacity to increase the surface area of a material, which promotes its capability for infiltration and surface modification for self-propelled particles.¹⁹

Preceramic polymer materials offer an important advantage for the fabrication of functional ceramic materials since they can be formed first as moldable liquid polymers before further transformation into ceramics. Introduction of porosity into preceramic materials can be achieved through several routes by introducing sacrificial material that will serve as the pores into the green polymer matrix. Researchers have investigated different approaches to introduce porosity into preceramic polymer materials⁹¹ as sacrificial fillers, etching, direct foaming, aerogel forming, and emulsion forming. Pore sizes with sacrificial fillers can be tuned by selecting different particle dimensions. For example, macroporous alumina ceramics were fabricated by introducing rice husk and sucrose as a binder that burned out when alumina was sintered.⁹⁸ Ceramic foams were achieved by tuning self-blowing time and heat temperature in direct-foaming technique, demonstrating porosity content up to 87%.⁹⁹ Vakifahmetoglu et al.¹⁰⁰ investigated the introduction of pores to preceramic polymers from water in oil emulsions stabilized with surfactants with pore sizes of 100 – 200 μm .

The introduction of porosity by creating an emulsion is an attractive technique, where the pores are the sacrificial discontinuous phase droplets suspended in the continuous phase matrix. By tuning energy density, interfacial tension, and container geometry, emulsion droplet sizes can be lowered to nanometer sizes.¹⁰¹ When droplets sizes reach 40 – 200 nm, the emulsion acquires a translucent or transparent appearance to the human eye.¹⁰² If desired droplet sizes are above 200

nm and a translucent emulsion is aimed to reduce UV-light absorbance of the emulsion, the alternative is to index-match the discontinuous phase with the continuous phase.¹⁰³

Even though the fabrication of porous preceramic polymers via emulsion generation has been proved, the droplet size tunability and porosity amount is still in question. In this research chapter, we demonstrate the introduction of pores in the preceramic polymer through emulsion generation where droplet size of the sacrificial material can be tuned with laminar and turbulent mixing methods, also known as *homogenization*. The emulsion was generated with DI-H₂O in polysiloxane preceramic polymer. The behavior of droplet size with laminar and turbulent homogenization methods is hereby described and analyzed. We present the fabrication of porous preceramic hexagon microparticles using an emulsion via stop-flow lithography (SFL). After heat treatment, the photopolymerized microparticles were transformed into ceramic SiOC microparticles.

4.2 Experimental Section

4.2.1 Materials, Characterization, and Methods

DI-H₂O in polysiloxane emulsion was used to fabricate the hexagon ceramic SiOC microparticles. The preceramic polymer selected was an acrylated polysiloxane with the commercial name TEGO RC® 711 (Evonik®, Dusseldorf, Germany), which was the continuous phase of the preceramic polymer emulsion. For the dispersed phase of the emulsion, DI-H₂O formed droplets in the siloxane matrix that after evaporation and pyrolysis transformed into pores. Water is a good candidate for preparing the emulsion due to its density similarity and immiscibility characteristic with the preceramic polymer selected. Before emulsification, the surfactant Tween 80 (Sigma-Aldrich®, St. Louis, MO) was added at 1 wt% to DI-H₂O to minimize droplet coalescence through time. For the preceramic polymer TEGO RC® 711, photoinitiator Irgacure® 651 (Ciba®, Basel, Switzerland) was added at 2.5 wt% to onset its UV photosensitive capability.

A two-step homogenization process¹⁰⁴ was used to prepare the emulsions. First, the solutions were mixed with a high shear homogenizer (VWR®, Radnor, PA), then with an ultrasonic horn (Branson, Danbury, CT). Emulsions containing water in TEGO RC® 711 at 5 wt%, 10 wt%, 20 wt%, and 30 wt% were prepared following a two-step emulsification process. For the first emulsification, TEGO RC® 711 was mixed with DI-H₂O in a 5-dram vial for a total volume of 3

ml. The high shear blender tip was immersed in the solution and turned on at 6,500 rpm for 5 minutes. After that, the vial with the emulsion stood still for 30 minutes to allow air bubbles to migrate to the top of the emulsion. Then, the emulsion was de-aired in a vacuum chamber by reducing the pressure to 200 mbar and decompressed slowly after 15 minutes. For the secondary emulsification, 2 ml of the primary emulsion was poured into a 1-dram vial, and then the ultrasonic tip was immersed 2 mm and ultrasonicated the emulsion for 2 minutes with 2 seconds on/off pulses with a power amplitude of 32%. The emulsion in the 1-dram vial was also de-aired in the vacuum chamber. Emulsion droplets after the two-step emulsification process were observed with an inverted microscope Axio Observer (Zeiss, Oberkochen, Germany), imaged with a camera (Nikon, Tokyo, Japan), and measured using ImageJ software. The rheology behavior of the emulsion with water content of 5 wt%, 10 wt% and 15 wt% was characterized with the rheometer Bohlin (Malvern Instruments, Malvern, United Kingdom) instrument.

Hexagon microparticles were fabricated via SFL (described in chapter 2) with the prepared preceramic emulsion containing 10 wt% of discontinuous phase. The 1-dram vial with the emulsion was located inside a MitoS® air chamber (Dolomite©, Royston, United Kingdom) and pumped into the $75 \pm 5 \mu\text{m}$ height PDMS microchannel (described in chapter 2). A photomask with 9 hexagon shapes, shown in figure 4.1, was used as the template to project patterned UV light using the inverted microscope through the photosensitive emulsion inside the PDMS microchannel. After the particles polymerized, they were flushed out with an air-pressure pulse letting new unconverted emulsion fill the projection area.

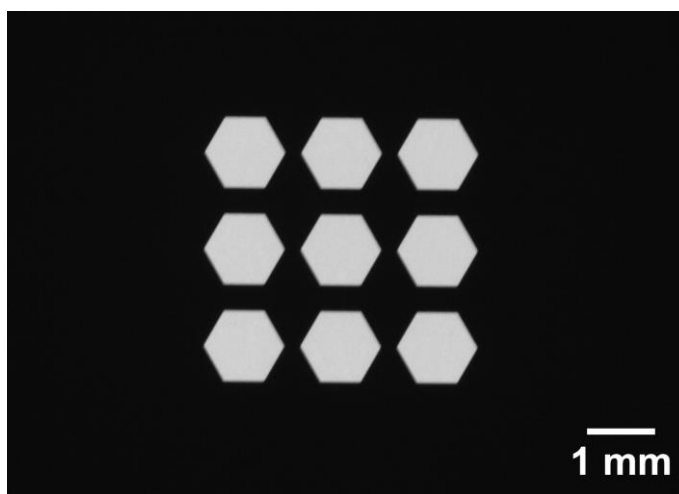


Figure 4.1: Image of photomask used to expose patterned UV light for the photopolymerization of the preceramic polymer emulsion.

The particles were collected, cleaned, and recovered (as described in chapter 4) using isopropyl alcohol (IPA) as the cleaning solution. Particles were dried on a glass slide in a laminar hood for 5 days before proceeding to pyrolysis transformation. The photopolymerized hexagonal extruded shape emulsion microparticles were heated in an oven for 1 hour at 80°C and subsequently for 13 hours at 140°C, to allow water droplets to evaporate from the polymerized green body and leave voids that would serve as the pores. After water removal, the particles were placed on an alumina crucible for pyrolysis treatment, where they were converted into SiOC particles. Polymer to ceramic conversion through pyrolysis heat treatment was performed in an inert atmosphere furnace (Lindberg54352, Lindberg, Riverside, MI) at a temperature of 1000 °C ramping up the furnace at 10 °C/min. Porous hexagonal microparticles were recovered and imaged with SEM Quanta FEG® (FEI, Hillsboro, OR) and measured using ImageJ software. Images of the photopolymerized particles immersed in the cleaning solution can be observed in figure 4.7(a). 70 – 100 measurements were performed to define each particle average size. The error of the measurement was calculated from the standard deviation using a confidence interval of 95%.

4.2.2 Emulsion Generation

We used a two-step homogenization process as the most efficient mechanical mixing method.¹⁰⁴ As a result, we maintained control of droplet sizes. We selected a laminar and turbulent homogenizer as primary and secondary mixing methods to consistently reduce droplet sizes. In both cases, the physics that governs the droplet breakup is the pressure difference between the outer disruptive forces and the inner interfacial forces that defined droplet stability, known as *Laplace pressure*, as show in equation 4.1, where P_L is the Laplace pressure, γ is the interfacial tension, and d is the droplet diameter. The scheme by which both laminar and turbulent emulsification occurs is hereby explained.

$$\Delta P_L = \frac{4\gamma}{d} \quad \text{Eq. 4.1}$$

Laminar Emulsification

Laminar mixing distinguishes three types of flow: rotational, elongational and shear.¹⁰⁵ The mechanism by which an emulsion is generated is droplet break up after droplet deformation. A big droplet is elongated in a shear velocity gradient and, upon disruption, it breaks into smaller droplets. Droplet breakup happens when disruptive forces equal interfacial forces. This process repeats until a minimum size is reached, where the droplets do not elongate anymore but instead rotate.¹⁰⁶

The Capillary number (Ca),¹⁰⁷ shown in equation 4.2, is the ratio of the shear stress to the interfacial stress. It serves as a guide to find when the droplet will burst, if the viscosity of the continuous phase, the interfacial tension, and the shear rate ($\dot{\gamma}$) are known. Grace¹⁰⁷ generated a map of critical Capillary numbers (Ca_{cr}) to guide when the droplet will burst for diverse viscosity ratios for simple shear and 2-D elongation regimes.

$$Ca = \frac{\eta \dot{\gamma} r}{\gamma} \quad \text{Eq. 4.2}$$

During droplet deformation in the shape of a cylinder or shred, flow instabilities as Rayleigh and end-pinch¹⁰⁸ instabilities will cause the droplet to break into two or more droplets. Droplet size as a function of time for laminar simple shear homogenization is then expected to reduce until it reaches its minimum average value after which diameter will plateau out. This behavior has been modeled by Mabille et al.¹⁰⁹ with equation 4.3, where d_m is the minimum droplet diameter, d_0 is the diameter of the initial monodisperse emulsion, d_s is the saturating diameter, ω_0 is the rupture rate, t is the current time, and t_0 is the initial time.

$$d_m(t) = \frac{d_s}{1 - \frac{d_0 - d_s}{d_0} \exp\left(-\frac{\omega_0(t - t_0)}{3}\right)} \quad \text{Eq. 4.3}$$

Even though the droplets minimum size can be predicted for simple general regimes, smaller droplet sizes, known as *satellite droplets*, could also be generated after droplet bursts. The sizes of main droplets and satellite droplets depend on the frequency of the outer instability, geometrical characteristics of the elongated droplet, and physical properties of the emulsion. Efforts to predict the size of both the main droplet and the secondary droplet for liquid jets that micron-size nozzles expel into the air have been studied. Solutions such as the Fisher-Kolmogorov model,¹¹⁰ lubrication approximation¹¹¹ model and the Lattice-Boltzmann¹¹² model have shown reasonable size predictions for primary and satellite droplets due to Rayleigh and end-pinch

instabilities for water in air jet fluids. However, models to predict main droplet with satellite droplet sizes during emulsification are still desired.

Surfactants¹¹³ are commonly used to reduce coalescence and interfacial tension between the continuous phase and the dispersed phase. Below 10 wt% of DI-H₂O content in the acrylated-polysiloxane matrix, the selected surfactant did not show an imperative effect on droplet size and stability during emulsion generation. However, emulsions containing 20 wt% and 30 wt% surfactant showed improved size distribution and reduced coalescence. With 40 wt% percent, the emulsion was of discontinuous type after laminar mixing. After reaching a minimum value with the primary emulsification, droplet sizes were reduced even further by applying a turbulent mixing, where a higher amount of energy was required.

First, the emulsion mixed at a shear rate of 6,500 rpm with a high shear rate mixer in a 5-dram vial that contained 3 ml of both the continuous phase and the discontinuous phase. The plot in figure 4.2 shows droplet content versus droplet size for the same speed but for two different times: 5 minutes, and 20 minutes. This plot suggests that for the case of laminar homogenization, more time is needed to reach droplet minimum diameter when droplet content in the emulsion increases, maintaining constant rotational speed (rpm) and emulsion total volume.

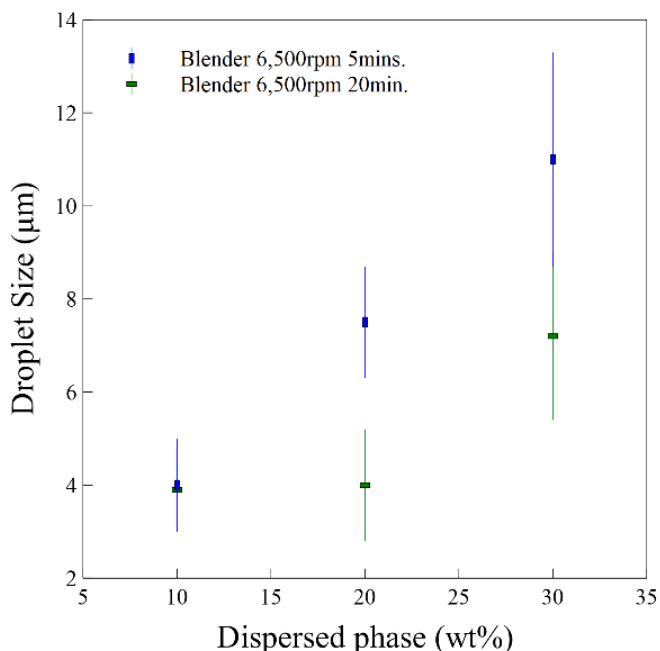


Figure 4.2: Droplet content vs. droplet size for laminar emulsification, considering constant volume and rotational speed for a 5-minute and 20-minute run. The error bar represents the standard deviation measured with a confidence interval of 95%.

Turbulent Emulsification

In turbulent mixing, the droplets do not undergo a shear elongation but rather a cavitation effect. The pressure difference is also the driving force in droplet breakup, where viscous or inertial stresses cause a droplet to break in an emulsion under turbulent flow.¹⁰¹ Ultrasonic horn homogenization is an excellent option to generate turbulent flow and induce cavitation of the droplets. During ultrasonication, physical shear is provided by acoustic cavitation, where formation, growth, and collapse of droplets is caused by pressure fluctuations of the acoustic wave generating highly localized turbulence, known as *implosion*.¹¹⁴ Walstra¹¹⁵ derived equation 4.4 to correlate droplet diameter with power density. To start breaking the droplets with turbulent flow, minimum input power is necessary to generate droplet break-up for a given volume.¹¹⁶ After this threshold, droplet diameter becomes proportional to power density input of introduced acoustic waves. Power density is the energy per time and volume, and it is the main parameter of turbulence strength (P_v , W/ml). The largest diameter, d_{max} , of droplets that can remain in a turbulent field can be calculated with equation 4.4, where C is a geometry constant, P_v is the power density, γ is the interfacial tension, and ρ_c is the density of the continuous phase.¹¹⁵ By lowering the interfacial tension of the phases in the emulsion with the addition of surfactants, droplets sizes as low as 20-30 nm can be generated¹⁰² with ultrasonic homogenization.

$$d_{max} = C P_v^{-2/5} \gamma^{3/5} \rho_c^{-1/5} \quad \text{Eq. 4.4}$$

The secondary emulsification was performed in a 1-dram vial with 2 ml of total emulsion and with an ultrasonic horn to generate turbulent flows. The emulsification time was 3 minutes with 32% power amplitude, with 2 sec. on/off pulses.

Droplet Size Reduction

Droplet size range was reduced and homogenized after following the two-step homogenization process. Figure 4.3 shows droplet size distribution after laminar and turbulent emulsification for the conditions previously described. Figure 4.4(a) shows how droplet size reduce even further after the two-step homogenization process. In figure 4.4(b), droplet size for the case of laminar emulsification, is plotted versus radial speed, and in turbulent homogenization, versus power amplitude. It can be observed in figure 4.4(b), that droplet size for laminar homogenization plateaus after reaching a minimum value, as expected from Mabilie's model. For

the case of turbulent homogenization, droplet size reduces even further following the proportionality $d_{max} \propto P_v^{-2/5}$.

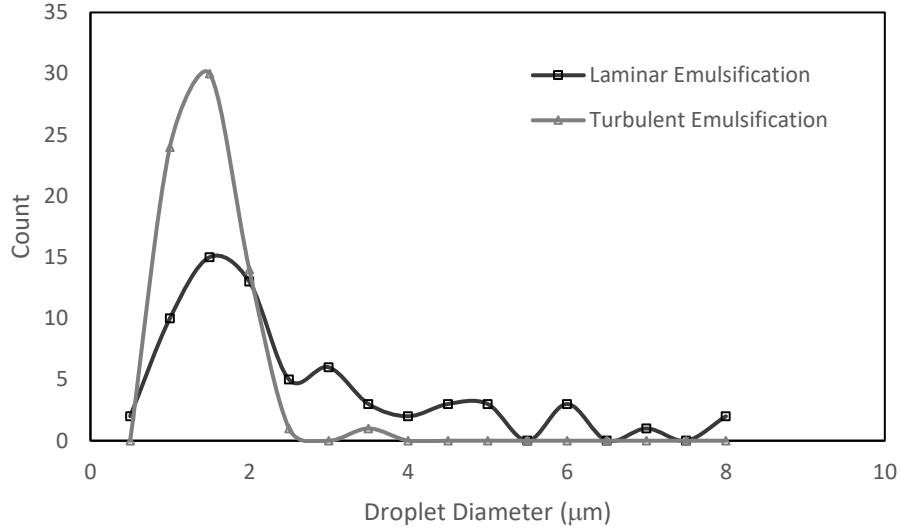


Figure 4.3: Droplet size for laminar and turbulent homogenization, showing the two-step emulsification process. 70–100 droplet sizes were measured, with a bin size of 0.5 μm.

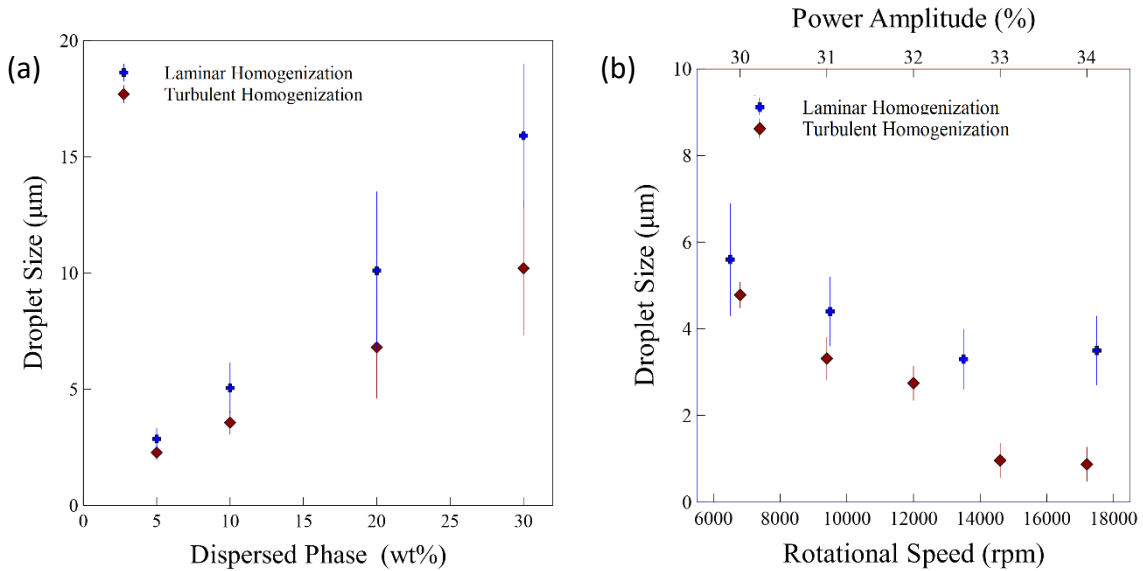


Figure 4.4: Droplet size vs. (a) dispersed phase, and (b) power for laminar and turbulent emulsification processes. Total volume was maintained constant with a droplet content of 10 wt%. For the case of laminar homogenization, x-axis is rotational speed. For turbulent homogenization, x-axis is power amplitude. The error bar represents the standard deviation measured with a confidence interval of 95%.

Rheology Behavior

Rheology models have shown to help predict emulsion and suspension flow through a duct or microchannel with diverse assumptions since several variables play a role in their behavior. Yaron and Gar-Ofi suggested a power law with correction factors to consider droplet deformation in emulsion rheological behavior.¹¹⁷ The rheology behavior of this emulsion was characterized with the rheometer Bohlin (Malvern Instruments, Malvern, United Kingdom) instrument, for water content of 5 wt%, 10 wt% and 15 wt%. Figure 4.5 shows how the viscosity behaves for an increasing content of discontinuous phase, for shear rates of 10-1000 s⁻¹.

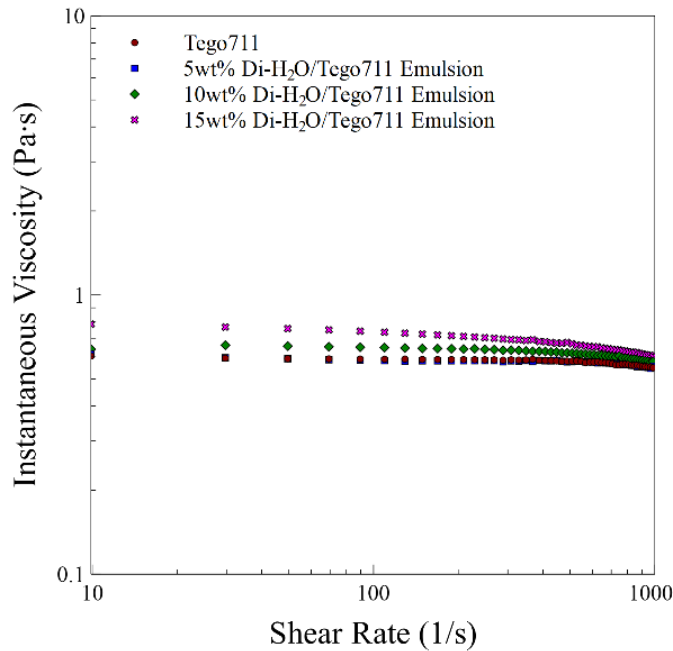


Figure 4.5: Rheology behavior of DI-H₂O/TEGO RC® 711 emulsion with DI-H₂O content of 5, 10 and 15 wt%.

4.2.3 Hexagon Microparticle Fabrication

Hexagon microparticles were fabricated using SFL method, as described in chapter 2. The prepared photosensitive acrylated-polysiloxane/DI-H₂O emulsion contained 10 wt% of DI-H₂O. It was flown into a PDMS microchannel and exposed with patterned UV light pulses to onset polymerization of the particles. The cycle repeated every 2.4 seconds for a yield of 13,500 particles/hour. Table 4.1 shows the parameters used to polymerize the hexagons particles using SFL.

Table 4.1: Stop-Flow lithography fabrication parameters as objective used, number of exposed shapes, exposed particle size, flush out and cycle times.

Size reduction	25%	SFL cycle time	2.36 s
Objective	10x	Exposure time	70 ms
UV light intensity level	4	Dark polymerization time	100 ms
Exposed particle size	275 μ m	Flush out time	700 ms
Flush out pressure	500 mbar	Stop time	1500 ms

After fabrication, particles were collected, drained, washed, and dried before heat treatment processes. The water droplets from the microparticles were evaporated by placing the particles in an oven for 1 hour at 80 °C and subsequently for 13 hours at 140 °C to generate the pores. Then, hexagon microparticles were pyrolyzed in an argon atmosphere furnace at 1000 °C. After fabrication, microparticle and pore dimensions were measured and compared, both, in cleaning solution and after pyrolysis. Linear shrinkage in the order 74% was measured for the hexagon microparticles from vertex to vertex. For the pore sizes, the linear shrinkage measured was 50%. Pore distribution on both sides of the microparticles was dissimilar. Pores on one side of the surface covered $\sim 11\%$ of the area and just $\sim 1\%$ of the surface area of the other side. This effect can be explained from the droplet migration to the microchannel centerline due to the lift force towards the microchannel centerline that the droplets experience during emulsion flow. As a result, the surface area of both sides of the droplets viewed two different values of surface area increment.

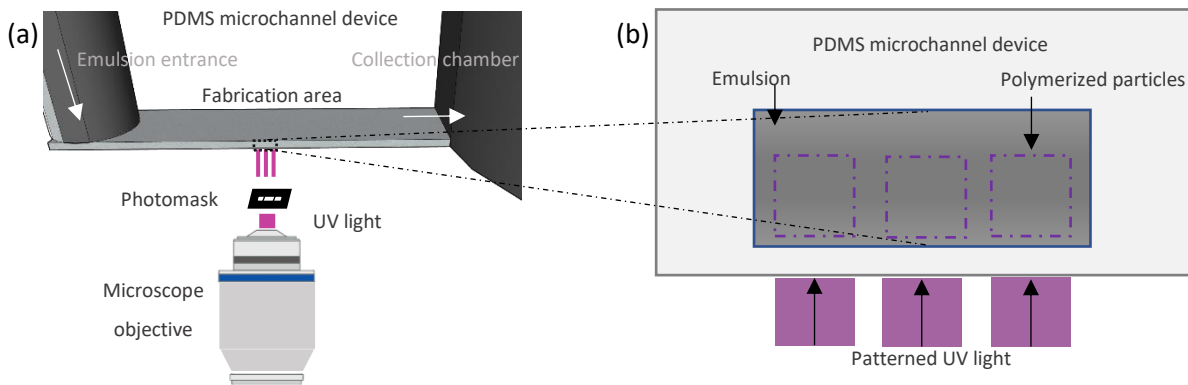


Figure 4.6: Schematic showing (a) PDMS microchannel device with emulsion entrance, fabrication area and collection chamber region; patterned UV light is projected to the fabrication area where the emulsion polymerizes in SFL cycles. (b) Schematic showing side view of microchannel particle fabrication area, showing the emulsion and partial height polymerization of the microparticles. The schematics are used for description, they are not actual scales.

Table 4.2: Hexagon microparticles, droplets and pores relevant dimensions after fabrication, immersed in cleaning solution, and after pyrolysis.

Hexagon Microparticles

(μm)	After fabrication	In cleaning solution	After pyrolysis
Diameter	248 ± 7.5	269.5 ± 16	65.5 ± 5
Thickness	59.5 ± 3	59 ± 4.5	10.5 ± 1

Droplets and Pores

(μm)	After emulsification	In cleaning solution	After pyrolysis
Diameter	2 ± 1	2.5 ± 1.5	1 ± 0.5

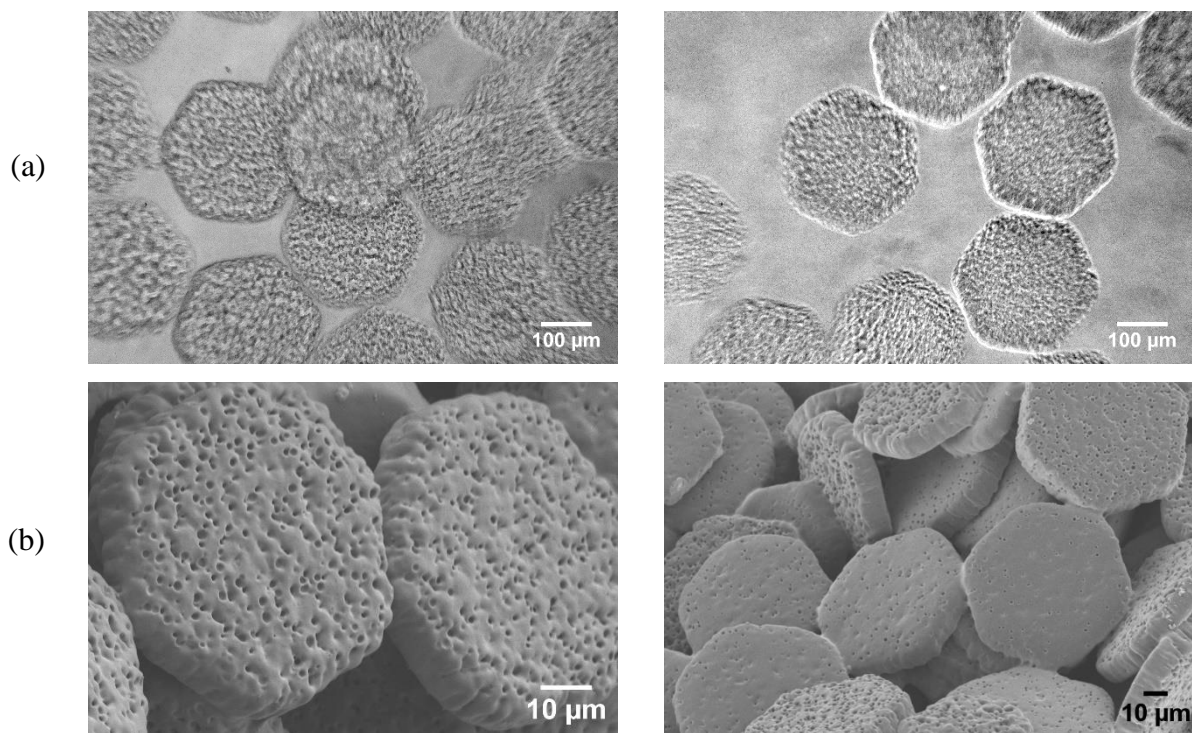


Figure 4.7: (a) Optical images of polymerized acrylated polysiloxane/DI-H₂O emulsion hexagon microparticles in cleaning solution. (b) SEM images of the ceramic hexagon microparticles after completion of polymer to ceramic transformation.

In an experiment fabricating microparticles in a reduced area microchannel with a low concentration dispersed phase emulsion, droplets were observed to migrate away from the PDMS microchannel walls, which corroborated the observation of higher porosity on one side of the microparticle and less on the opposite side (figure 4.8). On the other hand, inhibition of the UV light transmittance led to particles not polymerizing through all microchannel height. Considering these two effects, it can be understood that particles started polymerization at the bottom of the microchannel where a lower concentration of droplets was found and stopped polymerization between the centerline and the microchannel top wall, where a higher concentration of droplets was found.

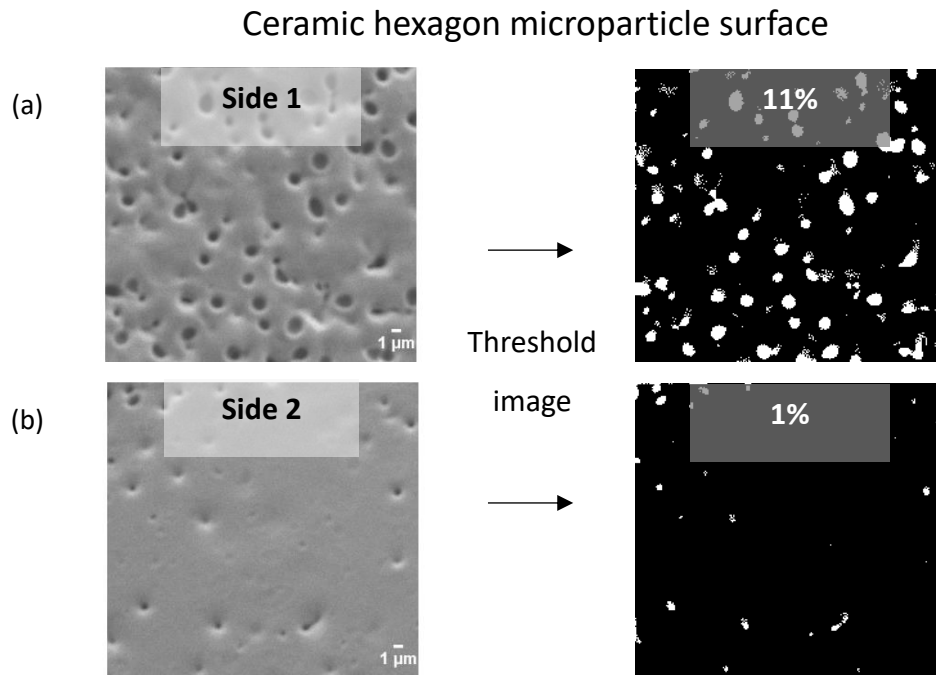


Figure 4.8: (a) Image showing one side of a ceramic microparticle with a higher content of porosity, after converting the image to black and white with the threshold method, the area with pores was measured at 11%. (b) Side two showed a low content of porosity, after doing the conversion of the image to black and white with the threshold method, the porous are was measured at 1%.

Droplet Migration

The first factor leading to different content of pores on both sides of the microparticles was droplet migration. Droplets and particles suspended in a continuous liquid matrix have shown migration of position during flow movement through a tube or a microchannel. Shear-induced force arises from the curvature of the flow profile in a microchannel.¹¹⁸ Segre and Silberger¹¹⁹ were the first to report particle migration in a circular tube. Particles, drops or cells that flow

through a channel move to a specific position depending on their properties.¹²⁰ Even at a low Reynolds number, drag and lift forces may change particles positions. If the migration rate is controlled, gradient porosity can be induced for UV exposed particles by controlling the shear velocity of a suspension or emulsion.¹²¹ Asmolov¹²² derived an expression (equation 4.5) for the net lift lateral force acting on a single spherical particle in a flow, where F_L is known as the lift force, ρ is the density of the fluid, U_f is the velocity of the fluid, C_L is the lift coefficient, a_p is the diameter of the particle and w is the microchannel width. Asmolov¹²² also stated that for a single particle the distance to completely migrate to an equilibrium position was given by equation 4.6, where η is the viscosity of the fluid and L_p is the maximum required migration distance.

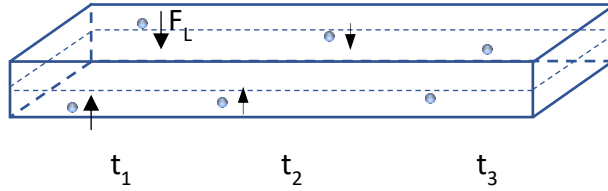


Figure 4.9: Schematic showing a PDMS microchannel where an emulsion is flow. Droplets experience migration due to a lift force (F_L) towards the centerline of the microchannel. t_1 , t_2 and t_3 , represent increasing times when the particle will change position.

$$F_L = \frac{4\rho U_f^2 C_L a_p^4}{w^2} \quad \text{Eq. 4.5}$$

$$L = \frac{3\pi\eta w^2 L_p}{2\rho U_f a_p^3 C_L} \quad \text{Eq. 4.6}$$

However, droplets have a more complicated behavior since deformation and internal circulation need to be taken into account.¹¹⁸ It has been shown by Lan,¹²⁰ that even when a droplet does not elongate as a shred, it will still deform as a triangle shape with curved endpoints. Chen modified the approach for the case of simple shear flow of lift force acting on sphere-like droplet where deformation was taken into account.¹¹⁸ Multiple droplets have more complicated behavior since an additional droplet-droplet interaction will be expected. However, for initial studies, droplets can be modeled as hard spheres before accounting for their deformability. For droplets behaving as a hard-sphere, Stokesian dynamics, diffusive flux models, suspension balance models, and two-fluid models¹²³ have truthfully simulated the behavior of particle migration in a suspension. Using Stokesian dynamics, for a suspension flow of hard spheres, Nott and Brady¹²⁴

derived equation 4.7, for the length necessary for particles to migrate to the equilibrium position, where L is the channel length, H is the channel height, and $f(\phi_b)$ is the shear induced diffusion function.

$$\frac{L}{H} \geq \frac{1}{6g(\phi_b)} \left(\frac{H}{d_p} \right)^2 \quad \text{Eq. 4.7}$$

Thickness Dependence

The second factor leading to different content of pores on both sides of the microparticles was UV light absorbance of the emulsion. UV light gets transmitted, absorbed, or reflected on a material. From Beer-Lambert law¹²⁵ we know that as concentration increases in an emulsion or suspension, absorbance of that material increases as well. It was observed experimentally that the thickness of the polymerized particles exposed with UV-light in the PDMS microchannel had a thickness reduction as the discontinuous phase droplets concentration increased. If thickness reduction is to be avoided, there are two main approaches. The first approach is to reduce the droplet sizes to $\leq 200\text{nm}$,¹¹⁴ where the emulsion becomes translucent, and the second is to index match the discontinuous phase with the continuous phase to obtain a translucent or transparent emulsion without constraint on the droplet size.

Table 4.3: Glycerol and DI-H₂O contents of emulsion discontinuous phase to index match with preceramic continuous phase TEGO RC ® 711 refractive index.

Glycerol	DI-H₂O	Refractive Index	Appearance
83wt%	17wt%	1.459	Opaque
77wt%	23wt%	1.438	Semi translucent
71wt%	29wt%	1.429	Translucent
67wt%	33wt%	1.423	Semi translucent
63wt%	38wt%	1.417	Opaque

The discontinuous emulsion phase was modified to index match the continuous phase. Glycerol was added to DI-H₂O and then to TEGO RC® 711 to index match both phases. Glycerol has a refractive index of 1.4731, and DI-H₂O of 1.333. The matched refractive index was 1.429 for a translucent emulsion. The selected weight percentages for the droplets discontinuous phase were 71 wt% glycerol and 29 wt% of DI-H₂O. Table 4.3 shows the percentages of glycerol and

water mixed together, and the appearance of the emulsion after primary mixing with the continuous phase TEGO RC® 711 polysiloxane. The mixing ratios were performed by following the EDGE glycerol/DI-H₂O refractive index guide¹²⁶ from the Rochester Institute of Technology. By mixing the right concentration of water in glycerol, the emulsion produced in TEGO RC® 711 can be index matched to allow UV-light to polymerize the particles throughout the microchannel. After addition, glycerol and DI-H₂O mixed in the wheel for 12 hours. In figure 4.10, we can observe the thickness reduction as a function of discontinuous phase concentration, for the case of DI-H₂O and 71 wt% glycerol/29 wt% DI-H₂O as the discontinuous phase.

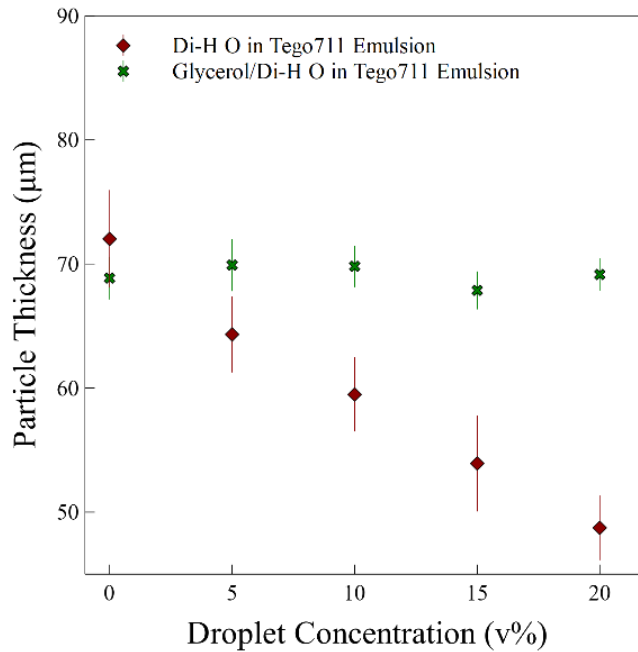


Figure 4.10: Microparticles thickness as a function of droplet concentration for the case of DI-H₂O and 71 wt% glycerol/29 wt% DI-H₂O as the dispersed phase in the preceramic polymer TEGO RC ® 711. The error bar represents the standard deviation measured with a confidence interval of 95%.

4.3 Conclusions

Porosity can be introduced in a preceramic polymer material by initially generating a photosensitive emulsion. Pores are introduced by creating sacrificial droplets, and their size can be defined by controlling the energy input when the continuous and discontinuous phase of an emulsion are mixed. Droplet breakup arises from pressure difference between the droplet and their surroundings. With a two-step homogenization method, laminar and turbulent, droplet sizes reduces with a narrow size distribution.

During laminar homogenization, droplets with smaller diameters may be generated, also known as satellite droplets. After reaching a minimum average drop size with laminar emulsification, droplets may continue to lower their size with a turbulent emulsification, proportional to the power law $e^{(2/5)}$. Alternatively, if the interfacial tension is reduced, droplets with even smaller sizes can appear with these mixing methods. Porous content through emulsion generation was introduced up to 30%. With 40% of dispersed phase, the emulsion did not mix homogeneously, and generated areas of great coalescence. Hexagon SiOC preceramic microparticles containing 10% of porosity were fabricated via SFL with cycle times of 2.4 seconds and a yield of 13,500 particles/hour. With 20% and 30% of dispersed phase, interconnected structures can be obtained, however, a surfactant with better long-term stability is required to reduce droplet coalescence.

Pores showed a linear shrinkage of 50%, while particles showed 74% percent. The surface area of the droplets showed dissimilar porosity. Pores on one side covered 11% of the particle area; while on the other side just covered 1%. This meant an increment in their surface area. The difference in porosity content was due to droplet migration during emulsion flow in the microchannel. If inlet pressure and the microchannel length are predefined, porous microparticles may achieve a gradient porosity. Exposed UV light to polymerize the microparticles was absorbed by the emulsion affecting the total height of the microparticles. To avoid thickness reduction, droplet sizes should be ≤ 200 nm or an index-match emulsion should be used.

5. FABRICATION OF SIOC MICROPARTICLES WITH EMBEDDED COBALT ZINC FERRITE NANOPARTICLES VIA STOP-FLOW LITHOGRAPHY

5.1 Introduction

Microparticles with controlled mobility capability are of special interest to the fields of structured assembly,²⁰ wastewater treatment,¹²⁷ magneto-optical devices,¹²⁸ microrobotics,²¹ and drug targeting.¹⁶ Drug delivery is a field with a strong need to control particle directionality. Magnetic particles have been tested to act as drug carriers for localized controlled-dose delivery. With external magnetic fields, magnetic microparticles can serve as non-intrusive medical devices alternatives to surgeries.²² Cancer, aids, and brain diseases can benefit from reducing both, risk and cost of intervention. Research on chemotherapies has deployed magnetic drug carriers,²³ in which a cytotoxic drug attached to a magnetic particle travels through the patient circulatory system towards areas of concentrated tumor cells.

For drug delivery purposes, paramagnetic and ferro/ferrimagnetic behavior are of the highest interest because of their higher susceptibility to external magnetic fields. Paramagnetic particles have an interesting behavior because their dipole orientation appears only when an external field is applied and acts individually with no mutual interaction between adjacent dipoles.¹²⁹ Ferro/ferrimagnetic materials are also very attractive but have an important disadvantage: their remnant magnetization is typically high, which may lead to particle agglomeration. Ferro/ferrimagnetic materials possess a permanent magnetic moment that increases when an external field is applied, but when the external field is released, they keep a magnetization magnitude.

Ferrimagnetism is a phenomenon found in cubic ferrite ceramics materials with the chemical formula MFe_2O_4 , where M is a metal element like Al, Co, Ni, Mn, and Zn.¹³⁰ Ferrites are an abundant and economic source of magnetic materials. They can have a dipole formula MFe_2O_4 or tripole formula $MNFe_2O_4$ with the known crystal structure spinel ferrite.¹³⁰ By adding lanthanides or transition metals, the crystal structure can modify its lattice parameters and properties. For example, by co-doping the ferrite structure with cobalt or nickel in addition to zinc, the doped ferrimagnetic material will lower its remnant magnetization and increase its saturation magnetization.¹³¹ When tuning the concentration of ions for the spinel ferrite $Co_xZn_{(1-x)}Fe_2O_4$, its

morphological, structural, elastic, optical, and magnetic characteristics will be modified.¹³² $\text{Ni}_x\text{Zn}_{(1-x)}\text{Fe}_2\text{O}_4$ is another interesting material with attractive properties, showing an even lower remnant magnetization with higher susceptibility than $\text{Co}_x\text{Zn}_{(1-x)}\text{Fe}_2\text{O}_4$.¹³³ Zinc results in an interesting element, because it can lead to a paramagnetic transition when adding it to a ferrite.¹³⁴ Additionally, ferro/ferrimagnetic particles are of high interest due to its highest magnetic susceptibility, low cost, versatility, and stability.¹³⁵

Hydrogel microparticles with embedded paramagnetic nanoparticles have been previously fabricated via stop-flow lithography (SFL).¹³⁶ However, magnetic nanoparticles with higher susceptibility are desirable to control particle mobility and reduce necessary external field strength. In this research chapter, we present the fabrication of oval microparticles via SFL containing $\text{CoZnFe}_4\text{O}_8$ magnetic nanoparticles embedded in the green preceramic polymer siloxane matrix with a ferrimagnetic behavior. The transformation of the microparticles from polymer to ceramic with the embedded ferrimagnetic nanoparticles is hereby demonstrated.

5.2 Experimental Section

5.2.1 Materials, Characterization, and Methods

The preceramic polymer used in this research was TEGO RC® 711. The photoinitiator selected, Irgacure 651 (Sigma-Aldrich®, St. Louis, MO) with chemical composition 2,2-Dimethoxy-2-phenylacetophenone, was mixed with the preceramic polymer to improve its UV curing properties. $\text{CoZnFe}_4\text{O}_8$ (Nanostructured and Amorphous Materials Inc., Katy, TX) ferrimagnetic nanoparticles were added and homogenized to the preceramic polymer. The magnetic nanoparticles have a purity of 99.5% with theoretical sizes ranging from 30–50 nm, and magnetic properties as saturation magnetization of $M_s = 27.5$ emu/g, remnant magnetization of $M_r = 5.7$ emu/g, and coercitivity of 286 Oe. Figure 5.1 shows an image of the size and morphology of the $\text{CoZnFe}_4\text{O}_8$ magnetic nanoparticles. We can observe from the image that the particles are in aggregate form and are not found as separate particles. The magnetic nanoparticles, $\text{CoZnFe}_4\text{O}_8$, in water were ultrasonicated and size was measured with the dynamic light scattered instrument Nano ZS (Malvern Instruments, Malvern, United Kingdom) to analyze crystal size.

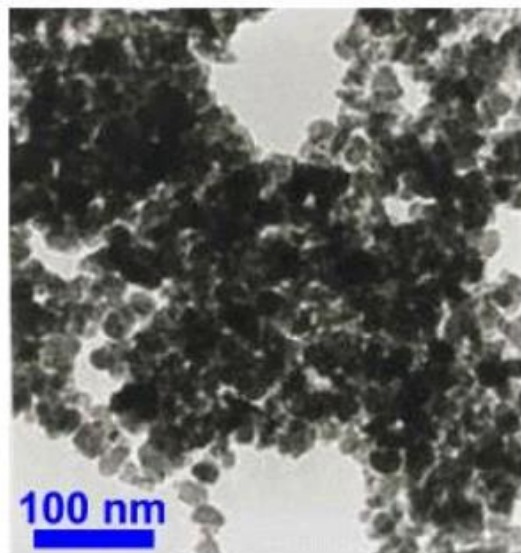


Figure 5.1: TEM image of magnetic nanoparticles $\text{Co}_{0.5}\text{Zn}_{0.5}\text{Fe}_2\text{O}_4$ provided by Nanostructured and Amorphous materials, Inc.

The photoinitiator was added to the preceramic polymer at 2.5 wt% and mixed on a rotational mixing wheel for 12 hours. Four TEGO 711® RC suspensions were prepared in vials containing magnetic $\text{CoZnFe}_4\text{O}_8$ nanoparticles at 0.0015 wt%, 0.015 wt%, .05 wt%, and .1 wt% concentrations. The preceramic polymer was then added to the vial that contained the magnetic nanoparticles to complete a total volume of 2 ml. Each vial was placed in an ultrasonic horn (Branson, Danbury, CT) and mixed in a turbulent flow with 2 sec. on/off pulses for 2 minutes at 20% power intensity amplitude. The procedure was repeated two times. For the first iteration, the ultrasonic tip was near the bottom of the vial at approximately 20% of the solution height. For the second iteration, the ultrasonic tip was near the top of the solution, at approximately 80% of the solution height, as observed in figure 5.2. After the preparation of the magnetic suspensions in 1-dram vials, agglomerates (estimated diameter $> 2 \mu\text{m}$) sedimented after the vial was left unperturbed for 14 days. The supernatant of the suspensions was then recovered and transferred to a new vial for further use. A UV-Vis transmittance experiment was performed with the instrument Lambda950 (PerkinElmer, Waltham, MA) to measure UV absorbance of the magnetic particles at wavelengths between 300 and 380 nm in polymethylmethacrylate (PMMA) cuvettes of 1-cm thickness. The transmittance of the suspensions was measured using the UV-Vis spectrometer thirty minutes after the suspension was prepared.

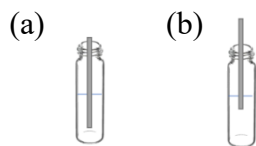


Figure 5.2: Illustration of ultrasonic tip immersed in vial (a) close to the bottom and (b) close to the top of the solution, containing preceramic polymer and magnetic nanoparticles.

Polymer particles containing $\text{CoZnFe}_4\text{O}_8$ magnetic nanoparticles were fabricated via SFL, as described in Chapter 2. After 30 minutes of fabrication, particles were collected in a mesh to drain the excess uncrosslinked solution for 12 hours. Afterward, particles were cleaned with isopropyl alcohol (IPA) using the exchange solvent method described in chapter 2 and dried 1 week before further transformation. Dried magnetic ovals were transferred to an alumina crucible for pyrolysis heat treatment and conversion to ceramic microparticles in an inert atmosphere furnace (Lindberg54352, Lindberg, Riverside, MI). Subsequently, particles were recovered for imaging using SEM (Quanta FEG, Thermofisher, Hillsboro, OR) and ImageJ software.

5.3 Results and Discussion

Magnetic behavior of a material depends on the external magnetic field applied and its intrinsic properties. The magnetic field strength is generally defined with the H symbol having units of oesterd (Oe). A higher susceptibility (χ) leads to a material with higher saturation magnetization. For the application of magnetic particles as drug delivery carriers, magnetic saturation should be maximized, while remnant magnetization should be minimized.

In $\text{CoZnFe}_4\text{O}_8$, a higher concentration of cation Co^{2+} may lead to an increase in the saturation magnetization from 5.7 up to 82 emu/g.¹³² Saturation magnetization changes due to the occupancies of cations and an increase disorder of the spinel structure.¹³⁰ Remnant magnetization (M_r) and coercitivity (H_c) are also affected by an increase of Co^{2+} content. These property changes are related to the crystalline structure modification of the material.¹³²

Pyrolysis heat treatment was performed at 600°C to allow full polymer to ceramic conversion and avoid zinc evaporation. During pyrolysis and mass loss of the preceramic polymer, a densification of the material was expected; as a result, an increase in the content of magnetic nanoparticles occurred. Due to high dipole-dipole magnetic interactions, ferrite nanoparticles suffer from strong aggregation.¹³⁷ Efforts such as coatings, surfactants, and additives to reduce

this effect are being studied.¹³⁸ In the meantime, the separation of big aggregates, small aggregates, and individual crystals can be achieved by diverse separation methods.¹³⁹

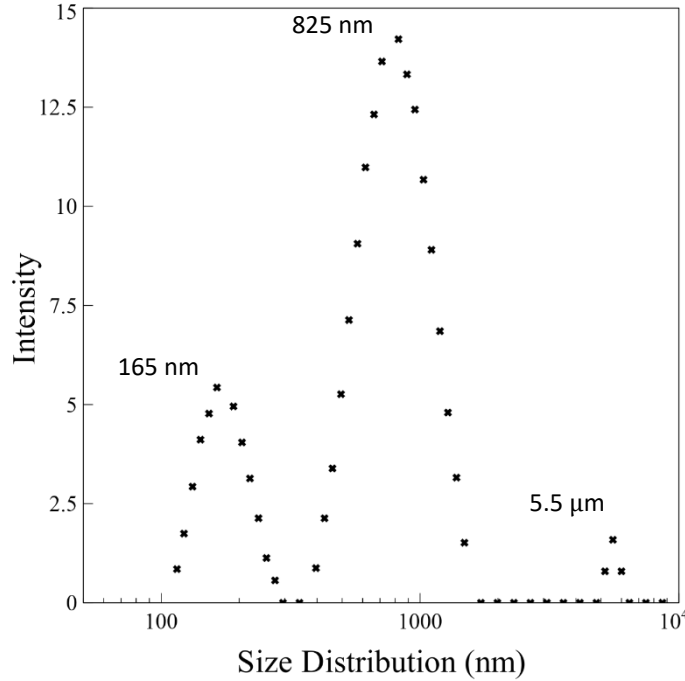


Figure 5.3: Size distribution plot for agglomerated $\text{Co}_{0.5}\text{Zn}_{0.5}\text{Fe}_2\text{O}_4$ nanoparticles immersed in DI- H_2O after ultrasonic mixing in a 1-dram vial with 20% of power amplitude.

Nanoparticle agglomerates $> 2 \mu\text{m}$ were separated from the suspension using a regular sedimentation method. The three main peaks observe in the size distribution plot of figure 5.3 were at 165 nm, at 820 nm, and at $5.5 \mu\text{m}$. Using the stokes sedimentation formula, as seen in equation 5.1, we can estimate the time for a particle to sediment a certain height in a liquid media, where t is time, h is height, η is viscosity, g is gravity, ρ is density, and d is particle diameter. $\text{CoZnFe}_4\text{O}_8$ particles have a density of 5.2 gr/cm^3 , and a height of 2.5 cm was considered.

$$t = \frac{h(18\eta)}{g(\rho_1 - \rho_2)d^2} \quad \text{Eq. 5.1}$$

If particle size separation wants to be accelerated, methods such as magnetic sedimentation¹³⁹ or centrifugation¹⁴⁰ can be implemented. By spinning a vial around a central axis, a particle suspension will experience radial force away from it,¹⁴¹ which will pull particles towards the bottom of the centrifuged vial. By increasing the G force, known as RCF , particles sizes are

expected to separate faster as the magnitude of the gravitational field increases, following the formula in equation 5.2, where l is the radius of the vial to the center of the centrifuge. It can be noted that the RCF is exponential to the radial speed in rpms. Table 5.1 shows the hours needed for particle size separation using both sedimentation and centrifugation with 10,000 rpm.

$$RCF = 11.18 \cdot l \left(\frac{rpm}{1000} \right)^2 \quad \text{Eq. 5.2}$$

Table 5.1: Sedimentation and centrifugation time to separate particle agglomerates of 0.4 – 10 μ m in TEGO RC® 711 preceramic polymer matrix.

Diameter	Sedimentation	Centrifugation
(μm)	(Hours)	(10,000rpm)
0.4	1.10E+04	1.10E+00
1	1.80E+03	1.80E-01
2	4.50E+02	4.50E-02
4	1.10E+02	1.10E-02
10	1.80E+01	1.80E-03

5.3.1 Preparation

Incremental content of magnetic nanoparticles in the preceramic polymer will have an effect on the thickness of the UV exposed microparticles. The extinction coefficient of the magnetic nanoparticles inhibits radical formation from the photoinitiator, limiting polymerization through all microchannel height. For a microchannel thickness of $75 \pm 5\mu$ m, with content above 1 wt% of magnetic nanoparticles, it was observed that UV-exposed microparticles reduced its thickness. Below 0.5 wt%, the UV exposed microparticles thickness did not have a significant reduction.

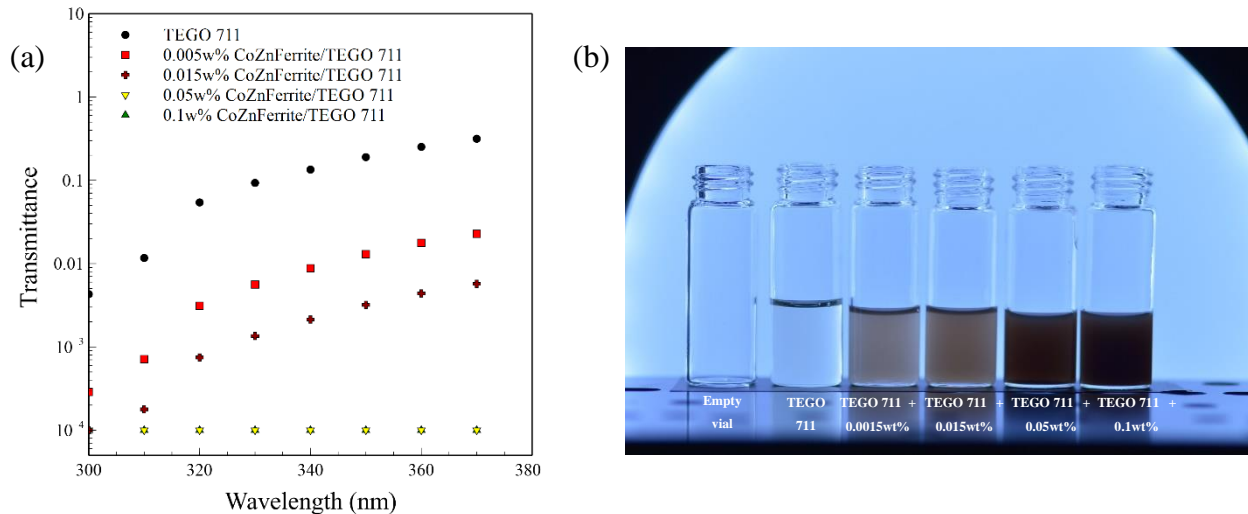


Figure 5.4: (a) Suspension transmittance vs. UV-light wavelength for TEGO RC® 711 containing CoZnFe₄O₈. b) Picture of suspensions after ultrasonic mixing for vials containing TEGO RC® 711 and magnetic particles with concentrations of 0.005 wt%, 0.015 wt%, 0.05 wt%, and 0.1 wt%.

To minimize thickness reduction due to inhibition of UV light, magnetic nanoparticles were added at concentrations $\leq 1\text{wt}\%$. To study the extinction coefficient of magnetic nanoparticles, four vials containing 0.005 wt%, 0.015 wt%, 0.05 wt%, and 0.1 wt% of nanoparticles in TEGO RC® 711 were mixed with the ultrasonic horn using the method previously described. For particle sizes below the visible light wavelength, the suspension becomes translucent, which minimizes UV light absorbance. We can observe from figure 5.4(a) that as magnetic nanoparticle content increases, UV light transmittance decreases.

5.3.2 Oval Shape Microparticle Fabrication

Particle agglomerates $> 2\mu\text{m}$ can be separated from the prepared photoinitiated suspension either by sedimentation or centrifugation. Two vials were used for the fabrication of the oval microparticles, which had an initial concentration of 1 wt% and 0.5 wt% of magnetic nanoparticles before sedimentation. After sedimentation, the content of magnetic nanoparticles was estimated in 0.1 wt% and .05 wt%, comparing the appearance of the sedimented suspensions with the suspensions used for UV transmittance test and the EDX test results. The suspension was fed into a PDMS microchannel for the continuous pulse polymerization of the microparticle suspension. Oval ceramic magnetic microparticles were fabricated successfully via SFL by feeding the

suspension into the microchannel. The particles were collected, washed, and dried after fabrication. The mask used for the fabrication of the particles is shown in figure 5.5, and the parameters used for the SFL fabrication can be found in Table 5.2.

Table 5.2: Stop-flow lithography parameters used for the fabrication of oval microparticles containing $\text{Co}_{0.5}\text{Zn}_{0.5}\text{Fe}_2\text{O}_4$ nanoparticles.

Objective	20x	SFL cycle	1.64 s
Reduced size	12.5%	Exposure time	40 ms
UV light intensity level	4	Dark polymerization time	150 ms
Exposed particle size	187 x 63 μm	Flush out time	650 ms
Flush out pressure	500 mbar	Stop time	800 ms

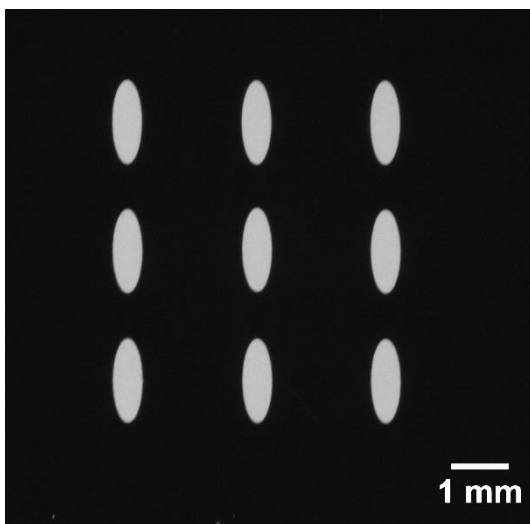


Figure 5.5: Photograph of a photomask used for the fabrication of oval microparticles with a 3x3 array via SFL.

The average initial dimensions of the oval particles of vial 1 (0.1wt%) were 162 μm x 65 μm x 62 μm , while the final average dimensions after pyrolysis were 39 μm x 15 μm x 13 μm . The linear shrinkage was in the order of 76% with a mass loss of $\sim 96\%$. A table showing the dimensions of the oval particles for both vials through the fabrication process can be found in table 5.4. Because of methacrylate and silanol chemical transformation and evaporation due to polymer to ceramic conversion, the initial wt % of the preceramic polymer matrix reduced drastically. From

the linear shrinkage and mass loss calculated, the initial and final concentration of magnetic nanoparticles embedded in the ceramic matrix expected from the initial loading is presented in table 5.3. Oval polymer and ceramic microparticles can be observed in figure 5.6.

Table 5.3: Content of magnetic nanoparticles embedded in the oval microparticles before and after pyrolysis.

Initial wt%	Final wt%
1	35
0.1	5
0.05	2.5
0.015	0.8
0.005	0.26

Table 5.4: Particle dimensions of oval microparticles after fabrication, in cleaning solution and after pyrolysis.

Oval Particles Dimensions (μm) Vial 1			
	After Fabrication	In Cleaning Solution	After Pyrolysis
Length	162 \pm 6	181 \pm 6	39 \pm 2
Width	65 \pm 1	66 \pm 2	15 \pm 1
Thickness	62 \pm 2	61 \pm 2	13 \pm 1

Oval Particles Dimensions (μm) Vial 2			
	After Fabrication	In Cleaning Solution	After Pyrolysis
Length	161 \pm 4	187 \pm 2	54 \pm 2
Width	64 \pm 2	73 \pm 2	23 \pm 1
Thickness	61 \pm 1	66 \pm 2	17 \pm 1

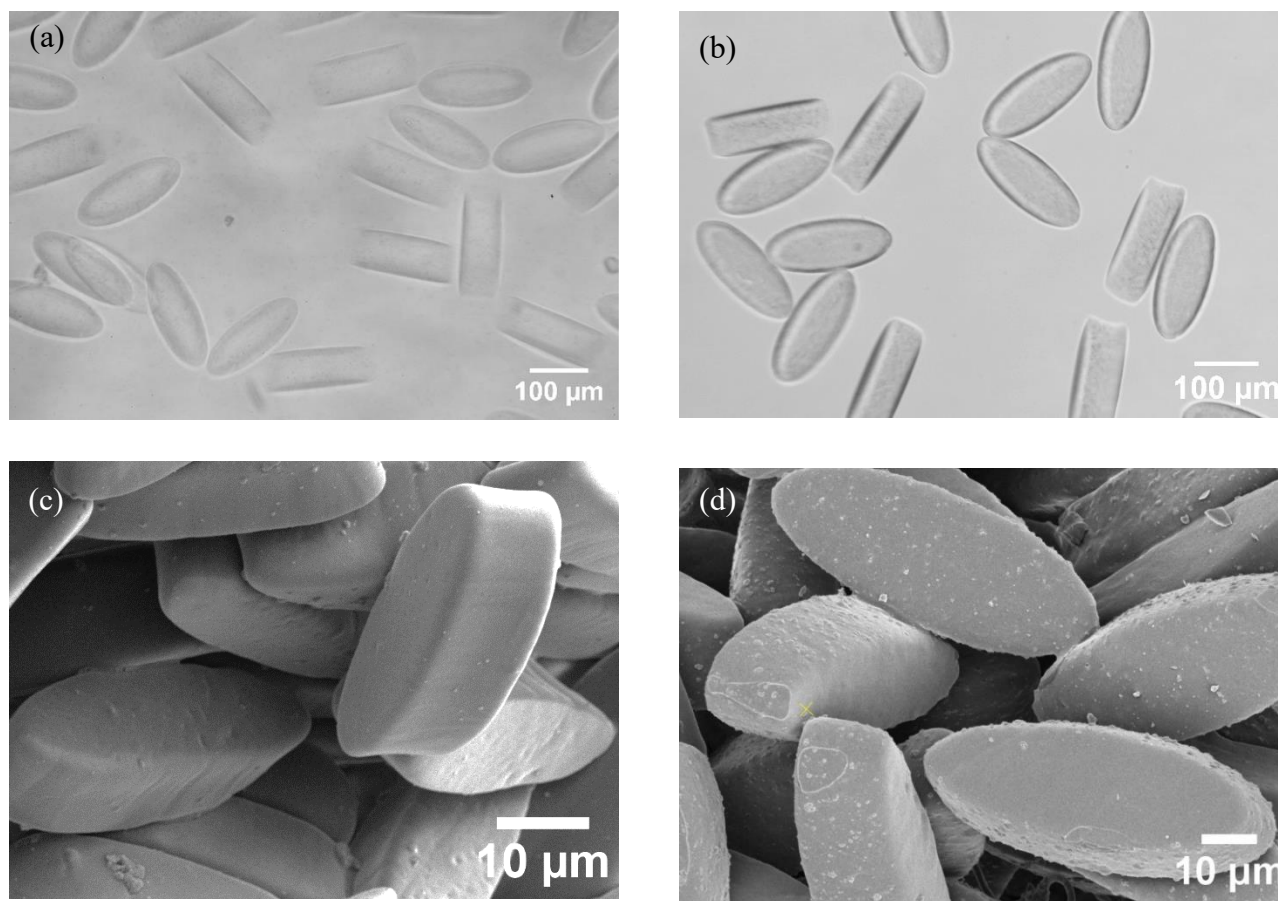


Figure 5.6: Photographs of oval shape polymer microparticles with embedded $\text{CoZnFe}_4\text{O}_8$ magnetic nanoparticles in cleaning solution, from (a) vial 1 and (b) vial 2; (b) SEM images of ceramic SiOC microparticles with embedded $\text{CoZnFe}_4\text{O}_8$ magnetic nanoparticles after pyrolysis transformation.

The particles were pyrolyzed at a temperature of 600 °C for 30 minutes. The temperature ramped up at a rate of 10 °C/min and cooled down at a rate of 2 °C/min. The temperature was selected to complete polymer to ceramic transformation and at the same time limit zinc evaporation. The temperature for melting zinc is 419 °C while boiling temperature is 908 °C. Oval microparticles were coated with Au/Pd to increase conductivity for image characterization with SEM and EDX. Oval ceramic microparticles containing the magnetic nanoparticles were analyzed with EDX to calculate the final content of embedded magnetic nanoparticles on both sides of the microparticles. The following elements present in the ceramic microparticles were corroborated using EDX elemental analysis: Zn, Co, Fe, Si, O, and C. Table 5.5 shows the average wt% of $\text{CoZnFe}_4\text{O}_8$ elements found in the fabricated microparticles from vial 1 and vial 2. $\text{CoZnFe}_4\text{O}_8$ has

a molecular weight of 210 gr/mol, where Fe accounts for 46.7 wt% of its molar mass. Assuming that the stoichiometric formula does not change, the wt% percent of $\text{CoZnFe}_4\text{O}_8$ was calculated for an average of 6 wt% of the oval microparticles for vial 1, while for vial 2 was calculated in 3 wt%. The presence of cobalt was found in microparticles from both vials. However, in the case of zinc, just one side of microparticles from 1 vial showed its presence, while the other showed no presence of Zinc. Additionally, the particles with no observed big particle agglomerates had the higher concentration of Fe and Co, while the ones showing the particle agglomerates had a lower concentration of Fe and Co. This result can be attributed to the mixing method. With more content of $\text{CoZnFe}_4\text{O}_8$, there is a higher chance of particle collision, agglomeration and sedimentation.

Table 5.5: Shows the elemental wt% calculated by EDX analysis for Oval SiOC particles containing $\text{CoZnFe}_4\text{O}_8$.

Particles from vial 1					Particles from vial 2				
Element	Side 1		Side 2		Element	Side 1		Side 2	
	wt%	Sigma	wt%	Sigma		wt%	Sigma	wt%	Sigma
C	61.18	1.02	59.51	0.75	C	44.3	0.23	47.9	0.17
O	27.01	0.95	13.86	0.58	O	19.75	0.14	22.58	0.12
Si	7.06	0.21	24.23	0.43	Si	33.21	0.14	28.6	0.1
Fe	3.75	0.45	1.91	0.25	Fe	2.08	0.03	0.72	0.02
Co	1	0.51	0.49	0.28	Co	0.6	0.03	0.2	0.01
Zn	0	0	0	0	Zn	0.06	0.03	0	0

XRD analysis was performed on the magnetic nanoparticles before and after 600 °C pyrolysis. It can be observed from figure 5.10 that the main peaks showing lattice parameters, and an overall structure of $\text{CoZnFe}_4\text{O}_8$ did not change during heat treatment at 600°C in argon atmosphere. The XRD analysis shows a pattern with peaks attributed to 220, 311, 400, 422, 511, and 400 planes,¹⁴² which belong to FCC cubic spinel structure that contains tetrahedral and octahedral sites.

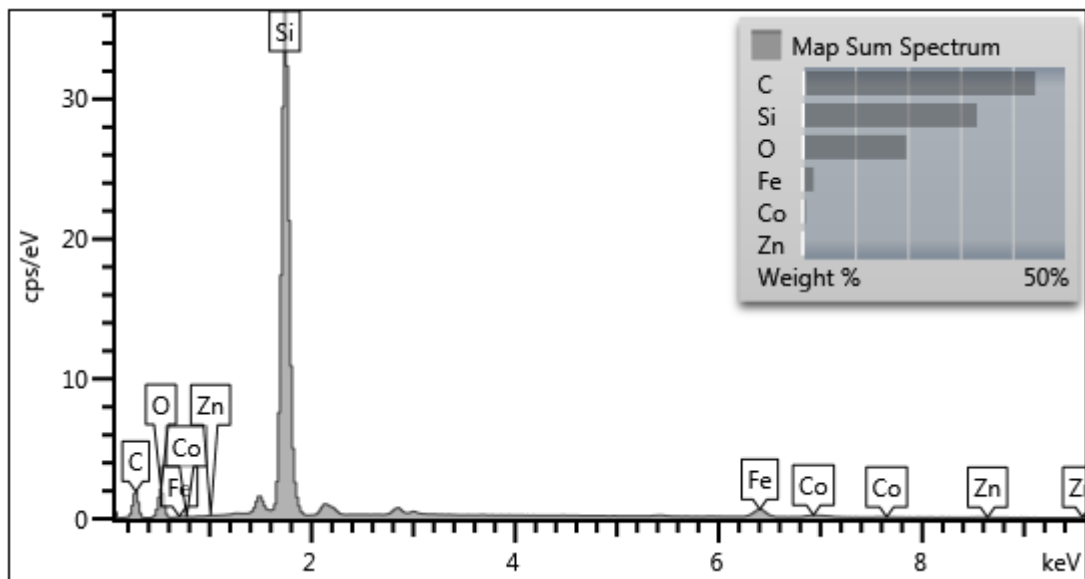


Figure 5.7: EDX analysis of oval ceramic microparticles with embedded $\text{CoZnFe}_4\text{O}_8$ magnetic nanoparticles. Particles from vial 2, side 1.

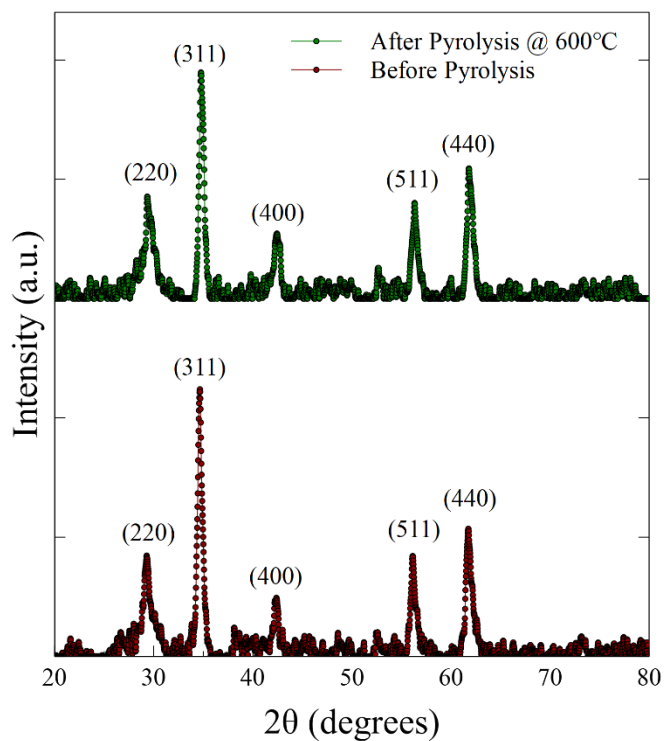


Figure 5.8: XRD data comparing scans for $\text{CoZnFe}_4\text{O}_8$ crystal structure before and after pyrolysis. The peaks are the spinel ferrite lattice planes.

5.3.3 Drug Targeting

Oval ceramic microparticles with embedded magnetic nanoparticles can be mobilized toward certain areas in a liquid media by controlling external magnetic fields. In the area of drug targeting, magnetic particles with oval shapes are moved towards a specific region in blood arteries to test particles as drug delivery systems.¹⁴³ Magnetic particle mobility in arteries has several factors affecting them, such as applied external magnetic forces, viscous forces, drag forces, inertia, blood-cell interaction, buoyancy, gravity, and interparticle effects, among others. However, the dominant forces are magnetic and viscous-drag forces.¹⁴⁴ The force balance for magnetic particles can be expressed with equation 5.3:

$$m_p \frac{dv_p}{dt} = F_m + F_d, \quad \text{Eq. 5.3}$$

where F_m is the magnetic force, F_d is the viscous-drag force, m_p is the particle mass, and v_p is the particle velocity. $m_p dv_p/dt$ can be understood as an inertial force and can be neglected.²² The magnetic force of the particle experience can be calculated with equation 5.4, where F_m is the magnetic force, v_p is the particle volume, M is the magnetization, and H is the applied field.

$$F_m = \mu_o V_p (M \cdot \nabla) H = \mu_o V_p \chi_{eff} M (\nabla) H \quad \text{Eq. 5.4}$$

Using identities and defining cartesian coordinates, F_m can be rewritten with equations 5.5 and 5.7, where μ_o is the permeability of vacuum, V_p is the volume of the particle, χ_{eff} is the susceptibility difference between the fluid and the magnetic particles, M_s is the magnetization of the source, R_{mag} is the radius of the magnetic field, x and y are the coordinate of the particle, and x_{mag} and y_{mag} are the coordinates of the center of the magnetic source.

$$F_{mx}(x, y) = \mu_o V_p \chi_{eff} M_s^2 R_{mag}^4 \frac{x - x_{mag}}{2[(y - y_{mag})^2 + (x - x_{mag})^2]^3} \quad \text{Eq. 5.5}$$

$$F_{my}(x, y) = \mu_o V_p \chi_{eff} M_s^2 R_{mag}^4 \frac{y - y_{mag}}{2[(y - y_{mag})^2 + (x - x_{mag})^2]^3} \quad \text{Eq. 5.6}$$

The visualization data with the colormap shown in figure 5.9 represent the magnetic field that four solenoids separated 10 cm vertically and 5 cm vertically from each other would exert

considering 1 Tesla of magnetic field strength. The colors are distributed in exponential form for the magnetic field. The minimum force needed to move a particle in a blood artery flow should be above $1 \times 10^{-12} \text{ N}$, force represented in blue.

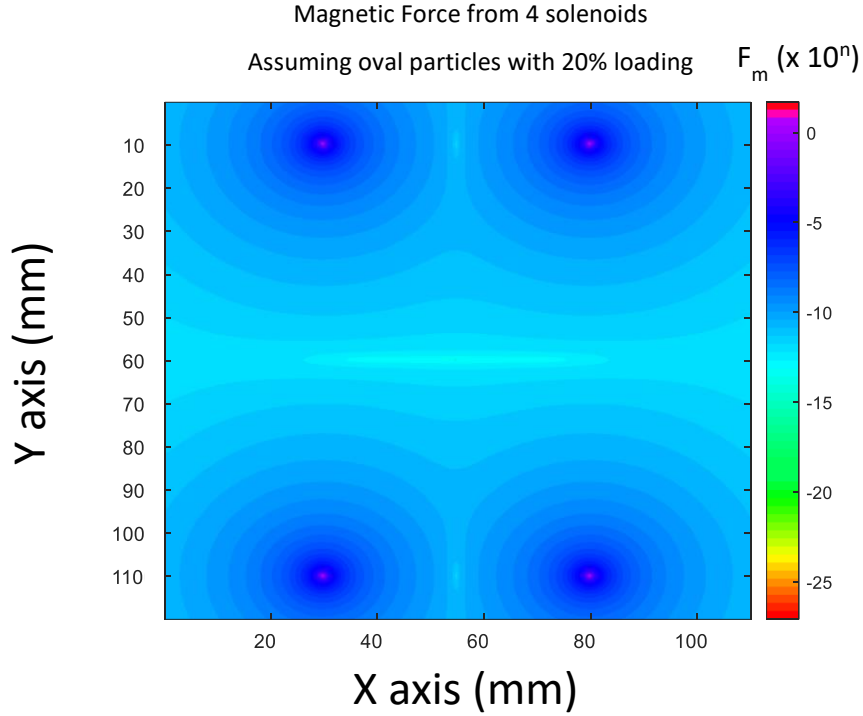


Figure 5.9: Magnetic force field with colors, showing the effect of 4 solenoids, with 10 cm of vertical distance and 5 cm of horizontal distance. The colors are shown in exponential form corresponding to 10^n , from 0 to -25.

The drag force equation acting against the motion of the particle is defined in equation 5.7, where F_d is the drag force, A is the particle reference area, ρ is the density of the fluid, and ΔV is the velocity of the particle with respect to the fluid. For the case of a bullet shape like particle, C_d is about 0.3.¹⁴⁵

$$F_d = C_D A \frac{\rho \Delta V^2}{2} \quad \text{Eq. 5.7}$$

In order to calculate the viability of these particles as drug carriers, a hypothetical case was studied to control particle trajectory. Assuming an arm sleeve with solenoids on it, a magnetic nanoparticle can be directed through a person's blood artery system, where solenoids at specific points can define the microparticle direction. We are studying a hypothetical case where the arm vein paths are

known, and the pathways are simplified into only two directions, this setup can be observed in figure 6.5. Sharzi et al.¹⁴⁶ calculated, experimentally and theoretically, the minimum force needed to move a particle in a blood-flow artery. Using equation 5.6, and the parameters used by Sharzi et al., the minimum magnetic force needed to move a particle inside a blood artery is 1.07×10^{-12} N.

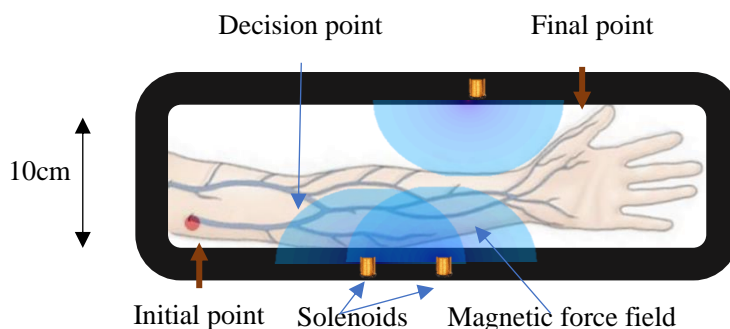


Figure 5.10: Schematic of arm with sleeve that contains 4 solenoids with an hypothetical strength of 1 Tesla to control magnetic particles directionality with magnetic field. Red arrows show initial and final desired points for a magnetic microparticle that acts as a drug carrier. Image of arms with arteries modified from original source from basicmedicalkey site.

Saturation magnetization, remnant magnetization, and susceptibility for the magnetic nanoparticles of ZnFe_2O_4 , $\text{NiZnFe}_2\text{O}_4$, NiFe_2O_4 , $\text{CoZnFe}_2\text{O}_4$, and CoFe_2O_4 provided by the supplier (Nanostructured and Amorphous Materials Inc., Katy, TX) are shown in Table 5.6(a). The geometry of the glove, the solenoid diameter and the particle volume are shown in table 5.6(b). Assuming a defined solenoid on both sides of the sleeve with a radius of 2.5 cm, a sleeve diameter of 10 cm, a sleeve thickness of 5 cm, with the dimensions of the previously fabricated ceramic microparticles containing magnetic nanoparticles, the solenoid strength necessary to control a drug carrier direction with increasing content of magnetic nanoparticles is shown in figure 5.10. Practical solenoid magnetic strengths for the radius considered for a permanent magnet are below 1 Tesla. Microparticles with a content of 10 wt% of $\text{CoZnFe}_2\text{O}_4$ would require solenoid strengths of ~ 2 Teslas. Microparticles containing $\text{NiZnFe}_2\text{O}_4$ require a lower content of embedded magnetic nanoparticles to achieve particle mobility, between 5 to 10 wt%.

Table 5.6 (a) Available ferrites from the selected supplier (Nanostructured and Amorphous Materials Inc., Katy, TX) with information about the saturation magnetization, the remnant magnetization, and the susceptibility. (b) Used parameters to calculate magnetic field strength needed to move a microparticle with magnetic loading.

(a)				(b)	
Modified Ferrites	Saturation Magnetization emu/g	Remnant Magnetization emu/g	Susceptibility	Used Parameters	
ZnFe ₂ O ₄	4	0.6	5.90E-04	Particle Volume	2.1 E4 μm^3
NiZnFe ₂ O ₄	51	4.2	1.20E-02	Diameter of glove	10 cm
NiFe ₂ O ₄	37.7	5.3	7.20E-03	Thickness of glove	5 cm
CoZnFe ₂ O ₄	27.5	5.7	1.20E-03	Solenoid Radius	2.5 cm
CoFe ₂ O ₄	46.8	17.3	6.50E-04		

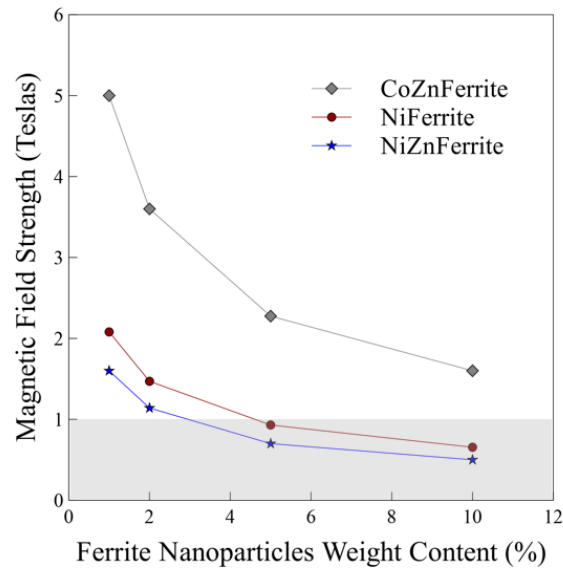


Figure 5.11: The magnetic field strength of two solenoids separated at a distance of 10 cm as shown in figure 5.10, for magnetic oval particles with the dimensions used in this chapter with loading (wt%) increasing from 1 to 10wt%.

5.4 Conclusions

Preceramic oval shape microparticles containing magnetic $\text{CoZnFe}_4\text{O}_8$ nanoparticles were fabricated successfully via SFL and transformed to ceramic SiOC after pyrolysis at 600 °C. This temperature allowed full polymer to ceramic conversion and minimum zinc evaporation. Magnetic nanoparticles were initially mixed using an ultrasonic horn with the preceramic siloxane polymer. From dipole-dipole interactions, ferrite nanoparticles suffer strong aggregation. Particle agglomerates $> 2 \mu\text{m}$ were separated from the suspension by sedimentation. UV transmittance did not show an important reduction inside the 75 μm PDMS microchannel for suspensions containing concentrations $\leq 1\text{wt}\%$. Due to the polymer to ceramic mass loss, magnetic nanoparticles embedded in the siloxane matrix increased their wt% in the microparticles final weight. An initial content of 0.1 wt% resulted in final content of 5 wt%, considering a preceramic mass loss conversion of 96%. As magnetic nanoparticle content increased, shrinkage reduced. The spinel ferrite fcc crystal structure of the magnetic nanoparticles was proved to be maintained after pyrolysis heat treatment. Co-doped ferrite structures with cobalt in addition to zinc is a great option to increase magnetic susceptibility and reduce remnant magnetization. Ferrimagnetic nanoparticles embedded in SiOC ceramic microparticles allow directional control with external magnetic fields, demonstrating feasibility to be used drug delivery carriers.

6. FABRICATION OF BIFUNCTIONAL POLYMER PRECERAMIC MICROPARTICLES VIA CONTINUOUS-FLOW LITHOGRAPHY

6.1 Introduction

Functional particles with two or more defined properties are of particular interest for the areas of self-assembly, self-propelled particles, and micromotors.¹⁴⁷ Specific particle shapes may contribute to catalyzing processes, guiding motion, or transporting chemicals, which permits complex processes to be achieved.¹⁴⁸ In addition, functional particles with anisotropic properties may enable self-assembly processes.¹⁴⁹ Shape anisotropy becomes an advantage in particle design to perform specific tasks. By doing so, chemical or physical properties may be applied with a demarcated directionality. Shapes such as dumbbells, disks, vesicles, capsules, and cylinders may benefit from a two-side property segmentation. Particles with two or more properties can be fabricated with flow lithography techniques by adding entrances to the PDMS microchannel molds. The vials containing the functional photosensitive solutions can be pumped into the PDMS microchannel with specific pressures. Figure 6.1 shows drawings of these types of particles.

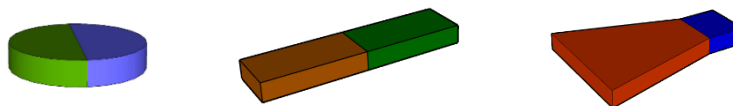


Figure 6.1: Drawings of potential particles having two sections, usually known as Janus particles. These types of particles can be fabricated with a 2-entrance microchannel PDMS device to be used in SFL.

To fabricate microparticles with two sections, continuous-flow lithography¹⁵⁰ (CFL) is the appropriate technique if the input fluids have a different rheological behavior. Inlet solutions with different properties as density and viscosity are necessary to generate a sharp interface between the fluids. When the inlet solutions have a different instantaneous viscosity, stop-flow lithography (SFL) is no longer the fastest method to fabricate multifunctional microparticles since the flow control becomes a complicated task. When fluids with different rheological behavior are pumped into the two entrance microchannel with air pulses, as they are with SFL technique, the solutions tend to mix or invade the opposite region leading to oscillating fluids inside the PDMS microchannel. For this reason, CFL was the technique selected to fabricate bifunctional

microparticles with porosity and magnetic properties. We present the fabrication of polymer preceramic particles such as dumbbells, dog-bone, and funnel-like shapes.

6.2 Experimental Setup

6.2.1 Materials, Characterization, and Methods

The microparticles were fabricated with the previously studied solutions, an emulsion and a suspension. For both solutions, the continuous phase was the preceramic polymer TEGO RC® 711 (Evonik®, Dusseldorf, Germany). Irgacure® 651 (Ciba®, Basel, Switzerland) photoinitiator was added initially to the preceramic polymer at 2.5 wt% to onset its UV photosensitive capability. The emulsion used was prepared as described in chapter 4, with droplets of DI-H₂O in TEGO RC® 711 emulsified with a two-step homogenization process. The content of the dispersed phase was 10 wt% and the droplets size range was $2 \pm 1 \mu\text{m}$. The surfactant Tween 80 (Sigma-Aldrich®, St. Louis, MO) was added at 1w% to DI-H₂O to minimize droplet coalescence. For the case of the suspension, CoZnFe₄O₈ (Nanostructured and Amorphous Materials Inc., Katy, TX) ferrimagnetic nanoparticles were added and homogenized with an ultrasonic horn to the preceramic polymer at a concentration of 1 wt% as described in chapter 5.

The PDMS microchannel device was fabricated using a two entrances vinyl self-adhesive film, a blunt needle, and an acrylic collection chamber mold, as observed in figure 6.2. The PDMS microchannel devices was constructed as described in chapter 2 with the stamp and stick method.⁷⁹ The dimensions of the microchannel fabrication area were 1.5 mm x 6 mm with a thickness of $75 \pm 5 \mu\text{m}$ in height.

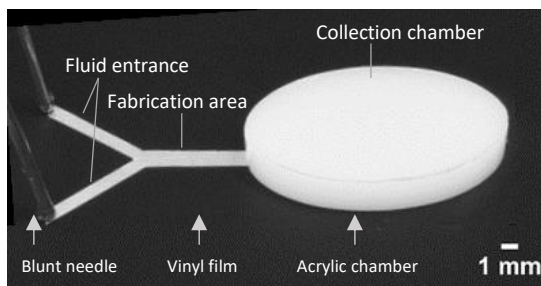


Figure 6.2: Photograph of microchannel mold showing the 3 different regions to imprint a PDMS microchannel device for the fabrication of bifunctional preceramic particles via CFL. It also shows the elements used for its construction. The scale bar is valid along the centerline of the image.

The vials containing the solutions were located inside the MitoS® air chambers (Dolomite®, Royston, United Kingdom) and pumped into PDMS microchannel with input pressures between 60 – 120 mbar. Photomasks with in-line printed shapes, as observed in the insets of figure 6.5 were used to fabricate the particles via CFL, by exposing pulsed UV light through the fluid in movement. The Arduino microcontroller only defined the pulses of the UV light (X-Cite 120, Excelitas®, Mississauga, ON) using the shutter drive (Uniblitz VS25S2ZM1R3-21, Vincent Associates, Rochester NY). The particles were collected and washed with isopropyl alcohol (IPA) as the cleaning solution. The recovered bifunctional preceramic polymer microparticles immersed in the cleaning solution were observed on an inverted microscope Axio Observer (Zeiss, Oberkochen, Germany), photographed with a camera (Nikon, Tokyo, Japan), and measured using ImageJ software.

6.2.2 Method

Continuous-flow lithography (CFL)¹⁵⁰ was the first of the flow lithography methods. It consists of a flow being fed continuously into a PDMS microchannel device, while pulses of UV light are exposed to the photosensitive solution passing through it. To allow a good definition of the particles, it is necessary to reduce flow velocity. In CFL, the entrance length as well as the fabrication area length have a minimum effect on the fluid behavior because the fluid does not run in flow cycles, and there is no need to stop and flush again the fluids.

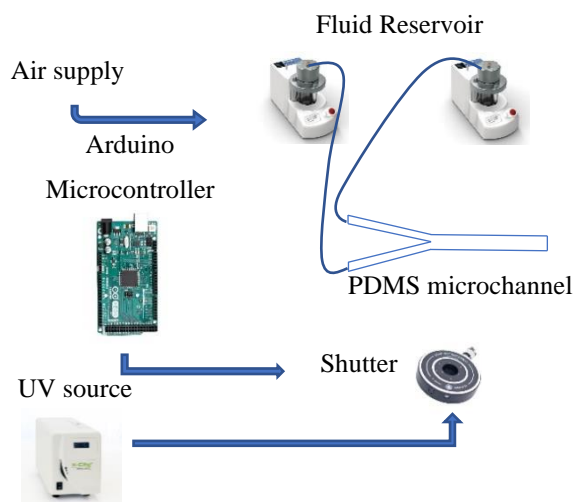


Figure 6.3: Schematic showing the microcontroller, the fluid reservoirs, the UV source, the shutter, and the PDMS microchannel device. The solutions were flown inside the PDMS microchannel with independent input pressures from the fluid reservoirs. UV pulses were controlled with the microcontroller and shutter and were exposed to the PDMS microchannel to polymerized bifunctional microparticles.

6.3 Results and Discussion

6.3.1 Liquid-Liquid Interface

When the solutions enter the microchannel, they may mix, change position or stay separated. As they are flown through the microchannel, their position might remain or change, depending on their equilibrium state. Whether or not the solutions will remain separated, depends on properties as solubility, velocity, viscosity and density. When 2 fluids of different density and/or viscosity flow in parallel inside a microchannel, at low speeds, an interface separating the fluids is formed. When the fluids have different properties, the interface travels with a specific velocity, different from the input solutions. As the velocity difference from the input fluid increases, the thickness of the interfacial layer increases as well.¹⁵¹ As the Reynolds number increases, flow instabilities known as Kelvin-Helmholtz start appearing. These flow instabilities are growing waves moving from fluid layer towards the region of the interfacial flow.¹⁵² In the event of particles or droplets in the input fluids with different properties, diffusion between layers will only exist when the particles or droplets would be able to cross the interfacial layer. Single particles or droplets in motion in a molecular liquid are dominated by intermolecular forces.¹⁵³ The inter particle or droplet collision can change their momentum to induce migration. Flow at low velocities with a defined interface through the PDMS microchannel is important to maintain the input fluids separated.

6.3.2 CFL Parameters

The main limitations of CFL for bifunctional microparticles are fabrication cycle times and a single photomask array. CFL has only two cycle times: exposure time (t_{exp}), and flush-out time (t_{flu}). As the speed of the solutions increases, the particles boundaries may lose definition. Since the velocity of the fluids is low, they can be induced with low input pressures or difference in height of the fluid reservoirs. The fluid velocity is an important parameter to define the particle definition and total cycle time. The other parameter that plays a role is UV exposure time, it must be fast and intense to initiate particle polymerization. The parameters used to fabricate the bifunctional microparticles inside a PDMS microchannel are shown in table 6.1 and 6.2. Parameters as microchannel input pressure, fluid speed, objective used, exposure time, and UV

intensity level, participated defining particle dimensions. These parameters were used to fabricate functional particles with two sections where the flow was moved in subtly at low speeds.

Table 6.1: Parameters used for the fabrication of dumbbell, ovals, and funnel-like preceramic polymer particles via CFL.

		Objective	Exposure time	Solution 1 (Suspension)	Solution 2 (Emulsion)
Dumbbell particles	Input pressure	10x	50ms	60 mbar	100 mbar
	Fluid speed			0.57 mm/s	0.96 mm/s
Ovals particles	Input pressure	20x	30 ms	60 mbar	100 mbar
	Fluid speed			0.57 mm/s	0.96 mm/s
Funnel-like particles	Input pressure	10x	50 ms	90 mbar	120 mbar
	Fluid speed			.85	1.14

Table 6.2: Additional parameters used for the fabrication of predefined shape bimodal preceramic polymer microparticles.

Parameters	10x Objective	20x Objective
UV Intensity	Level 4	Level 4
Exposure Time	50 ms	30 ms
Mchannel length	7 mm	7 mm
Fabrication length	1.3 mm	.65 mm
Minimum flush out time	3 sec.	1.5 sec.

It can be noted that microchannel length does not play an important role in the definition of the CFL fabrication cycle times, in contrast with SFL. Cycle times were between 4 - 7 seconds, for 3 – 7 particles per cycle.

6.3.3 Functional Particles

Particles with two sections, a preceramic polymer emulsion and a preceramic polymer suspension were fabricated via CFL, using a 2 entrance PDMS microchannel device. The properties of interest were porosity and magnetism. Particles with a magnetic side and a porous side can serve as controlled motion devices for the transport of physical or chemical elements. Figure 6.4 shows the entrance of a 2-inlet microchannel with the two different solutions. 3 different particle shapes were photopolymerized with 10x and 20x objective using the inverted microscope Axio Observer (Axio Observer, Zeiss America, Peabody, MA, USA), a UV source, a shutter, and

patterned photomasks. Three different particle shapes were fabricated with three different masks, which are shown below in figure 6.4.

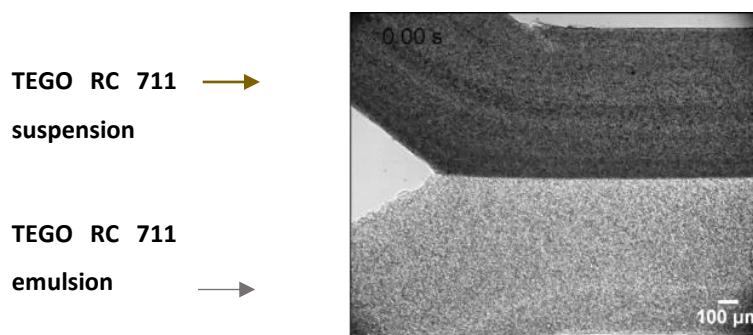


Figure 6.4: Image of the solutions entrance of a two-inlet PDMS microchannel device with two solutions, a suspension and an emulsion, prepared as described in chapter 4 and 5.

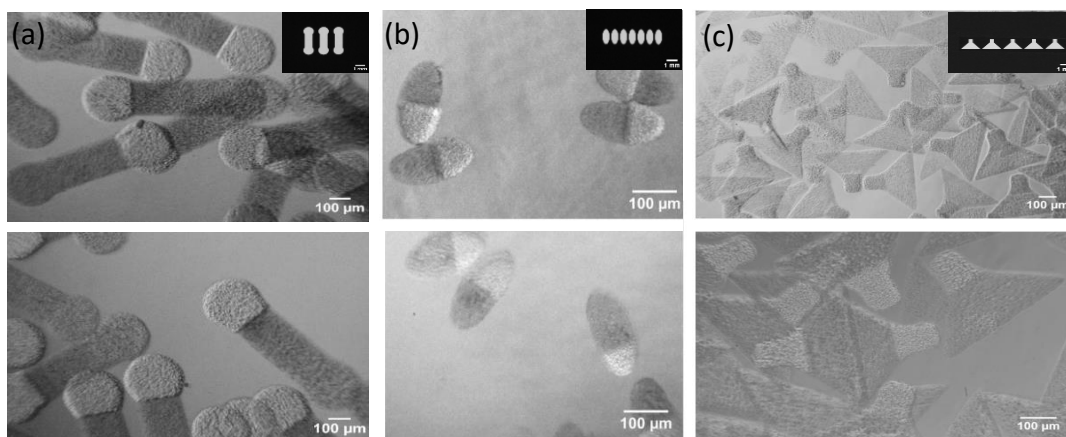


Figure 6.5: Optical images of microparticles with two sides, one porous and one magnetic, fabricated via CFL. The mask used to fabricate the shapes is shown in the inset of the upper row images.

The content of the emulsion used to fabricate the 3 different particle shapes was kept constant at 10 wt%. The initial content of the magnetic suspension was also kept constant at 1 wt%. However, for the case of the dumbbell shapes and the oval shapes, the suspension was used 1 day after preparation. In contrast, the suspension used to fabricate the funnel-like shape microparticles was used 14 days after preparation, allowing big particle agglomerates to sediment. Dumbbell and oval shape particles showed a different thickness between the polymerized emulsion side and the suspension side. For the case of the funnel-like microparticles, the thickness was even

along the particle cross section. Particle in figure 6.5 were observed in the cleaning solution, after collection and washing.

Table 6.3: Parameters and major dimensions for the 3 different microparticles fabricated via CFL, for 2 inlet fluids, an emulsion and a suspension.

	Shape 1 (Dumbbell)	Shape 2 (Ovals)	Shape 3 (Funnel-like)
Emulsion content	10 wt%	10 wt%	10 wt%
Suspension content	~ 1wt%	~ 1wt%	< 1wt%
Objective used	10x	20x	10x
Size reduction	25%	12.5%	12.5%
Exposure time	50 ms	30 ms	50 ms
Thickness	30 - 40 μm	30 - 40 μm	40 - 45 μm
Particle max. length	825 μm	185 μm	405 μm
Particle max. width	104 μm	85 μm	220 μm

6.4 Conclusions

Continuous flow lithography is a feasible option to fabricate bimodal microparticles from photosensitive fluids. The main limitation of CFL is cycle time constraints and single photomask array. Fluids with different densities and viscosities are necessary to form a sharp interface between the entrance input fluids. Polymer or ceramic microparticles may be fabricated with CFL method. By generating particles with 2 regions, porous and magnetic, controlled directionality with a carrier side can be fabricated in cycle repetitions. The porous side can serve as a region prone for surface modification or to carry physical or chemical elements. Porosity was introduced by generating an emulsion with the preceramic polymer and DI-H₂O. Ferrimagnetic nanoparticles were embedded into the preceramic matrix. Both solutions were fed into the PDMS microchannel to prepare the CFL cycle. Bimodal particles fabricated through this technique can be used, for instance, as drug carriers. The magnetic force needed to move these particles in a liquid media are shown in chapter 5. Ferromagnetic particles embedded in a ceramic or polymer silicon matrix are good candidates to control the direction of a particle with external magnetic fields.

7. FUTURE WORK

The fabrication of polymer and ceramic microparticles has applications in several areas. We presented the use of bifunctional microparticles for the drug delivery area, but certainly, other areas may benefit from these versatile set of fabrication techniques. We realized preliminary work in the fabrication of microbatteries and self-assembly structures. In this section, we briefly present the scope and future work for these projects.

7.1 Fabrication of Microbatteries

Fabrication of rechargeable microbatteries¹⁵⁴ with thicknesses in the micron range is an area of opportunity for flow lithography. Microbatteries particles can supply energy to sensors, MEMS, or microrobots. By reducing battery sizes, functional active devices in the micron range can become self-powered. Flow lithography techniques are of high interest due to their versatility and economical cost. Preceramic polymers are good candidates to serve as matrix materials for functional particles used for batteries. TEGO RC® 711 has proved to be a feasible matrix to load functional powders. The introduction of porosity and shrinkage during conversion are characteristics of interest for the fabrication of these devices. Additionally, converted TEGO® RC 711 into SiOC has also been suggested as anode⁶⁷ material.

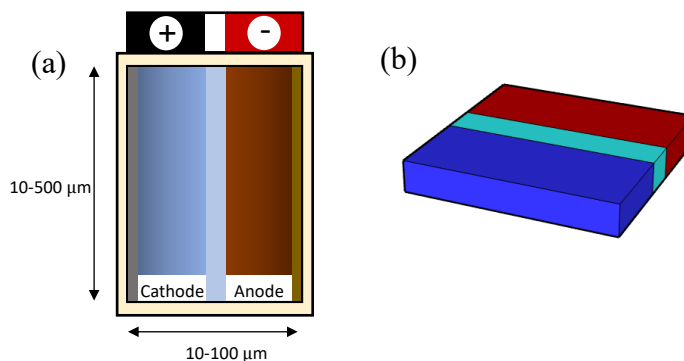


Figure 7.1: Schematic of microbatteries with three components: anode, separator and cathode. (a) Design considering porous spheres in the cathode and anode sections; (b) drawing of square shape with the three sections resembling a battery architecture.

The microchannel mold with three entrances was suggested to fabricate these types of devices with its three sections: the anode, the separator, and the cathode. The microchannel

fabricated consists of four areas: the entrance area, the mixing area, the exposure/fabrication area, and the collection area. The four areas of the microchannel mold can be observed in figure 7.2.

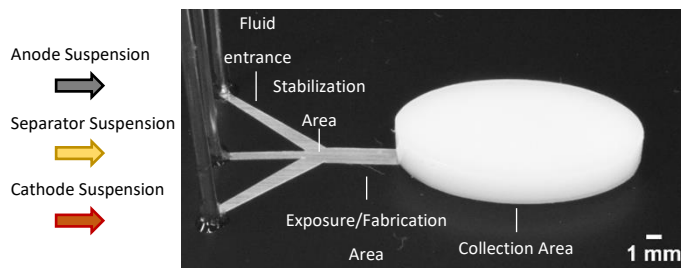


Figure 7.2: Photograph of microchannel mold with three entrances, indicating the microchannel regions for a three-entrance microchannel for the fabrication of microparticles with three different sections.

Anode, cathode and electrolyte materials were first loaded in PEGDA 400 and PEGDA 700, both with different viscosities. The loading of the suspensions of the functional powders were < 20 wt%, with particle sizes between 1 and 10 μm , which led to areas of aggregation. Images of the anode, separator (electrolyte only), and cathode can be observed in figure 7.3.

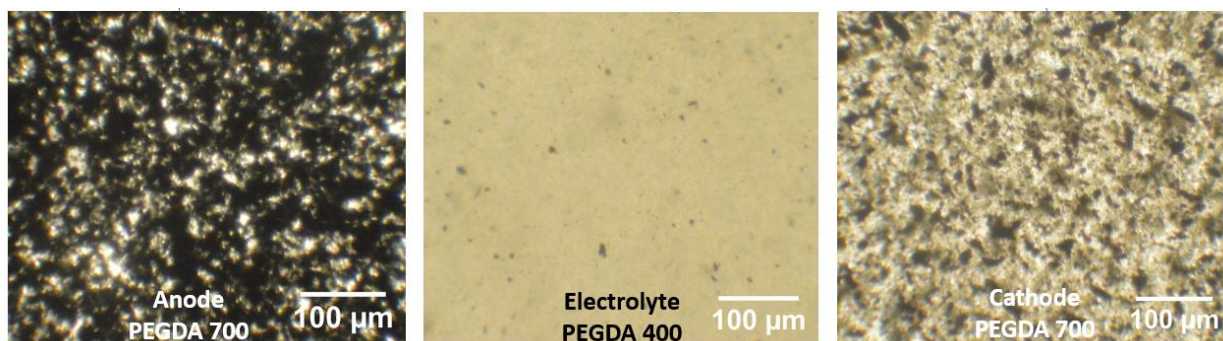


Figure 7.3: Photographs showing suspensions containing functional powders for anode, separator, and cathode for the fabrication of microbatteries via SFL.

To achieve a sharp interface, the solutions in the three different sections should have different viscosity and density characteristics. In addition to PEGDA 400 and 700, we also used TEGO® RC 711 as the anode and cathode matrix. This material was a good candidate due to its immiscibility and difference in viscosity with PEGDA. The respective viscosity of TEGO® RC 711 was 600 cSt and the viscosity of PEGDA 400 was 50 cSt. TEGO® RC 711 contained the heavier elements—graphite and LiCoO_2 in the outer sections—to reduce sedimentation, particle

migration, and agglomeration. The lighter powders (electrolyte) were in the separator (middle) entrance. Figure 7.4 shows the entrance of the three fluids in the microchannel.

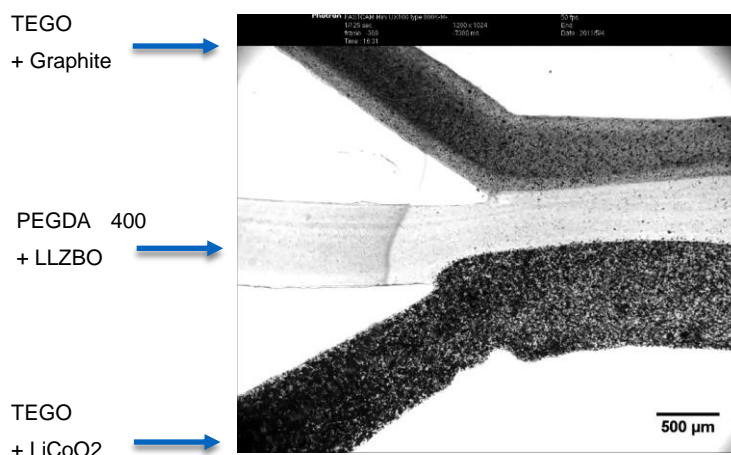


Figure 7.4: PDMS microchannel device with 3 entrances having components of a microbattery, the anode, the separator, and the cathode. The 3 suspensions have different loadings. The middle fluid contained PEGDA 400 as the photopolymer matrix, while the outer regions contained TEGO RC® 711 as the photopolymer matrix.

7.2 Self-Assembly Particles

Self-assembly is an area that has gained a lot of attention in recent years.¹⁵⁵ The study of autonomous components that may organize in patterned structures without external intervention has fascinated researchers.¹⁵⁶ Interaction among particles in fluid phases or smooth surfaces, allow particle mobility and self-arrangement into equilibrium states. For example, self-assembly in molecules occurs with non-covalent or weak covalent interactions.¹⁵⁷ The environment in which the molecules or particles are immersed or in contact, intervene in their interaction. Self-assembly of microparticles is another area of opportunity for microparticles fabricated through flow lithography techniques. Particles with defined characteristics may develop selective attraction or repulsion among them. Particle's characteristics as shape, surface energy, charge, polarizability, magnetic dipoles, mass, etc., may define their interaction.¹⁵⁵ Figure 7.5 shows particle shapes of diverse materials forming greater structures.

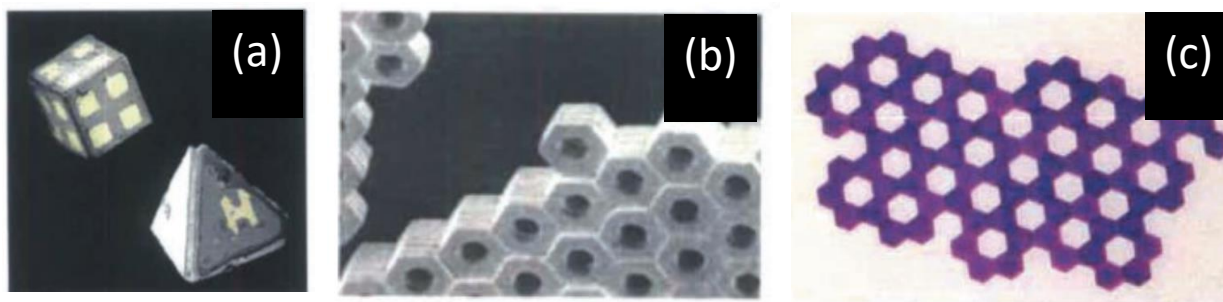


Figure 7.5: (a) Micron size polyhedral folded from planar substrates, (b) 3D aggregate of micron size plates assembled by capillary forces, and (c) millimeter polymeric plates assembled at water/perfluorodecalin interface by capillary interactions. Reproduced from ref 154 with permission from The American Association for the Advancement of Science, copyright 2002.

Interactions of particular interest are hydrophobicity and hydrophilicity, which are forces based in surface tension of a material. These types of forces may occur only when the particles are almost in contact. In the case of the preceramic polymer that we used, TEGO® RC 711, it showed a hydrophobic behavior. After hexagonal shape preceramic polymer microparticles were fabricated, they were washed, and then collected with DI-H₂O, since it led to particle agglomeration. It can be observed that if this type of aggregation follows some order, particles could self-assemble, building a higher order structure. Figure 7.6 shows how polymer hexagons fabricated via SFL collected in water tended to align and form a close structure. Additionally, after conversion, converted TEGO RC ® 711 ceramic microparticles (known as black glass) can also be treated with glass modifiers to change their surface behavior into hydrophilic or hydrophobic.

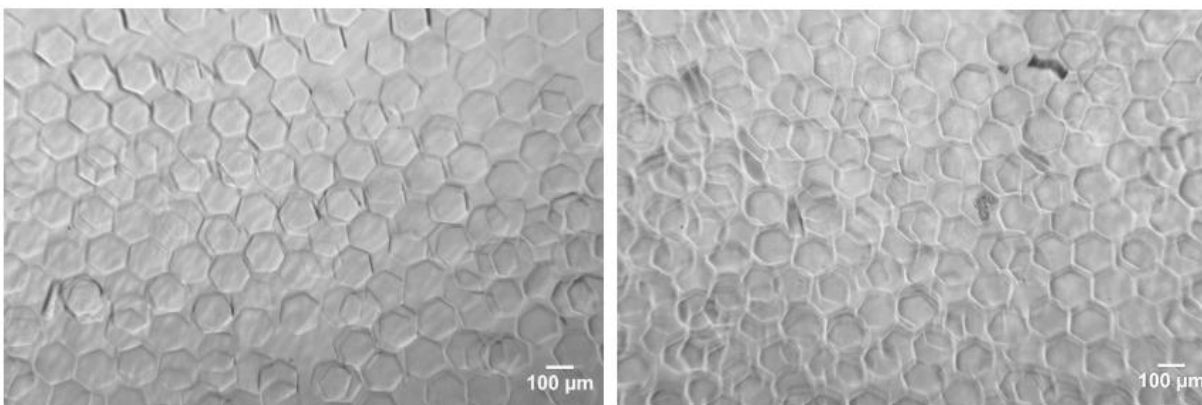


Figure 7.6: Hexagon polysiloxane polymer TEGO RC ® 711 microparticles fabricated via SFL and collected in DI-H₂O. The hexagons agglomerated due to their hydrophobic characteristic.

Considering the way in which microparticles can align and form greater structures, when they flow close to each other in liquid media, pattern shapes containing two sections were suggested to fabricate microparticles that could self-assemble into a higher order structure (figure 7.6). These designs are proposed as structures that can cover an entire area. For instance, shapes showed in image 7.7(b) use a known structure (I-beam) to minimize area and maximize mechanical strength when a load in the y direction is applied, by transmitting force to nodal points. The difference in color of the shapes suggest particles with 2 different properties, as hydrophilic and hydrophobic, in a way that certain surfaces can be attracted instead of the opposite one.

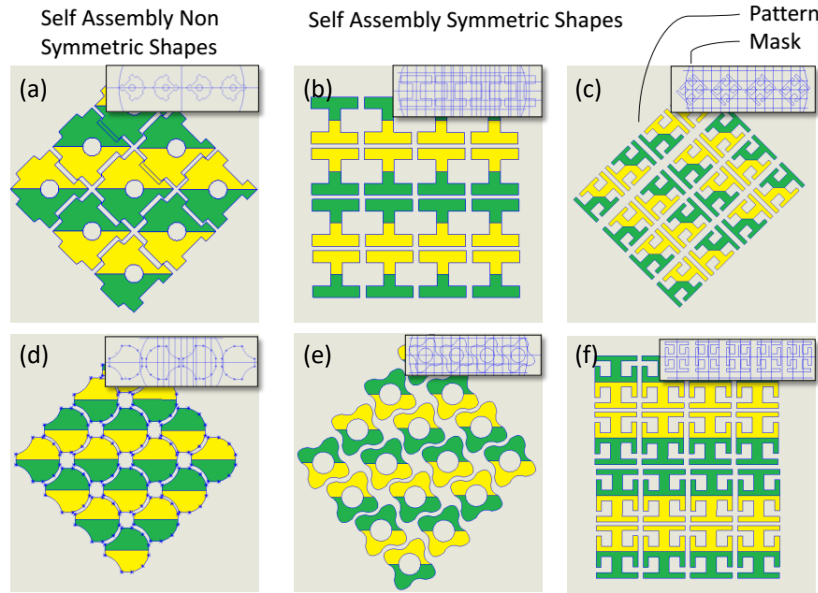


Figure 7.7: Drawings showing potential shapes that can be fabricated assuming two different properties: potentially one that is hydrophilic and one that is hydrophobic for self-assembly structures.

7.3 Conclusions

Preliminary work was performed for the fabrication of microbatteries and self-assembly particles. The goal was to show the application of a particle having two and three different sections. Functional powders can be loaded in the preceramic polymer matrix, to either treat them as polymers or convert them into ceramics. For the case of the microbatteries, it is important to have the input fluids with different properties as density, viscosity or solubility, to achieve sharp interfaces that will separate the phases. For the case of the self assembly particles, they could have one phase or two phases, where the phases could be hydrophilic and hydrophobic, that can lead to specific structure arrangements. Microparticles may develop a specific function or be designed to

generate a higher order structure. SFL and CFL are practical, versatile, and economical techniques to fabricate functional or multifunctional microparticles, either for polymers or ceramics. Not only electro-magnetic forces, but also Van der Waals forces can be exploited in the micron-range. In the case of suspensions or emulsions it is important to optimize them with the fluid matrix to achieve a stable solution.

8. CONCLUSIONS

Stop-flow lithography (SFL) is a fast and versatile technique for fabricating microparticles with defined shapes. By introducing new materials as preceramic polymers to SFL technique, polymer particles with improved properties can be easily molded. After collection, washing, and drying they were converted to ceramic materials via pyrolysis, by losing silanol and methoxide groups and rearranging Si-O and Si-C bonds. Vinyl films are replicable, inexpensive, and versatile way of fabricating microchannel molds to be used for SFL fabrication. The thickness of the vinyl film selected will determine initial particle height. Other two sources of variability were encountered, UV light projection distribution and oxygen consumption through fabrication cycles. Particle size variability cannot be avoided but it can be minimized. By mitigating variability, particles can have a narrow size distribution.

By using an acrylated polysiloxane preceramic precursor to fabricate ceramic SiOC particles, the fabrication of other ceramic microparticles such as SiC, Si₃N₄ and SiO₂ through preceramic polymers has shown to be feasible. The pyrolysis conversion of the preceramic polymer led to linear shrinkage of ~80%. SiOC is a hard, biocompatible and chemically inert material that can resist temperatures up to 1200°C. It is recommended to perform a post UV treatment after the particles have been fabricated and collected, preferably during the washing step where the excess of crosslink monomer is removed. By doing so, the conversion of polymer within the particles can be completed.

Porosity can be introduced in a preceramic polymer material by initially generating a photosensitive emulsion. Droplets serving as a sacrificial material can have tunable sizes by controlling the energy input when the continuous and discontinuous phases of an emulsion are mixed. After reaching a minimum average drop size through laminar homogenization, turbulent homogenization may be used to continue to decrease droplet size proportional to the power law $e^{(2/5)}$. Porous content through emulsion generation was introduced up to 30%. Droplets were observed to migrate during solution feed into the microchannel, which led to a higher concentration of droplets on one side of the particle compared to the other. By defining microchannel length and velocity of input solution, porosity gradients can be achieved.

Magnetic microparticles are a promising option to act as drug carriers for drug delivery area. Ferrimagnetic nanoparticles embedded in SiOC ceramic microparticles may be controlled with

external magnetic fields. Co-doped ferrite structures with cobalt or nickel in addition to zinc can increase magnetic susceptibility and reduce remnant magnetization of a ferrimagnetic material. The spinel ferrite fcc crystal structure of the magnetic nanoparticles was proved to remain after pyrolysis heat treatment. Additionally, bimodal particles containing a porous side and a magnetic side were fabricated with Continuous Flow Lithography (CFL) technique, showing feasibility to serve as controlled carriers. Fabrication of preceramic polymer microparticles for other applications as microbatteries or self-assembly particles was also demonstrated to be feasible.

APPENDIX A. ARDUINO PROGRAM

Arduino SFL Program

```
//YWROBOT
//Compatible with the Arduino IDE 1.0
//Library version:1.1
#include <LiquidCrystal_I2C.h>

LiquidCrystal_I2C lcd(0x27,20,4); // set the LCD address to 0x27 for a 16 chars and 2 line
display

void setup()
{

    const int analogPin = A12;//the analog input pin for POT 1

    int inputValue = 0;//variable to store the value coming from sensor
    int outputValue = 250 ;

    const int analogPin2 = A8;//the analog input pin for POT 2

    int inputValue2 = 0;//variable to store the value coming from sensor
    int outputValue2 = 250 ;

    const int analogPin4 = A0;//the analog input pin for POT 2

    int inputValue4 = 0;//variable to store the value coming from sensor
    int outputValue4 = 250 ;

    const int analogPin6 = A10;//the analog input pin for POT 2

    int inputValue6 = 0;//variable to store the value coming from sensor
    int outputValue6 = 250 ;

}

void loop()
{

    const int ledPin = 12;    // the number of the LED pin // LED Pin On
    pinMode(ledPin, OUTPUT);
```

```

const int buttonPin = 7; // Initialize Pin 7 NC/NO transistor
pinMode(7, OUTPUT); // declare pin 7 to be an output

int buttonState = 0; // Set NC/NC variable name
pinMode(buttonPin, INPUT); // Set Input variable

buttonState = digitalRead(buttonPin); // ButtonStated digitalread ButtonPin

digitalWrite(ledPin, LOW);

const int analogPin = A12; // the analog input pin for POT 1

int inputValue = 0; // variable to store the value coming from sensor
int outputValue = 250 ;

const int analogPin2 = A8; // the analog input pin for POT 2

int inputValue2 = 0; // variable to store the value coming from sensor
int outputValue2 = 250 ;

const int analogPin4 = A0; // the analog input pin for POT 2

int inputValue4 = 0; // variable to store the value coming from sensor
int outputValue4 = 250 ;

const int analogPin6 = A10; // the analog input pin for POT 2

int inputValue6 = 0; // variable to store the value coming from sensor
int outputValue6 = 250 ;

for (int i=0; i<3600; i++)

{
  //if pushButton is On

  if (buttonState == HIGH)
  {

    while (buttonState == HIGH)

    {

      digitalWrite(ledPin, HIGH);

      inputValue = analogRead(analogPin); //read the value from the sensor

```

```
    outputValue = map(inputValue,0,1023,100,1001);//Convert from 0-1023 to 10 to 1000
Exposure
```

```
    inputValue2 = analogRead(analogPin2); //read the value from the sensor
    outputValue2 = map(inputValue2,0,1023,100,1001);//Convert from 0-1023 to 10 to 1000
Dark
```

```
    inputValue4 = analogRead(analogPin4); //read the value from the sensor
    outputValue4 = map(inputValue4,0,1023,100,1001);//Convert from 0-1023 to 10 to 1000
Flush out
```

```
    inputValue6 = analogRead(analogPin6); //read the value from the sensor
    outputValue6 = map(inputValue6,0,1023,100,1001);//Convert from 0-1023 to 10 to 1000
Flush out
```

```
    lcd.init();           // initialize the lcd
    // Print a message to the LCD.
    lcd.backlight();
    lcd.setCursor(0,0);
    lcd.print("Ex:");
    lcd.setCursor(3,0);
    lcd.print(outputValue);
```

```
    lcd.setCursor(8,0);
    lcd.print("Dk:");
    lcd.setCursor(11,0);
    lcd.print(outputValue2);
```

```
    lcd.setCursor(0,1);
    lcd.print("Fh:");
    lcd.setCursor(3,1);
    lcd.print(outputValue4);
```

```
    lcd.setCursor(8,1);
    lcd.print("St:");
    lcd.setCursor(11,1);
    lcd.print(outputValue6);
```

```
}
```

```
}
```

```
else if (buttonState == LOW) {
```

```
    inputValue = analogRead(analogPin); //read the value from the sensor
```

```
    outputValue = map(inputValue,0,1023,100,1001);//Convert from 0-1023 to 10 to 1000
Exposure time
```

```
    inputValue2 = analogRead(analogPin2); //read the value from the sensor
    outputValue2 = map(inputValue2,0,1023,100,1001);//Convert from 0-1023 to 10 to 1000
Dark Polymerization time
```

```
    inputValue4 = analogRead(analogPin4); //read the value from the sensor
    outputValue4 = map(inputValue4,0,1023,100,1001);//Convert from 0-1023 to 10 to 1000
Flush out time
```

```
    inputValue6 = analogRead(analogPin6); //read the value from the sensor
    outputValue6 = map(inputValue6,0,1023,100,1001);//Convert from 0-1023 to 10 to 1000
Stop time
```

```
    lcd.init();           // initialize the lcd
    // Print a message to the LCD.
    lcd.backlight();
    lcd.setCursor(0,0);
    lcd.print("Ex:");
    lcd.setCursor(3,0);
    lcd.print(outputValue);
```

```
    lcd.setCursor(8,0);
    lcd.print("Dk:");
    lcd.setCursor(11,0);
    lcd.print(outputValue2);
```

```
    lcd.setCursor(0,1);
    lcd.print("Fh:");
    lcd.setCursor(3,1);
    lcd.print(outputValue4);
```

```
    lcd.setCursor(8,1);
    lcd.print("St:");
    lcd.setCursor(11,1);
    lcd.print(outputValue6);
```

```
while (buttonState == LOW)
```

```
{
    analogWrite(3, 255);           // EXOPOSURE set the brightness of pin 3: AMARILLO -
UV On
```

```
    delay(outputValue);           //FIJO    //wait for 1000ms
```



```
analogWrite(3, 0);          // set the brightness of pin 3: AMARILLO
delay(outputValue2);
digitalWrite(ledPin,HIGH);   // LED ROJO - FLOW
delay(outputValue4);
digitalWrite(ledPin,LOW);    // LED ROJO
delay(outputValue6);
digitalWrite(ledPin, LOW);
}
}
}
}
```

REFERENCES

- (1) Li, H.; Tan, J.; Zhang, M. Dynamics Modeling and Analysis of a Swimming Microrobot for Controlled Drug Delivery. *IEEE Trans. Autom. Sci. Eng.* **2009**, 6 (2), 220–227. <https://doi.org/10.1109/TASE.2008.917137>.
- (2) Wang, W.; Castro, L. A.; Hoyos, M.; Mallouk, T. E. Autonomous Motion of Metallic Microrods Propelled by Ultrasound. *ACS Nano* **2012**. <https://doi.org/10.1021/nn301312z>.
- (3) Olivas, J. D.; Bolin, S. Advancements in MEMS Materials and Processing Technology. *Jom* **1998**, 50 (1), 38–43. <https://doi.org/10.1007/s11837-998-0066-3>.
- (4) Wong, F.; Dey, K. K.; Sen, A. Synthetic Micro/Nanomotors and Pumps: Fabrication and Applications. *Annu. Rev. Mater. Res.* **2016**, 46 (1), 407–432. <https://doi.org/10.1146/annurev-matsci-070115-032047>.
- (5) Shimoyama, I. Scaling in Microrobots. *IEEE Int. Conf. Intell. Robot. Syst.* **1995**, 2, 208–211. <https://doi.org/10.1109/iros.1995.526161>.
- (6) Fukuda, T.; Arai, F. Microrobot and Applications. *IEEE Int. Conf. Emerg. Technol. Fact. Autom. ETFA* **1993**, 1–8. <https://doi.org/10.1109/ETFA.1993.396435>.
- (7) Sahai, R.; Avadhanula, S.; Groff, R.; Steltz, E.; Wood, R.; Fearing, R. S. Towards a 3g Crawling Robot through the Integration of Microrobot Technologies. *Proc. - IEEE Int. Conf. Robot. Autom.* **2006**, 2006 (May), 296–302. <https://doi.org/10.1109/ROBOT.2006.1641727>.
- (8) Churaman, W. A.; Gerratt, A. P.; Bergbreiter, S. First Leaps toward Jumping Microrobots. *2011 IEEE/RSJ Int. Conf. Intell. Robot. Syst.* **2011**, 2 (2), 1680–1686. <https://doi.org/10.1109/iros.2011.6095090>.
- (9) Kubo, Y.; Miura, H. ? ? A. **1993**, No. 3, 386–391.
- (10) Abbott, J. J.; Peyer, K. E.; Lagomarsino, M. C.; Zhang, L.; Dong, L.; Kaliakatsos, I. K.; Nelson, B. J. How Should Microrobots Swim? *Int. J. Rob. Res.* **2009**, 28 (11–12), 1434–1447. <https://doi.org/10.1177/0278364909341658>.
- (11) 38. White, Viscous Fluid Flow, Vol. 3. New York: McGraw-Hill, 2006.
- (12) Yesin, K. B.; Vollmers, K.; Nelson, B. J. Modeling and Control of Untethered Biomicrobots in a Fluidic Environment Using Electromagnetic Fields. *Int. J. Rob. Res.* **2006**, 25 (5–6), 527–536. <https://doi.org/10.1177/0278364906065389>.

- (13) Zhang, L.; Abbott, J. J.; Dong, L.; Kratochvil, B. E.; Bell, D.; Nelson, B. J. Artificial Bacterial Flagella: Fabrication and Magnetic Control. *Appl. Phys. Lett.* **2009**, *94* (6), 13–15. <https://doi.org/10.1063/1.3079655>.
- (14) Nelson, B. J.; Kaliakatsos, I. K.; Abbott, J. J. Microrobots for Minimally Invasive Medicine. *Annu. Rev. Biomed. Eng.* **2010**, *12* (1), 55–85. <https://doi.org/10.1146/annurev-bioeng-010510-103409>.
- (15) McBain, S. C.; Yiu, H. H. P.; Dobson, J. Magnetic Nanoparticles for Gene and Drug Delivery. *Int. J. Nanomedicine* **2008**, *3* (2), 169–180. <https://doi.org/10.2147/ijn.s1608>.
- (16) Lübke, A. S.; Bergemann, C.; Huhnt, W.; Fricke, T.; Riess, H.; Brock, J. W.; Huhn, D. Preclinical Experiences with Magnetic Drug Targeting: Tolerance and Efficacy. *Cancer Res.* **1996**, *56* (20), 4694–4701.
- (17) Loh, Q. L.; Choong, C. Three-Dimensional Scaffolds for Tissue Engineering Applications: Role of Porosity and Pore Size. *Tissue Eng. - Part B Rev.* **2013**, *19* (6), 485–502. <https://doi.org/10.1089/ten.teb.2012.0437>.
- (18) Vakifahmetoglu, C.; Zeydanli, D.; Ozalp, V. C.; Borsa, B. A.; Soraru, G. D. Hierarchically Porous Polymer Derived Ceramics: A Promising Platform for Multidrug Delivery Systems. *Mater. Des.* **2018**, *140*, 37–44. <https://doi.org/10.1016/j.matdes.2017.11.047>.
- (19) Wang, H.; Gu, X.; Wang, C. Self-Propelling Hydrogel/Emulsion-Hydrogel Soft Motors for Water Purification. *ACS Appl. Mater. Interfaces* **2016**, *8* (14), 9413–9422. <https://doi.org/10.1021/acsami.6b00197>.
- (20) Isojima, T.; Suh, S. K.; Sande, J. B. V.; Hatton, T. A. Controlled Assembly of Nanoparticle Structures: Spherical and Toroidal Superlattices and Nanoparticle-Coated Polymeric Beads. *Langmuir* **2009**, *25* (14), 8292–8298. <https://doi.org/10.1021/la900522u>.
- (21) Kim, S.; Qiu, F.; Kim, S.; Ghanbari, A.; Moon, C.; Zhang, L.; Nelson, B. J.; Choi, H. Fabrication and Characterization of Magnetic Microrobots for Three-Dimensional Cell Culture and Targeted Transportation. *Adv. Mater.* **2013**, *25* (41), 5863–5868. <https://doi.org/10.1002/adma.201301484>.
- (22) Sharma, S.; Gaur, A.; Singh, U.; Katiyar, V. K. Modeling and Simulation of Magnetic Nanoparticles Transport in a Channel for Magnetic Drug Targeting. 116–120.

- (23) Rotariu, O.; Strachan, N. J. C. Modelling Magnetic Carrier Particle Targeting in the Tumor Microvasculature for Cancer Treatment. *J. Magn. Magn. Mater.* **2005**, *293* (1), 639–646. <https://doi.org/10.1016/j.jmmm.2005.01.081>.
- (24) Kim, H. S.; Kim, J. H.; Kim, J. A Review of Piezoelectric Energy Harvesting Based on Vibration. *Int. J. Precis. Eng. Manuf.* **2011**, *12* (6), 1129–1141. <https://doi.org/10.1007/s12541-011-0151-3>.
- (25) Chen, X.; Ware, H. O. T.; Baker, E.; Chu, W.; Hu, J.; Sun, C. The Development of an All-Polymer-Based Piezoelectric Photocurable Resin for Additive Manufacturing. *Procedia CIRP* **2017**, *65*, 157–162. <https://doi.org/10.1016/j.procir.2017.04.025>.
- (26) Tian, X.; Jin, J.; Yuan, S.; Chua, C. K.; Tor, S. B.; Zhou, K. Emerging 3D-Printed Electrochemical Energy Storage Devices: A Critical Review. *Adv. Energy Mater.* **2017**, *7* (17), 1–17. <https://doi.org/10.1002/aenm.201700127>.
- (27) Sun, K.; Wei, T. S.; Ahn, B. Y.; Seo, J. Y.; Dillon, S. J.; Lewis, J. A. 3D Printing of Interdigitated Li-Ion Microbattery Architectures. *Adv. Mater.* **2013**, *25* (33), 4539–4543. <https://doi.org/10.1002/adma.201301036>.
- (28) Kata, M.; Wayer, M.; Gyorgy, E. Microcapsulation by Spray Drying. *Acta Pharm. Hung.* **1983**, *53* (1), 36–43. <https://doi.org/10.1080/07373939808917460>.
- (29) Shah, R. K.; Shum, H. C.; Rowat, A. C.; Lee, D.; Agresti, J. J.; Utada, A. S.; Chu, L. Y.; Kim, J. W.; Fernandez-Nieves, A.; Martinez, C. J.; et al. Designer Emulsions Using Microfluidics. *Mater. Today* **2008**, *11* (4), 18–27. [https://doi.org/10.1016/S1369-7021\(08\)70053-1](https://doi.org/10.1016/S1369-7021(08)70053-1).
- (30) Acharya, G.; Shin, C. S.; McDermott, M.; Mishra, H.; Park, H.; Kwon, I. C.; Park, K. The Hydrogel Template Method for Fabrication of Homogeneous Nano/Microparticles. *J. Control. Release* **2010**, *141* (3), 314–319. <https://doi.org/10.1016/j.jconrel.2009.09.032>.
- (31) Guan, J.; Ferrell, N.; James Lee, L.; Hansford, D. J. Fabrication of Polymeric Microparticles for Drug Delivery by Soft Lithography. *Biomaterials* **2006**, *27* (21), 4034–4041. <https://doi.org/10.1016/j.biomaterials.2006.03.011>.
- (32) Rajurkar, K. P.; Levy, G.; Malshe, A.; Sundaram, M. M.; McGeough, J.; Hu, X.; Resnick, R.; DeSilva, A. Micro and Nano Machining by Electro-Physical and Chemical Processes. *CIRP Ann. - Manuf. Technol.* **2006**, *55* (2), 643–666. <https://doi.org/10.1016/j.cirp.2006.10.002>.

- (33) Revzin, A.; Russell, R. J.; Yadavalli, V. K.; Koh, W. G.; Deister, C.; Hile, D. D.; Mellott, M. B.; Pishko, M. V. Fabrication of Poly(Ethylene Glycol) Hydrogel Microstructures Using Photolithography. *Langmuir* **2001**, *17* (18), 5440–5447. <https://doi.org/10.1021/la010075w>.
- (34) Devon, M. Tamarind Techniques for Fine Art Lithography. **2008**.
- (35) Gates, B. D.; Xu, Q.; Stewart, M.; Ryan, D.; Willson, C. G.; Whitesides, G. M. New Approaches to Nanofabrication: Molding, Printing, and Other Techniques. *Chem. Rev.* **2005**, *105* (4), 1171–1196. <https://doi.org/10.1021/cr030076o>.
- (36) Nakagawa, K.; Taguchi, M.; Ema, T. Fabrication of 64M DRAM with I-Line Phase-Shift Lithography. *Tech. Dig. - Int. Electron Devices Meet.* **1990**, 817–820. <https://doi.org/10.1109/iedm.1990.237037>.
- (37) Yablonovitch, E.; Vrijen, R. B.; Angeles, L. L / J I / -J. **1998**, *2* (x), 126–128.
- (38) Haske, W.; Chen, V. W.; Hales, J. M.; Dong, W.; Barlow, S.; Marder, S. R.; Perry, J. W. 65 Nm Feature Sizes Using Visible Wavelength 3-D Multiphoton Lithography. *Opt. Express* **2007**, *15* (6), 3426. <https://doi.org/10.1364/oe.15.003426>.
- (39) Chen, Y. Nanofabrication by Electron Beam Lithography and Its Applications: A Review. *Microelectron. Eng.* **2015**, *135*, 57–72. <https://doi.org/10.1016/j.mee.2015.02.042>.
- (40) Developments, R.; Operational, O. S. F. Microfluidics-a Review. **1993**.
- (41) Trietsch, S. J.; Hankemeier, T.; van der Linden, H. J. Lab-on-a-Chip Technologies for Massive Parallel Data Generation in the Life Sciences: A Review. *Chemom. Intell. Lab. Syst.* **2011**, *108* (1), 64–75. <https://doi.org/10.1016/j.chemolab.2011.03.005>.
- (42) Fujii, T. PDMS-Based Microfluidic Devices for Biomedical Applications. *Microelectron. Eng.* **2002**, *61–62*, 907–914. [https://doi.org/10.1016/S0167-9317\(02\)00494-X](https://doi.org/10.1016/S0167-9317(02)00494-X).
- (43) Qin, D.; Xia, Y.; Whitesides, G. M. Soft Lithography for Micro- and Nanoscale Patterning. *Nat. Protoc.* **2010**, *5* (3), 491–502. <https://doi.org/10.1038/nprot.2009.234>.
- (44) Dendukuri, D.; Pregibon, D. C.; Collins, J.; Hatton, T. A.; Doyle, P. S. Continuous-Flow Lithography for High-Throughput Microparticle Synthesis. - Supplementary Information. *Nat. Mater.* **2006**, *5* (5), 1–12.
- (45) Dendukuri, D.; Gu, S. S.; Pregibon, D. C.; Hatton, T. A.; Doyle, P. S. Stop-Flow Lithography in a Microfluidic Device. *Lab Chip* **2007**. <https://doi.org/10.1039/b703457a>.
- (46) Bong, K. W.; Pregibon, D. C.; Doyle, P. S. Lock Release Lithography for 3D and Composite Microparticles. *Lab Chip* **2009**, *9* (7), 863–866. <https://doi.org/10.1039/b821930c>.

- (47) Habasaki, S.; Lee, W. C.; Yoshida, S.; Takeuchi, S. Vertical Flow Lithography for Fabrication of 3D Anisotropic Particles. *Small* **2015**, *11* (48), 6391–6396. <https://doi.org/10.1002/sml.201502968>.
- (48) Jang, J.-H.; Dendukuri, D.; Hatton, T. A.; Thomas, E. L.; Doyle, P. S. A Route to Three-Dimensional Structures in a Microfluidic Device: Stop-Flow Interference Lithography. *Angew. Chemie* **2007**, *119* (47), 9185–9189. <https://doi.org/10.1002/ange.200703525>.
- (49) Kaminaga, M.; Ishida, T.; Omata, T. Fabrication of Pneumatic Microvalve for Tall Microchannel Using Inclined Lithography. *Micromachines* **2016**, *7* (12). <https://doi.org/10.3390/mi7120224>.
- (50) Lee, S. A.; Chung, S. E.; Park, W.; Lee, S. H.; Kwon, S. Three-Dimensional Fabrication of Heterogeneous Microstructures Using Soft Membrane Deformation and Optofluidic Maskless Lithography. *Lab Chip* **2009**. <https://doi.org/10.1039/b819999j>.
- (51) Panda, P.; Yuet, K. P.; Hatton, T. A.; Doyle, P. S. Tuning Curvature in Flow Lithography: A New Class of Concave/Convex Particles. *Langmuir* **2009**, *25* (10), 5986–5992. <https://doi.org/10.1021/la8042445>.
- (52) Le Goff, G. C.; Lee, J.; Gupta, A.; Hill, W. A.; Doyle, P. S. High-Throughput Contact Flow Lithography. *Adv. Sci.* **2015**, *2* (10), 1–7. <https://doi.org/10.1002/advs.201500149>.
- (53) Tian, Y.; Wang, L. Complex Three-Dimensional Microparticles from Microfluidic Lithography. *Electrophoresis* **2020**, 1–12. <https://doi.org/10.1002/elps.201900322>.
- (54) Eddings, M. A.; Johnson, M. A.; Gale, B. K. Determining the Optimal PDMS-PDMS Bonding Technique for Microfluidic Devices. *J. Micromechanics Microengineering* **2008**, *18* (6). <https://doi.org/10.1088/0960-1317/18/6/067001>.
- (55) Ullah, F.; Othman, M. B. H.; Javed, F.; Ahmad, Z.; Akil, H. M. Classification, Processing and Application of Hydrogels: A Review. *Mater. Sci. Eng. C* **2015**, *57*, 414–433. <https://doi.org/10.1016/j.msec.2015.07.053>.
- (56) Mcdermott, S. Investigation of UV-LED Initiated Photopolymerisation of Bio-Compatible HEMA. *Dublin Inst. Technol.* **2008**, 196.
- (57) Kotz, F.; Plewa, K.; Bauer, W.; Hanemann, T.; Waldbaur, A.; Wilhelm, E.; Neumann, C.; Rapp, B. E. Rapid Prototyping of Glass Microfluidic Chips. *Microfluid. BioMEMS, Med. Microsystems XIII* **2015**, 9320 (March 2015), 932003. <https://doi.org/10.1117/12.2076964>.

- (58) Dendukuri, D.; Gu, S. S.; Pregibon, D. C.; Hatton, T. A.; Doyle, P. S. Stop-Flow Lithography in a Microfluidic Device. *Lab Chip* **2007**, 7 (7), 818–828. <https://doi.org/10.1039/b703457a>.
- (59) Zhong, C.; Wu, J.; Reinhart-King, C. A.; Chu, C. C. Synthesis, Characterization and Cytotoxicity of Photo-Crosslinked Maleic Chitosan-Polyethylene Glycol Diacrylate Hybrid Hydrogels. *Acta Biomater.* **2010**. <https://doi.org/10.1016/j.actbio.2010.04.011>.
- (60) Shepherd, R. F.; Panda, P.; Bao, Z.; Sandhage, K. H.; Hatton, T. A.; Lewis, J. A.; Doyle, P. S. Stop-Flow Lithography of Colloidal, Glass, and Silicon Microcomponents. *Adv. Mater.* **2008**. <https://doi.org/10.1002/adma.200801090>.
- (61) Baah, D.; Donnell, T.; Tigner, J.; Floyd-Smith, T. Stop Flow Lithography Synthesis of Non-Spherical Metal Oxide Particles. *Particuology* **2014**. <https://doi.org/10.1016/j.partic.2013.09.001>.
- (62) Yajima, Ceramics from Polymers.
- (63) Seyferth, Preceramics, Past, Present and Future.
- (64) Wynne, K. J.; Rice, R. W. Ceramics Via Polymer Pyrolysis. *Annu. Rev. Mater. Sci.* **1984**, 14, 297–334. <https://doi.org/10.1146/annurev.ms.14.080184.001501>.
- (65) Blum, Y. D.; Schwartz, K. B.; Laine, R. M. Preceramic Polymer Pyrolysis - Part 1 Pyrolytic Properties of Polysilazanes. *J. Mater. Sci.* **1989**, 24 (5), 1707–1718. <https://doi.org/10.1007/BF01105695>.
- (66) Karakuscu, A.; Guider, R.; Pavesi, L.; Sorarù, G. D. White Luminescence from Sol-Gel-Derived SiOC Thin Films. *J. Am. Ceram. Soc.* **2009**, 92 (12), 2969–2974. <https://doi.org/10.1111/j.1551-2916.2009.03343.x>.
- (67) Shi, H.; Yuan, A.; Xu, J. Tailored Synthesis of Monodispersed Nano/Submicron Porous Silicon Oxycarbide (SiOC) Spheres with Improved Li-Storage Performance as an Anode Material for Li-Ion Batteries. *J. Power Sources* **2017**, 364, 288–298. <https://doi.org/10.1016/j.jpowsour.2017.08.051>.
- (68) Shekhar, P.; Pendharker, S.; Sahasrabudhe, H.; Vick, D.; Malac, M.; Rahman, R.; Jacob, Z. Extreme Ultraviolet Plasmonics and Cherenkov Radiation in Silicon. *Optica* **2018**, 5 (12), 1590. <https://doi.org/10.1364/optica.5.001590>.

- (69) Zanchetta, E.; Cattaldo, M.; Franchin, G.; Schwentenwein, M.; Homa, J.; Brusatin, G.; Colombo, P. Stereolithography of SiOC Ceramic Microcomponents. *Adv. Mater.* **2016**. <https://doi.org/10.1002/adma.201503470>.
- (70) Ponomarev, I.; Van Duin, A. C. T.; Kroll, P. Reactive Force Field for Simulations of the Pyrolysis of Polysiloxanes into Silicon Oxycarbide Ceramics. *J. Phys. Chem. C* **2019**, *123* (27), 16804–16812. <https://doi.org/10.1021/acs.jpcc.9b03810>.
- (71) Zanchetta, E.; Cattaldo, M.; Franchin, G.; Schwentenwein, M.; Homa, J.; Brusatin, G.; Colombo, P. Stereolithography of SiOC Ceramic Microcomponents. **2016**, 370–376. <https://doi.org/10.1002/adma.201503470>.
- (72) Kotz, F.; Arnold, K.; Bauer, W.; Schild, D.; Keller, N.; Sachsenheimer, K.; Nargang, T. M.; Richter, C.; Helmer, D.; Rapp, B. E. Three-Dimensional Printing of Transparent Fused Silica Glass. *Nat. Publ. Gr.* **2017**, *544* (7650), 337–339. <https://doi.org/10.1038/nature22061>.
- (73) Brigo, L.; Eva, J.; Schmidt, M.; Gandin, A.; Michieli, N.; Colombo, P.; Brusatin, G. 3D Nanofabrication of SiOC Ceramic Structures. **2018**, *1800937*. <https://doi.org/10.1002/advs.201800937>.
- (74) Ye, C.; Chen, A.; Colombo, P.; Martinez, C. Ceramic Microparticles and Capsules via Microfluidic Processing of a Preceramic Polymer. *J. R. Soc. Interface* **2010**, *7* (SUPPL. 4). <https://doi.org/10.1098/rsif.2010.0133.focus>.
- (75) Dendukuri, D.; Panda, P.; Haghgooie, R.; Kim, J. M.; Hatton, T. A.; Doyle, P. S. Modeling of Oxygen-Inhibited Free Radical Photopolymerization in a PDMS Microfluidic Device. *Macromolecules* **2008**. <https://doi.org/10.1021/ma801219w>.
- (76) Lamberti, A.; Marasso, S. L.; Cocuzza, M. PDMS Membranes with Tunable Gas Permeability for Microfluidic Applications. *RSC Adv.* **2014**. <https://doi.org/10.1039/c4ra12934b>.
- (77) Firpo, G.; Angeli, E.; Repetto, L.; Valbusa, U. Permeability Thickness Dependence of Polydimethylsiloxane (PDMS) Membranes. *J. Memb. Sci.* **2015**. <https://doi.org/10.1016/j.memsci.2014.12.043>.
- (78) Nath, P.; Fung, D.; Kunde, Y. A.; Zeytun, A.; Branch, B.; Goddard, G. Rapid Prototyping of Robust and Versatile Microfluidic Components Using Adhesive Transfer Tapes. *Lab Chip* **2010**. <https://doi.org/10.1039/c002457k>.

- (79) Satyanarayana, S.; Karnik, R. N.; Majumdar, A. Stamp-and-Stick Room-Temperature Bonding Technique for Microdevices. *J. Microelectromechanical Syst.* **2005**. <https://doi.org/10.1109/JMEMS.2004.839334>.
- (80) Yang, W.; Yu, H.; Liang, W.; Wang, Y.; Liu, L. Rapid Fabrication of Hydrogel Microstructures Using UV-Induced Projection Printing. *Micromachines* **2015**. <https://doi.org/10.3390/mi6121464>.
- (81) Models, S.; Xi, P. X-Cite ® 120PC Q User Guide.
- (82) Decker, C.; Moussa, K. Real-Time Kinetic Study of Laser-Induced Polymerization. *Macromolecules* **1989**, 22 (12), 4455–4462. <https://doi.org/10.1021/ma00202a013>.
- (83) Suh, S. K.; Yuet, K.; Hwang, D. K.; Bong, K. W.; Doyle, P. S.; Hatton, T. A. Synthesis of Nonspherical Superparamagnetic Particles: In Situ Coprecipitation of Magnetic Nanoparticles in Microgels Prepared by Stop-Flow Lithography. *J. Am. Chem. Soc.* **2012**. <https://doi.org/10.1021/ja209245v>.
- (84) Hwang, D. K.; Oakey, J.; Toner, M.; Arthur, J. A.; Anseth, K. S.; Lee, S.; Zeiger, A.; Van Vliet, K. J.; Doyle, P. S. Stop-Flow Lithography for the Production of Shape-Evolving Degradable Microgel Particles. *J. Am. Chem. Soc.* **2009**, 131 (12), 4499–4504. <https://doi.org/10.1021/ja809256d>.
- (85) Dendukuri, D.; Doyle, P. S. The Synthesis and Assembly of Polymeric Microparticles Using Microfluidics. *Adv. Mater.* **2009**, 21 (41), 4071–4086. <https://doi.org/10.1002/adma.200803386>.
- (86) Sadeghi, M.; Yarahmadi, M. Development of a Temperature - Sensitive Composite Hydrogel for Drug Delivery Applications. *Orient. J. Chem.* **2011**, 27 (3), 865–874.
- (87) Streeter, V. L.; Wylie, E. B. Fluid Mechanics (Seventh Ed.). **1979**.
- (88) Zheng, X.; Silber-Li, Z. H. Measurement of Velocity Profiles in a Rectangular Microchannel with Aspect Ratio $\alpha = 0.35$. *Exp. Fluids* **2008**. <https://doi.org/10.1007/s00348-007-0454-4>.
- (89) Bruus, H. Hydrodynamics and Lab-on-a-Chip Technology. **2009**, No. course 10030.
- (90) Decker, C.; Jenkins, A. D. Kinetic Approach of O₂ Inhibition in Ultraviolet and Laser-Induced Polymerizations. *Macromolecules* **1985**, 18 (6), 1241–1244. <https://doi.org/10.1021/ma00148a034>.

- (91) Colombo, P.; Mera, G.; Riedel, R.; Sorarù, G. D. Polymer-Derived Ceramics: 40 Years of Research and Innovation in Advanced Ceramics. *J. Am. Ceram. Soc.* **2010**. <https://doi.org/10.1111/j.1551-2916.2010.03876.x>.
- (92) Lewinsohn, C. A.; Colombo, P.; Reimanis, I.; Ünal, Ö. Stresses Occurring during Joining of Ceramics Using Preceramic Polymers. *J. Am. Ceram. Soc.* **2004**, *84* (10), 2240–2244. <https://doi.org/10.1111/j.1151-2916.2001.tb00995.x>.
- (93) Andrzejewska, E. Photopolymerization Kinetics of Multifunctional Monomers. *Progress in Polymer Science (Oxford)*. 2001. [https://doi.org/10.1016/S0079-6700\(01\)00004-1](https://doi.org/10.1016/S0079-6700(01)00004-1).
- (94) Decker, C. The Use of UV Irradiation in Polymerization. *Polym. Int.* **1998**, *45* (2), 133–141. [https://doi.org/10.1002/\(SICI\)1097-0126\(199802\)45:2<133::AID-PI969>3.0.CO;2-F](https://doi.org/10.1002/(SICI)1097-0126(199802)45:2<133::AID-PI969>3.0.CO;2-F).
- (95) Pantano, C. G.; Singh, A. K.; Zhang, H. *Silicon Oxycarbide Glasses*; 1999; Vol. 14.
- (96) Sandra, F.; Depardieu, M.; Mouline, Z.; Vignoles, G. L.; Iwamoto, Y.; Miele, P.; Backov, R.; Bernard, S. Polymer-Derived Silicoboron Carbonitride Foams for CO₂ Capture: From Design to Application as Scaffolds for the in Situ Growth of Metal-Organic Frameworks. *Chem. - A Eur. J.* **2016**, *22* (24), 8346–8357. <https://doi.org/10.1002/chem.201600060>.
- (97) Carbide-Derived Carbons with Tunable Porosity. *Management* **2009**, 1–27.
- (98) Mohanta, K.; Kumar, A.; Parkash, O.; Kumar, D. Processing and Properties of Low Cost Macroporous Alumina Ceramics with Tailored Porosity and Pore Size Fabricated Using Rice Husk and Sucrose. *J. Eur. Ceram. Soc.* **2014**, *34* (10), 2401–2412. <https://doi.org/10.1016/j.jeurceramsoc.2014.01.024>.
- (99) Zeschky, J.; Goetz-Neunhoeffler, F.; Neubauer, J.; Lo, S. H. J.; Kummer, B.; Scheffler, M.; Greil, P. Preceramic Polymer Derived Cellular Ceramics. *Compos. Sci. Technol.* **2003**, *63* (16), 2361–2370. [https://doi.org/10.1016/S0266-3538\(03\)00269-0](https://doi.org/10.1016/S0266-3538(03)00269-0).
- (100) Vakifahmetoglu, C.; Balliana, M.; Colombo, P. Ceramic Foams and Micro-Beads from Emulsions of a Preceramic Polymer. *J. Eur. Ceram. Soc.* **2011**, *31* (8), 1481–1490. <https://doi.org/10.1016/j.jeurceramsoc.2011.02.012>.
- (101) Schultz, S.; Wagner, G.; Urban, K.; Ulrich, J. High-Pressure Homogenization as a Process for Emulsion Formation. *Chem. Eng. Technol.* **2004**, *27* (4), 361–368. <https://doi.org/10.1002/ceat.200406111>.

- (102) Porras, M.; Solans, C.; González, C.; Gutiérrez, J. M. Properties of Water-in-Oil (W/O) Nano-Emulsions Prepared by a Low-Energy Emulsification Method. *Colloids Surfaces A Physicochem. Eng. Asp.* **2008**, 324 (1–3), 181–188. <https://doi.org/10.1016/j.colsurfa.2008.04.012>.
- (103) Shepherd, R. F.; Panda, P.; Bao, Z.; Sandhage, K. H.; Hatton, T. A.; Lewis, J. A.; Doyle, P. S. Stop-Flow Lithography of Colloidal, Glass, and Silicon Microcomponents. *Adv. Mater.* 2008, 20 (24), 4734–4739. <https://doi.org/10.1002/adma.200801090>.
- (104) McClements, David Julian. Food emulsions: principles, practices, and techniques. CRC press, 2015. <https://books.google.com>
- (105) Weiss, J. 5. Emulsion Processing -Homogenization-. Univ. Massachusetts Amherst 2008, 1–50.
- (106) Stone, H. A.; Leal, L. G. The Influence of Initial Deformation on Drop Breakup in Subcritical Time-Dependent Flows at Low Reynolds Numbers. *J. Fluid Mech.* **1989**, 206, 223–263. <https://doi.org/10.1017/S0022112089002296>.
- (107) Janssen, J. M. H.; Meijer, H. E. H. Droplet Breakup Mechanisms: Stepwise Equilibrium versus Transient Dispersion. *J. Rheol. (N. Y. N. Y.)*. **1993**, 37 (4), 597–608. <https://doi.org/10.1122/1.550385>.
- (108) Driessen, T. *Drop Formation from Axi-Symmetric Fluid Jets*; 2013.
- (109) Caubet, S.; Le Guer, Y.; Grassl, B.; El Omari, K.; Normandin, E. A Low-Energy Emulsification Batch Mixer for Concentrated Oil-in-Water Emulsions. *AIChE J.* **2011**, 57 (1), 27–39. <https://doi.org/10.1002/aic.12253>.
- (110) Powers, T. R.; Goldstein, R. E. Pearling and Pinching: Propagation of Rayleigh Instabilities. *Phys. Rev. Lett.* **1997**, 78 (13), 2555–2558. <https://doi.org/10.1103/PhysRevLett.78.2555>.
- (111) van Hoeve, W.; Gekle, S.; Snoeijer, J. H.; Versluis, M.; Brenner, M. P.; Lohse, D. Breakup of Diminutive Rayleigh Jets. *Phys. Fluids* **2010**, 22 (12), 1–24. <https://doi.org/10.1063/1.3524533>.
- (112) Hagedorn, J. G.; Martys, N. S.; Douglas, J. F. Breakup of a Fluid Thread in a Confined Geometry: Droplet-Plug Transition, Perturbation Sensitivity, and Kinetic Stabilization with Confinement. *Phys. Rev. E - Stat. Physics, Plasmas, Fluids, Relat. Interdiscip. Top.* **2004**, 69 (5), 18. <https://doi.org/10.1103/PhysRevE.69.056312>.

- (113) Jiao, J.; Burgess, D. J. Rheology and Stability of Water-in-Oil-in-Water Multiple Emulsions Containing Span 83 and Tween 80. *AAPS PharmSci* **2003**, *5* (1), 1–12. <https://doi.org/10.1208/ps050107>.
- (114) Leong, T. S. H.; Wooster, T. J.; Kentish, S. E.; Ashokkumar, M. Minimising Oil Droplet Size Using Ultrasonic Emulsification. *Ultrason. Sonochem.* **2009**, *16* (6), 721–727. <https://doi.org/10.1016/j.ultsonch.2009.02.008>.
- (115) Basu, P. 濟無No Title No Title. *J. Chem. Inf. Model.* **2013**, *53* (9), 1689–1699. <https://doi.org/10.1017/CBO9781107415324.004>.
- (116) Abismail, B.; Canselier, J. P.; Wilhelm, A. M.; Delmas, H.; Gourdon, C. Emulsification by Ultrasound : Drop Size Distribution and Stability. *Ultrason. Sonochem.* **1999**, *6*, 75–83.
- (117) Abbott, S. Surfactant Science : Principles and Practice. *Surfactant Sci. Princ. Pract.* **2015**, 1–249.
- (118) Chen, X.; Xue, C.; Zhang, L.; Hu, G.; Jiang, X.; Sun, J. Inertial Migration of Deformable Droplets in a Microchannel. *Phys. Fluids* **2014**, *26* (11). <https://doi.org/10.1063/1.4901884>.
- (119) Segré, G.; Silberberg, A. Behaviour of Macroscopic Rigid Spheres in Poiseuille Flow: Part 2. Experimental Results and Interpretation. *J. Fluid Mech.* **1962**, *14* (1), 136–157. <https://doi.org/10.1017/S0022112062001111>.
- (120) Lan, H.; Khismatullin, D. B. A Numerical Study of the Lateral Migration and Deformation of Drops and Leukocytes in a Rectangular Microchannel. *Int. J. Multiph. Flow* **2012**, *47*, 73–84. <https://doi.org/10.1016/j.ijmultiphaseflow.2012.07.004>.
- (121) Van Dinter, A. M. C.; Schroën, C. G. P. H.; Vergeldt, F. J.; Van Der Sman, R. G. M.; Boom, R. M. Suspension Flow in Microfluidic Devices - A Review of Experimental Techniques Focussing on Concentration and Velocity Gradients. *Adv. Colloid Interface Sci.* **2012**, *173*, 23–34. <https://doi.org/10.1016/j.cis.2012.02.003>.
- (122) Bhagat, A. A. S.; Kuntaegowdanahalli, S. S.; Papautsky, I. Enhanced Particle Filtration in Straight Microchannels Using Shear-Modulated Inertial Migration. *Phys. Fluids* **2008**, *20* (10). <https://doi.org/10.1063/1.2998844>.
- (123) Municchi, F.; Nagrani, P. P.; Christov, I. C. A Two-Fluid Model for Numerical Simulation of Shear-Dominated Suspension Flows. *Int. J. Multiph. Flow* **2019**, *120*, 103079. <https://doi.org/10.1016/j.ijmultiphaseflow.2019.07.015>.

- (124) Nott, P. R.; Brady, J. F. Pressure-Driven Flow of Suspensions: Simulation and Theory. *J. Fluid Mech.* **1994**, 275 (6), 157–199. <https://doi.org/10.1017/S0022112094002326>.
- (125) Sardela, M. *Practical Materials Characterization*; 2014. <https://doi.org/10.1007/978-1-4614-9281-8>.
- (126) Multidisciplinary engineering, Rochester Institute of Technology, <http://edge.rit.edu>
- (127) Song, H. J.; You, S.; Jia, X. H.; Yang, J. MoS₂ Nanosheets Decorated with Magnetic Fe₃O₄ Nanoparticles and Their Ultrafast Adsorption for Wastewater Treatment. *Ceram. Int.* **2015**, 41 (10), 13896–13902. <https://doi.org/10.1016/j.ceramint.2015.08.023>.
- (128) Akhter, S.; Paul, D. P.; Hakim, A.; Saha, D. K. Synthesis , Structural and Physical Properties of Cu _{1 - x} Zn _x Fe ₂ O ₄ Ferrites. **2011**, 2011 (November), 1675–1681. <https://doi.org/10.4236/msa.2011.211223>.
- (129) Mitomo, M.; Uenosono, S. *Gas Pressure Sintering of β -Silicon Nitride*; 1991; Vol. 26. <https://doi.org/10.1007/BF01184995>.
- (130) Hocheplied, J. F.; Pileni, M. P. Magnetic Properties of Mixed Cobalt-Zinc Ferrite Nanoparticles. *J. Appl. Phys.* **2000**, 87 (5), 2472–2478. <https://doi.org/10.1063/1.372205>.
- (131) Huang, X.; Zhang, J.; Xiao, S.; Chen, G. The Cobalt Zinc Spinel Ferrite Nanofiber: Lightweight and Efficient Microwave Absorber. *J. Am. Ceram. Soc.* **2014**, 97 (5), 1363–1366. <https://doi.org/10.1111/jace.12909>.
- (132) Tatarchuk, T. R.; Paliychuk, N. D.; Bououdina, M.; Al-Najar, B.; Pacia, M.; Macyk, W.; Shyichuk, A. Effect of Cobalt Substitution on Structural, Elastic, Magnetic and Optical Properties of Zinc Ferrite Nanoparticles. *J. Alloys Compd.* **2018**, 731, 1256–1266. <https://doi.org/10.1016/j.jallcom.2017.10.103>.
- (133) Patil, V. G.; Shirsath, S. E.; More, S. D.; Shukla, S. J.; Jadhav, K. M. Effect of Zinc Substitution on Structural and Elastic Properties of Cobalt Ferrite. *J. Alloys Compd.* **2009**, 488 (1), 199–203. <https://doi.org/10.1016/j.jallcom.2009.08.078>.
- (134) Bayoumi, W. Structural and Electrical Properties of Zinc-Substituted Cobalt Ferrite. *J. Mater. Sci.* **2007**, 42 (19), 8254–8261. <https://doi.org/10.1007/s10853-007-1616-8>.
- (135) Srivastava, R.; Yadav, B. C. Ferrite Materials: Introduction, Synthesis Techniques, and Applications as Sensors. *Int. J. Green Nanotechnol. Biomed.* **2012**, 4 (2), 141–154. <https://doi.org/10.1080/19430892.2012.676918>.

- (136) Suh, S. K.; Bong, K. W.; Hatton, T. A.; Doyle, P. S. Using Stop-Flow Lithography to Produce Opaque Microparticles: Synthesis and Modeling. *Langmuir* **2011**, 27 (22), 13813–13819. <https://doi.org/10.1021/la202796b>.
- (137) Wang, G.; Ma, Y.; Tong, Y.; Dong, X. Development of Manganese Ferrite/Graphene Oxide Nanocomposites for Magnetorheological Fluid with Enhanced Sedimentation Stability. *J. Ind. Eng. Chem.* **2017**, 48, 142–150. <https://doi.org/10.1016/j.jiec.2016.12.032>.
- (138) Lee, S.; Shin, K. Y.; Jang, J. Enhanced Magnetorheological Performance of Highly Uniform Magnetic Carbon Nanoparticles. *Nanoscale* **2015**, 7 (21), 9646–9654. <https://doi.org/10.1039/c4nr07168a>.
- (139) Akbulut, O.; MacE, C. R.; Martinez, R. V.; Kumar, A. A.; Nie, Z.; Patton, M. R.; Whitesides, G. M. Separation of Nanoparticles in Aqueous Multiphase Systems through Centrifugation. *Nano Lett.* **2012**, 12 (8), 4060–4064. <https://doi.org/10.1021/nl301452x>.
- (140) Beakke, M. K. Density Gradient Centrifugation: A New Separation Technique. *J. Am. Chem. Soc.* **1951**, 73 (4), 1847–1848. <https://doi.org/10.1021/ja01148a508>.
- (141) Graham, J. M. Preparation of Crude Subcellular Fractions by Differential Centrifugation. *ScientificWorldJournal*. **2002**, 2, 1638–1642. <https://doi.org/10.1100/tsw.2002.851>.
- (142) Yousefi, M. H.; Manouchehri, S.; Arab, A.; Mozaffari, M.; Amiri, G. R.; Amighian, J. Preparation of Cobalt-Zinc Ferrite ($\text{Co}_{0.8}\text{Zn}_{0.2}\text{Fe}_{2}\text{O}_4$) Nanopowder via Combustion Method and Investigation of Its Magnetic Properties. *Mater. Res. Bull.* **2010**, 45 (12), 1792–1795. <https://doi.org/10.1016/j.materresbull.2010.09.018>.
- (143) Vinson, V. K. Drug Targeting. *Sci. Signal.* **2013**, 6 (283), 81–91. <https://doi.org/10.1126/scisignal.2004484>.
- (144) Furlani, E. J.; Furlani, E. P. A Model for Predicting Magnetic Targeting of Multifunctional Particles in the Microvasculature. *J. Magn. Magn. Mater.* **2007**, 312 (1), 187–193. <https://doi.org/10.1016/j.jmmm.2006.09.026>.
- (145) Nancy Hall, Shapes effects on drag, NASA, Sep 2015, <https://www.grc.nasa.gov/www/k-12/airplane/shaped.html>
- (146) Kane, S. N.; Mishra, A.; Dutta, A. K. Preface: International Conference on Recent Trends in Physics (ICRTP 2016). *J. Phys. Conf. Ser.* **2016**, 755 (1), 0–13. <https://doi.org/10.1088/1742-6596/755/1/011001>.

- (147) Kümmel, F.; Ten Hagen, B.; Wittkowski, R.; Buttinoni, I.; Eichhorn, R.; Volpe, G.; Löwen, H.; Bechinger, C. Circular Motion of Asymmetric Self-Propelling Particles. *Phys. Rev. Lett.* **2013**, *110* (19), 1–5. <https://doi.org/10.1103/PhysRevLett.110.198302>.
- (148) Hu, J.; Zhou, S.; Sun, Y.; Fang, X.; Wu, L. Fabrication, Properties and Applications of Janus Particles. *Chem. Soc. Rev.* **2012**, *41* (11), 4356–4378. <https://doi.org/10.1039/c2cs35032g>.
- (149) Walther, A.; Müller, A. H. E. Janus Particles: Synthesis, Self-Assembly, Physical Properties, and Applications. *Chem. Rev.* **2013**, *113* (7), 5194–5261. <https://doi.org/10.1021/cr300089t>.
- (150) Dendukuri, D.; Pregibon, D. C.; Collins, J.; Hatton, T. A.; Doyle, P. S. Continuous-Flow Lithography for High-Throughput Microparticle Synthesis. *Nat. Mater.* **2006**. <https://doi.org/10.1038/nmat1617>.
- (151) Keulegan, G. H. Laminar Flow at the Interface of Two Liquids. *J. Res. Natl. Bur. Stand. (1934)*. **1944**, *32* (6), 303. <https://doi.org/10.6028/jres.032.016>.
- (152) Views, R. E.; Of, S.; Work, P. Nter: Ace. **1968**, No. 3, 652–658.
- (153) WASAN DT; GUPTA L; VORA MK. Interfacial Shear Viscosity At Fluid-Fluid Interfaces. **1970**, *17* (6).
- (154) Fabrication of Micro-Batteries via Stop-Flow Lithography. **2015**, No. August, 2015.
- (155) Soc, J. A. C.; Whitesides, G. M.; Grzybowski, B. Self-Assembly at All Scales. **2002**, 295 (March), 2418–2422.
- (156) Huck, W. T. S.; Tien, J.; Whitesides, G. M. Three-Dimensional Mesoscale Self-Assembly [12]. *J. Am. Chem. Soc.* **1998**, *120* (32), 8267–8268. <https://doi.org/10.1021/ja981390g>.
- (157) Pangali, C.; Rao, M.; Berne, B. J. Hydrophobic Hydration around a Pair of Apolar Species in Water. *J. Chem. Phys.* **1979**, *71* (7), 2982–2990. <https://doi.org/10.1063/1.438702>.

VITA

Alejandro M. Alcaraz Ramirez was born on October 19th of 1984, in Mexico City, Mexico. He graduated from Tecnológico de Monterrey campus CM, as Mechanical Electrical Engineer in 2007, where he received a laureate for the highest GPA of his graduating class. After graduation, the Taiwanese government granted him a fellowship to study mandarin for 1 year. He worked in the industry as Technology Analyst and Technical Manager. In 2015, he decided to go back to academia to pursue his PhD as part of Prof. Martinez research group in Materials Engineering department at Purdue University, where he arranged an SFL setup for the fabrication of functional microparticles. During his time at Purdue, he also enrolled in a certificate program in Mechanical and Electrical Engineering for hybrid electric vehicles. He assisted the Graduate Student Association one year as Cultural Chair. He is part of SHPE and ACERS associations. He also participated in IEEE UAVs club Purdue chapter.